Summer 2002

Development of an Efficient Ti:Sapphire Laser Transmitter for Atmospheric Ozone Lidar Measurements

Khaled A. Elsayed
Old Dominion University

Recommended Citation

Elsayed, Khaled A.. "Development of an Efficient Ti:Sapphire Laser Transmitter for Atmospheric Ozone Lidar Measurements" (2002). Doctor of Philosophy (PhD), Dissertation, Electrical & Computer Engineering, Old Dominion University, DOI: 10.25777/y549-8118
https://digitalcommons.odu.edu/ece_etds/70

DEVELOPMENT OF AN EFFICIENT TI:SAPPHIRE LASER TRANSMITTER FOR ATMOSPHERIC OZONE LIDAR MEASUREMENTS

by

Khaled A. Elsayed
B.Sc. May 1991 Cairo University
M.Sc. May 1996 Cairo University

A Dissertation Submitted to the Faculty of Old Dominion University in
Partial Fulfillment of the Requirement for the Degree of

DOCTOR OF PHILOSOPHY

ELECTRICAL ENGINEERING

OLD DOMINION UNIVERSITY
August 2002

Approved by:

Hani Elsayed-Ali (Director)

Linda Vahala (Member)

John Cooper (Member)

Russell DeYoung (Co-Advisor)

ABSTRACT

DEVELOPMENT OF AN EFFICIENT TI:SAPPHIRE LASER TRANSMITTER FOR ATMOSPHERIC OZONE LIDAR MEASUREMENTS

Khaled A. Elsayed
Old Dominion University, 2002
Director: Dr. Hani Elsayed-Ali

The impetus of this work was to develop an all solid-state Ti:sapphire laser transmitter to replace the current dye lasers that could provide a potentially compact, robust, and highly reliable laser transmitter for differential absorption lidar measurements of atmospheric ozone. Two compact, high-energy pulsed, and injection-seeded Ti:sapphire lasers operating at a pulse repetition frequency of 30 Hz and wavelengths of 867 nm and 900 nm, with M^2 of 1.3, have been experimentally demonstrated and compared to model results. The Ti:sapphire lasers have shown the required output beam quality at maximum output pulse energy, 115 mJ at 867 nm and 105 mJ at 900 nm, with a slope efficiency of 40% and 32%, respectively, to achieve 30 mJ of ultraviolet laser output at 289 nm and 300 nm with two LBO nonlinear crystals.

This dissertation is dedicated to my lovely family

ACKNOWLEDGMENTS

I'm grateful to many people who have supported and helped me during the successful completion of this dissertation. I gratefully acknowledge the inspiration of my advisors, Dr. Hani Elsayed-Ali, of Old Dominion University and Dr. Russell DeYoung of NASA, Langley Research Center, who both helped me during this effort in many different ways with useful suggestions and helpful advice. Their guidance in reviewing my work enabled me to maintain focus and enhanced my research skills. The tireless efforts of Dr. DeYoung deserve special recognition.

While conducting this research, I spent the majority of my time at NASA, Langley Research Center. I would, therefore, like to thank my colleagues, who have always been ready to help, in the Laser and Electro-Optics Branch for their kind and generous support. A special thanks also goes to Dr. Larry Petway, William Edwards, Byron Meadows, Waverly Marsh, James Barnes, and Dr. Norman Barnes for their scientific input, insightful discussions, and technical assistance.

Additionally, I would like to express appreciation to the Chemistry and Dynamics Branch of NASA Langley Research Center, and in particular, Dr. Bill Grant, Dr. Syed Ismail, Dr. Edward Browell, and Anthony Notari for providing positive feedback and support.

I would like to convey my appreciation to my advising committee members, Dr. John Cooper and Dr. Linda Vahala for serving on my committee.

Finally, I wholeheartedly and graciously thank my family and friends who have supported and encouraged me throughout my academic career. My family has always supported me and been at my side even though they live thousands of miles away.

TABLE OF CONTENTS

Page

LIST OF TABLES

LIST OF FIGURES

CHAPTER I

INTRODUCTION

1. 1. Importance of Atmospheric Ozone

Ozone is a very rare gas in the atmosphere averaging about 30 molecules of ozone for every one billion unpolluted near surface air molecules. Most of the ozone is found within two regions of the atmosphere; 90% resides in the stratosphere, which is located between 10 and 50 km above the Earth's surface. This layer is known as "the ozone layer." The remaining ozone is in the lower region of the atmosphere, the troposphere, which ranges from sea level up to about 10 km. In both the stratosphere and the troposphere, ozone molecules have the same chemical formula, O_3, but the effect of ozone on human and plant life is vastly different [1].

Ozone in the troposphere, near the Earth's surface, has direct contact with life forms where high levels are toxic to living systems and can severely damage the tissue of plants and animals [2]. Many studies have shown that ozone has harmful effects on crop production [3], forest growth [4], and human health [5]. Ozone is a key component of smog, a familiar problem in the atmosphere of many industrialized cities around the world. However, increased amounts of surface-level ozone are now being observed in rural areas as well, leading to heightened concern about levels of ozone in the troposphere. To observe changes of ozone in the troposphere, it is necessary to monitor concentrations at different heights and global locations.

The format model of this dissertation is the *Optical Engineering Journal.*

Ozone in the stratosphere, in contrast to ozone in the troposphere, has a great benefit for human beings. It filters the sun's ultraviolet-B (UV-B) radiation that would reach the Earth's surface and lead to skin cancer and cataracts. Thus, there is great interest in studying the loss of stratospheric ozone. Ground-based, airborne, and satellite instruments have measured a decrease in the amount of stratospheric ozone. Over some parts of Antarctica, up to 60 percent of the total amount of ozone, known as the "column ozone," is depleted during September and October each year [6]. This phenomenon is known as the "ozone hole." A significant stratospheric ozone decrease has been observed at other, more populated regions of the Earth [6], and increases in surface UV-B radiation have been observed in association with decreases in stratospheric ozone.

Much scientific evidence has been collected over the last two decades to show that man-made chemicals are responsible for the observed depletion of the ozone layer over Antarctica [6]. The ozone depleting chemical compounds contain chlorine, fluorine, bromine, carbon, and hydrogen, and they are described by the general term "halocarbons." The compounds that contain only carbon, chlorine, and fluorine are called "chlorofluorocarbons." The production of these chemicals is now regulated. The measurement of ozone in both the troposphere and stratosphere is critical to understanding the production, destruction, and transport of ozone in the global atmosphere.

1. 2. Methods of Ozone Measurement

There are two general approaches to making atmospheric ozone measurements. The first approach is in-situ, and the second is remote sensing.

In-Situ Measurements

In-situ measurements of ozone involve direct sampling of the atmosphere. A sample of the atmosphere (air) is brought into the instrument and is analyzed for its properties and/or its relative amount of various chemical components including ozone. This can involve the use of mass or optical spectroscopy, chemical assays, or observation of how intense light interacts with the molecules inside the sample. These techniques can be employed either from ground, aircraft, or balloon platforms, but it cannot be done from space where there is no air. Balloons measure the change in ozone concentration with altitude as high as 40 km and provide several days of continuous coverage. In-situ devices that are used to measure ozone from balloons include electrochemical concentration cells (ECCs), which measure a current produced by chemical reactions with ozone. Photospectroscopy uses films or electronic sensors sensitive to UV light to measure wavelengths affected by ozone. Laser in situ sensors can measure absorption of laser light over a fixed optical path; thus, the more ozone, the more optical absorption. The advantage of in-situ measurements is that they are usually very specific and accurate and do not require a precise understanding of the radiative properties of the atmosphere, such as are needed for remote sensing.

Rockets can also measure ozone profiles from the ground to an altitude of 75 km by using photospectroscopy. Spectra are recorded instantaneously at various altitudes on film, or continuously by a photoelectric sensor, then ozone concentrations are calculated from the recorded intensities of UV light. Rockets provide all weather capability but are limited by their short life, narrow geographic range, and infrequent launch.

Remote Sensing Measurements

Remote sensing is defined as the technique of obtaining information about ozone through the analysis of data collected by instruments that are not in physical contact with ozone. Remote sensing differs from in-situ sensing, where instruments are immersed in, or physically capture, ozone. There are two types of remote sensing, passive and active. In the passive case, the observer depends on a natural source of light or other electromagnetic radiation, while in the active case the observer provides the light source. Passive remote sensing detects the sun's reflected or radiated energy, while active remote sensing sends out its own electromagnetic energy (usually a laser beam) and then records this light reflected back to a receiver.

Passive remote sensing

Passive remote sensing is an indirect way of measuring an atmospheric molecule or particle that involves observing the changes in electromagnetic radiation coming from the sun. These changes in radiation can be observed because each atmospheric constituent absorbs radiation at certain wavelengths in different regions of the electromagnetic spectrum. This radiation is emitted, reflected, and scattered by the atmosphere and the Earth's surface over a wide range of wavelengths from the infrared, visible, ultraviolet, and microwave regions of the spectrum. The radiation is altered by the type, size, and amount of constituent molecules in the atmosphere it encounters. It is also affected by atmospheric temperature. By knowing how and by what amount different molecules absorb radiation at different wavelengths, a "fingerprint" for each atmospheric constituent can be identified.

Physicists can identify a molecule by observing it with an instrument that is sensitive to radiation at certain wavelengths. An example of passive remote sensing is the use of a satellite platform to measure the light coming from the sun at the wavelength where ozone absorbs sunlight.

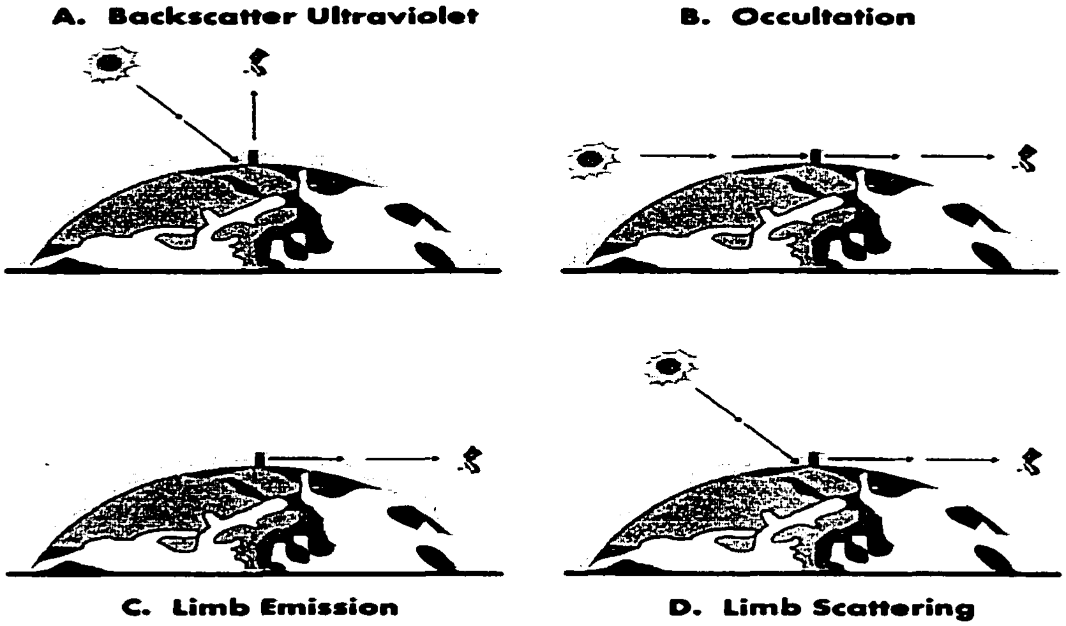

Fig. 1.1 Viewing Geometries of Remote Sensing Techniques for satellite platform (a) Backscatter Ultraviolet (b) Occultation (c) Limb emission and (d) Limb scattering [7]

Four passive remote sensing techniques exist for satellite platforms based on different viewing geometry concepts. The four techniques shown in Fig. 1.1 for passive remote sensing are (1) the backscatter ultraviolet (BUV) technique, (2) the occultation technique, (3) the limb emission technique, and (4) the limb scattering technique. Each technique involves a different viewing geometry that affects the measurement of atmospheric radiation. An example of passive remote sensing using a satellite platform is the backscatter ultraviolet (BUV) technique. In this technique, measurements are made of solar ultraviolet (UV) light entering the atmosphere (referred to as the irradiance) at a particular wavelength and of the solar UV that is either reflected from the surface or scattered back from the atmosphere (referred to as the radiance) at the same wavelength.

For determining total ozone, two pairs of measurements are made. One measurement of incoming UV light (irradiance) and backscattered UV light (radiance) is made at a wavelength that is strongly absorbed by ozone. The other measurement of incoming UV irradiance and backscattered UV radiance is made at a wavelength that is weakly absorbed by ozone. The difference in the pair of measurements at the two wavelengths is used to infer how much ozone is present in the atmosphere.

Information on the vertical atmospheric structure of ozone can be derived using the BUV profiling technique. The longer the wavelength of the incoming UV irradiance, the less absorption of this radiation by ozone occurs; thus the UV light penetrates far into the atmosphere. Conversely, the shorter the incoming UV irradiance wavelength, the more absorption of this radiation by ozone occurs; thus this UV light does not penetrate as far into the atmosphere. The absorption increases with decreasing wavelength, such that radiation at shorter wavelengths is significantly absorbed at higher altitudes. So the backscattered radiation at specific UV wavelengths can only be scattered from above a particular atmospheric height. Below this level, all the radiation is absorbed, and there is no backscattered radiance. This allows scientists to make a vertical profile measurement of ozone. Measurements at certain UV wavelengths are sensitive to specific portions of the ozone vertical profile, and the full atmospheric profile can be obtained by measuring radiation at a series of wavelengths and using a retrieval algorithm that converts each radiance measurement to an ozone number density.

A big advantage of the BUV technique is that by looking directly down at the atmosphere below in a viewing geometry called nadir viewing, the satellite is able to achieve a good horizontal resolution. The main disadvantage of the BUV technique is that the effects of increased multiple scattering and reduced sensitivity to the shape of the profile lead to poor vertical resolution in the region below the ozone peak (about 30 km).

Active remote sensing

An example of active remote sensing is laser remote sensing from aircraft using lidar (light detection and ranging), which is one important technique for measuring molecules and aerosols in the atmosphere. Lidars are active remote sensing instruments that can measure temperature and density profiles from measurements of atmospheric backscattered laser light.

Lidar is similar to radar but uses optical wavelengths. A basic lidar system is composed of a transmitter and receiver as shown in Fig. 1.2. A laser pulse at a specific wavelength is fired into the atmosphere. A portion of the energy in the laser pulse is scattered from the atmospheric molecules and aerosols. This reflected radiation is captured by the telescope field of view detected by a receiver system that is used to determine the relative concentration of atmospheric molecules and aerosols over the targeted region of the atmosphere. In addition to the relative concentration, the range of the interacting species can be determined from the temporal delay of the backscattered radiation. The variation in the received intensity as a function of time is used to determine the density profile of atmospheric molecules and aerosols. Lidar by itself cannot distinguish between different atmospheric molecular constituents; the more advanced differential absorption lidar technique is required.

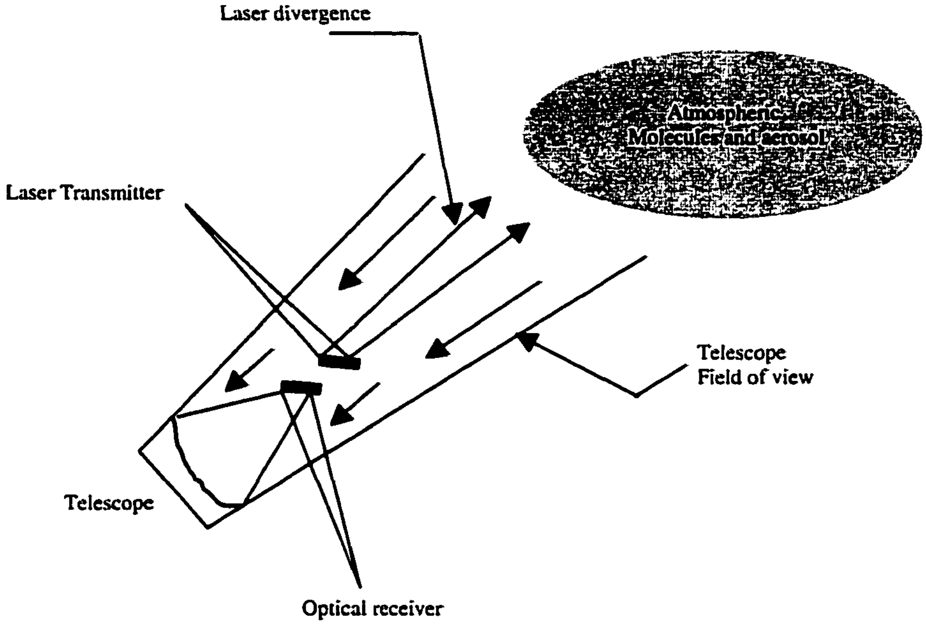

Fig. 1.2 Schematic diagram of typical lidar system.

1.3. Ozone differential absorption lidar (DIAL) technique

Laser remote sensing from aircraft has become a very important technique for observing ozone in the environment. NASA Langley uses a specialized lidar called the airborne Ultraviolet (UV) Differential Absorption Lidar (DIAL). Differential absorption lidar is a powerful technique to selectively measure the density of specific molecules in the atmosphere as a function of altitude. It uses two laser pulses of slightly different wavelength. One is chosen to coincide with a strong absorption feature of the specific molecule of interest, which is known as the "on-line" wavelength λ_{on}, while the other laser beam is tuned to a wavelength where there is less absorption and is known as the "off-line" wavelength, λ_{off}. Both λ_{on} and λ_{off} experience the same scattering from atmospheric molecules, but λ_{on} has slightly more absorption than λ_{off}; thus the difference in absorption will give a measure of ozone as a function of range. Pulsed laser beams are transmitted into the atmosphere, and the time between transmitting and receiving signals depends on the distance between the transmitter and the measured point in the atmosphere. The receiver system collects the backscattered light with a telescope, usually positioned close to the laser system.

Typical differential absorption lidar DIAL system

Figures 1.3 and 1.5 show a schematic diagram of a typical ozone DIAL system [1]. Two frequency-doubled Nd:YAG lasers are used to pump two, frequency doubled, tunable dye lasers. The four lasers are mounted in an aircraft on a structure that integrates the associated laser power supplies, the laser beam transmission optics, and the dual telescope and detector packages, which allow for simultaneous nadir and zenith O_3 measurements. One frequency doubled dye laser is operated at 289 nm for the DIAL on-line wavelength; the other is operated at 300 nm for the off-line wavelength. The DIAL wavelengths are produced in sequential laser pulses with a temporal separation of 300 μs to ensure that the same atmospheric scattering volume is sampled at both wavelengths during the DIAL measurement, as shown in Fig. 1.4. Half of each UV beam is transmitted in the zenith and nadir directions. The dye laser output at 600 and 582 nm that is left after the frequency doubling process and the residual 1064 nm outputs from the Nd:YAG lasers are also transmitted for aerosol profile measurements. They are then transmitted out of the aircraft co-linear to the receiver telescopes through 40-cm diameter quartz windows. Parameters for the airborne DIAL transmitter system are given in table 1.1.

The receiver system consists of two back-to-back 36-cm diameter Celestron telescopes and two identical detector packages. Each detector package has dichroic optics to separate the UV (289 and 300nm), visible (600 or 572 nm), and IR (1064 nm) lidar returns onto their respective detectors.

Table 1.1 Parameters of the NASA Langley airborne UV DIAL system [10]

Laser Continuum Model ND 6000 flashlamp-pumped Nd:YAG, Model 9030 dye lasers	
Pulse repetition frequency/Hz	30
Pulse length (ns)	8-12
Pulse energy (mJ)	250-350@1064nm 50-70@600nm 30@290/300nm
Wavelength separation for ozone measurements (nm)	10
Dimesnion (l x w x h) (m)	5.94 x 1.02 x 1.09
Weight (kg)	1735
Power requirements (kW)	30

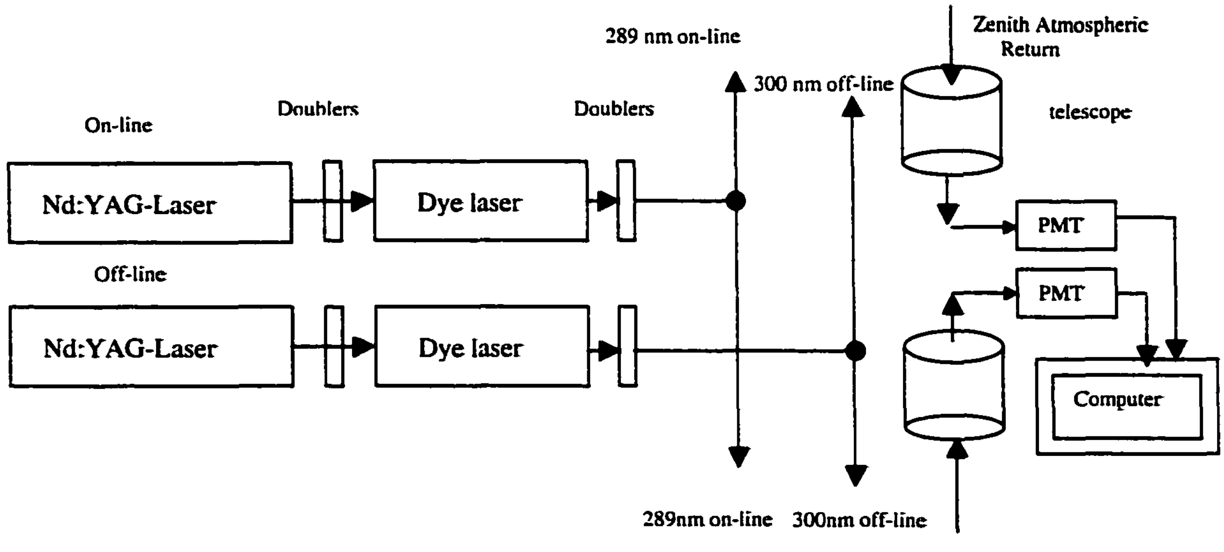

Fig. 1.3 Schematic diagram of the aircraft DIAL ozone system.

UV DIAL can give a much broader understanding of the chemistry, composition, and nature of the atmosphere. Since UV DIAL takes measurements from above and below the aircraft, it creates a two dimensional atmospheric ozone map of the surrounding area as shown in Fig. 1.6 [9] Using this map, other atmospheric events like a plume from a fire can be located, allowing other instruments to study it.

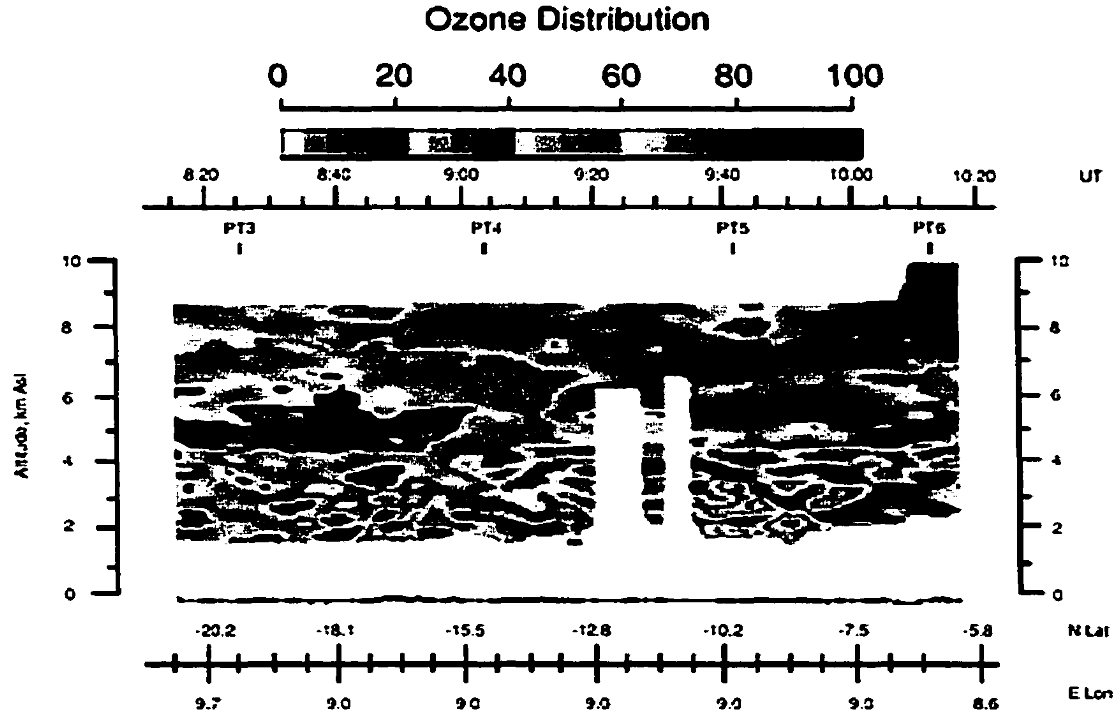

Fig. 1.6: Example of atmospheric ozone distribution map. Colors represent the level of ozone in the atmosphere and are given in units of ppb. The aircraft was flying at about 8.5 km and transmitting only in the down direction [9].

The image of Fig. 1.6 is a map of the ozone distribution associated with biomass burning in the western part of central Africa (below 6 kilometers) and another outflow from Brazil (above 6 kilometers). The image was taken as the plane flew up the west central coast of Africa. The color scale from blue (low concentration) to black (high concentration) indicates the concentration of ozone in the atmosphere. White areas indicate regions inaccessible to measurements because of a lack of data due to clouds. On the right hand side of the image, the pink color indicates that the ozone concentration is high where the biomass-burning plume is coming from Africa. Away from the burning plume, the air is clean as indicated by the low concentration of zone, which can be seen from the blue color on the left side of the image.

The UV DIAL system is used to study ozone in both the troposphere and stratosphere. In one six-week mission every year or two, scientists use the UV DIAL system to study the troposphere over remote areas such as the Atlantic and Pacific Oceans and parts of Africa, Brazil, and Canada. The UV DIAL system is being used in an airborne field experiment to study ozone in the stratosphere every three to five years, particularly in the polar regions where the most chemical ozone depletion occurs.

1.4. Limitations of current laser transmitter system.

The current aircraft UV-DIAL system, shown schematically in Fig 1.5, uses a dye laser to convert the 532nm pump energy to other visible wavelengths for conversion into the UV producing on and off line wavelengths. This configuration yields a nominal UV output of 30 mJ per pulse. As is common to most dye lasers, dyes must be changed on a regular basis due to bleaching effects that increase with operating time. Many dyes, including the ones currently used (Rh6G), are toxic and possibly carcinogenic. Given the high need for maintenance, there is an increased risk of exposure to the dye. Dyes are also often mixed with alcohol, making the mixture flammable and ill suited for use in airborne experiments. Considering all the drawbacks of operating dye lasers, replacement with a solid state, high-energy laser is highly advantageous.

1.5. Thesis research goals

The goal of this thesis research is the development of an advanced Ti:Sapphire solid state laser transmitter to replace the current dye lasers that could provide a potentially compact, robust, and highly reliable laser transmitter at the required on-line and off-line wavelengths for ozone differential absorption lidar measurements of atmospheric ozone. The Ti:sapphire laser will be pumped by a 30 Hz high energy Nd:YAG laser (532nm). The tunable Ti:sapphire laser will provide output pulses at 867nm and 900nm with a temporal separation of 300 μs. The laser cavity will be injection seeded using two external diode lasers operating at 867 nm and 900 nm respectively. The two different wavelength outputs are then frequency tripled using second and third harmonic generation schemes. The resulting output from the laser system would be a 30 Hz train of pulse pairs separated by 300 μs with the first pulse at wavelength 289nm (on-line) and the second pulse at a wavelength of 300nm (off-line).

The main goal is to achieve a high conversion efficiency of doubling and tripling for both wavelengths 867nm and 900nm resulting in a UV pulse energy of 40 mJ (on and off-line) at 30 Hz. This Ti:sapphire laser transmitter will be used as a replacement for the current tunable dye laser transmitters shown in Fig 1.3.

References:

1. S. Goldschmidt, R.J.Deyoung, "An Ozone Differential Absorption Lidar (DIAL) Receiver System for Use on Unpiloted Atmospheric Vehicles," NASA/TM-1999-209716.
2. Adams, R. M.. Hamilton, S. A., And McCarl, B. A. "An Assesment of Economic Effect of Ozone on U.S. Agriculture," *J. Air Pollut. Control Assoc.*, vol.35, 1985, pp.938-943.
3. Heck, Walter W.; Cure, William W.; Rawlings, John O.; Zaragoza, Lawrence J.; Heagle, Allen S.; Heggestad, Howard E.; Kohut, Robert J; Lance W.; and Temple, Patrick. "Assessing impacts of ozone on agriculture crops: Overview," *J. Air Pollut. Control Assoc.*, vol.34, no.7, 1984, pp.725-735.
4. Pye, John M, " Impact of Ozone on the Growth and Yield of Trees," *A review. J. Environ. Qual.*, vol.17, no.3, 1988, pp.347-360.
5. Lippmann, Morton: Health Effects of Ozone: Critical Review. *J. Air Pollut. Control Assoc.*, vol.39, no.5, 1989, pp.672-695.
6. Scientific Assessment of Ozone Depletion, 1994. NOAA, NASA, *United Nations Environment Program, and World Meteorol. Org.* 1994.
7. *The Stratospheric Ozone Electronic Textbook* was funded, developed, written, and edited by members of NASA's Goddard Space Flight Center Atmospheric Chemistry and Dynamics Branch (Code 916), Chapter 7 -- Ernest Hilsenrath.
8. Browell, Edward, "Differential Absorption Lidar Sensing of Ozone," *IEEE Proc.*, vol. 77. no. 3, pp.419-432, 1989.
9. *NASA facts* online, fs-2000-09-55-LaRC.

10. Browell, S. Ismail, W.B. Grant, "Differential absorption lidar (DIAL) measurements from air and space," *Appl. Phys.* B Vol.67, pp399-410, 1998.

CHAPTER II

THE LIDAR THEORY

This chapter covers the theory behind and the derivation of the Lidar and DIAL equations for measuring atmospheric ozone.

2.1. The Lidar Equation

Lidar is an active remote sensing technique that can measure the density and range of scattering molecules or aerosols in the atmosphere. A laser pulse is transmitted into the atmosphere and some of this light is scattered by molecules or aerosols into a receiver telescope. For a pulsed lidar, the increment of the signal power ΔP(λ,R) received by the detection system in the wavelength range (λ,λ+Δλ) from the range element (R,R+ΔR) is given by [2]

$$\Delta P(\lambda, R) = \int J(\lambda, R, r) \cdot \Delta\lambda \cdot \Delta R \cdot p(\lambda, R, r) dA(R, r), \tag{1}$$

where J(λ,R,r) represent the laser-induced spectral radiance at wavelength λ, at position r in the range R per unit range interval, p(λ,R,r) is the probability that radiation of wavelength λ scattered from position r at range R will be detected, and dA(R,r) is the element of the target area at position r and range R.

The probability p(λ,R,r) will be affected by several factors, which is given by

$$p(\lambda, R, r) = \frac{A_o}{R^2} \cdot T(\lambda, R) \cdot \eta(\lambda) \cdot \xi(R, r), \tag{2}$$

where A_o/R^2 is the acceptance solid angle of the receiver optics with A_o being the area of the telescope mirror, T(λ,R) is the atmospheric transmission factor at wavelength

λ over the range R, $\eta(\lambda)$ is the spectral transmission factor of the receiver which includes the effect of any spectral selecting elements such as filters, and $\xi(R,r)$ is the overlap factor or the geometrical form factor defined as the probability of radiation from position r at the range R being detected based on geometrical considerations. Assume that $\xi(R,r)$ depends only upon the overlap of the laser divergence with the field of view of the telescope. Consequently $\xi(R,r)$ is called overlap the factor.

The target spectral radiance $J(\lambda,R,r)$ depends upon the nature of the interaction between the laser radiation and the target medium. For an elastic scattering medium only, $J(\lambda,R,r)$ may be written in the form

$$J(\lambda,R,r)=\beta(\lambda_L,R,r)\cdot I(R,r), \tag{3}$$

where $I(R,r)$ is the laser irradiance at position r and range R, and

$$\beta(\lambda_L,R,r)=\sum_i N_i(R,r)\cdot\left\{\frac{d\sigma(\lambda_L)}{d\Omega}\right\}_i^s\cdot\Im_i(\lambda) \tag{4}$$

is the volume backscattering coefficient [2], where $N_i(R,r)$ is the number density of scatterer species i; $\{d\sigma(\lambda_L)/d\Omega\}_i^s$ is the differential scattering cross section under irradiation with laser radiation at wavelength λ_L, and $\Im_i(\lambda)\ \Delta\lambda$ is the fraction of the scattered radiation that falls into the wavelength interval $(\lambda, \lambda+\Delta\lambda)$.

To evaluate the total power of the return signal collected by the receiver at the instance t (where $t = 2R/c$) corresponding to the time interval between the leading edge of the laser pulse to range R and the returned radiation to reach the receiver, equation (1) must be integrated with respect to both the received wavelength and the range R.

$$P(\lambda,t)=\int_0^{R=ct/2} dR\int_{\Delta\lambda_0} d\lambda\int J(\lambda,R,r)\cdot p(\lambda,R,r)\cdot dA(R,r). \tag{5}$$

The range integral is required to account for the radiation reaching the receiver from any position along the path of the laser pulse from which scattering occurs. The range of the wavelength integral extends to cover the lidar receiver spectral window $\Delta\lambda_o$ centered at λ, which is usually defined by the receiver optical filter.

Substituting equations (2) and (3) into equation (5) yields:

$$P(\lambda,t)=A_o\int_0^{R=ct/2}\frac{dR}{R^2}\int_{\Delta\lambda_o}\eta(\lambda)\cdot d\lambda\int\beta(\lambda_L,R,r)\cdot T(\lambda,R)\cdot\xi(R,r)\cdot I(R,r)\cdot dA(R,r) \qquad (6)$$

In the case of an elastic scattering medium, the observed radiation is as narrowband as that of the laser radiation and both are much smaller than the receiver spectral window $\Delta\lambda_o$, thus both $S_i(\lambda)$ and β can then be treated as delta functions. Furthermore, assuming that the scattering medium is homogenous over the overlap between the telescope field of view and the laser beam divergence results in equation (6) being written in the form:

$$P(\lambda,t)=A_o\eta(\lambda)\int_0^{R=ct/2}\beta(\lambda_L,\lambda,R)\cdot T(\lambda,R)\cdot\frac{dR}{R^2}\int\xi(R,r)\cdot I(R,r)\cdot dA(R,r). \qquad (7)$$

As stated above, the probability $\xi(R,r)$ can be assumed to be unity where the field of view of the receiver overlaps with the laser beam divergence and zero elsewhere, and the lateral distribution of the laser pulse is uniform over an area $A_L(R)$ at the range R, resulting in

$$\int\xi(R,r)\cdot I(R,r)\cdot dA(R,r)=\xi(R)\cdot I(R)\cdot A_L(R). \qquad (8)$$

Equation (7) can now be written as

$$P(\lambda,t)=A_o\eta(\lambda)\int_0^{R=ct/2}\beta(\lambda_L,\lambda,R)\cdot T(\lambda,R)\cdot\xi(R)\cdot I(R)\cdot A_L(R)\frac{dR}{R^2}. \qquad (9)$$

For simplicity, the temporal shape of the laser pulse will be assumed to be a rectangle of duration τ_L. Hence, the limits of the range integration of equation (9) are $c(t-\tau_L)/2$ to $ct/2$. Furthermore, the range of interest is much larger than the pulse duration. Thus, the range dependent parameters can be treated as constants over the small interval of the range integration. Then, the total received power at a time $t = 2R/c$ can be expressed in the form

$$P(\lambda,t) = A_o\eta(\lambda)\cdot\beta(\lambda_L,\lambda,R)\cdot T(\lambda,R)\cdot\xi(R)\cdot I(R)\cdot A_L(R)\frac{c\tau_L/2}{R^2}. \qquad (10)$$

For a rectangular laser pulse of duration τ_L, the intensity is given by

$$I(R) = \frac{E_L T(\lambda_L,R)}{\tau_L A_L(R)}, \qquad (11)$$

where E_L is the output energy of the laser pulse and $T(\lambda_L,R)$ is the atmospheric transmission factor at the laser wavelength to range R. From the Beer-Lambert law, the transmission factors in equations (10) and (11) are given by

$$T(\lambda_L,R) = \exp\left(-\int_0^R \kappa(\lambda_L,R)dR\right) \qquad (12)$$

where $\kappa(\lambda_L,R)$ is the atmospheric attenuation coefficients at the laser wavelength, λ_L.

The increment of radiation energy at wavelength λ_L received by the detector during the interval $(t, t+\tau_d)$, where τ_d is the integration period for the detector, is given by

$$E(\lambda,R) = \int_{2R/c}^{\tau_d+2R/c} P(\lambda,t)dt. \qquad (13)$$

Combining equations (10), (11), (12) and (13) yields the scattered laser energy received within the response time of the detector, τ_d:

$$E(\lambda,R)=E_L\eta(\lambda)\cdot T(R)\cdot\xi(R)\frac{A_o}{R^2}\beta(\lambda_L,R)\frac{c\tau_d}{2}. \tag{14}$$

Equation (14) is known as the basic scattering lidar equation.

For more general laser pulse shapes, the average power in the laser pulse is given by

$$P_L=\frac{E_L}{\tau_L}, \tag{15}$$

then equation (14) can be written in the form using equation 12 as

$$P(\lambda,R)=P_L\frac{A_o}{R^2}\eta(\lambda)\cdot\xi(R)\cdot\beta(\lambda_L,R)\frac{c\tau_L}{2}\cdot\exp\left(-\int_0^R\kappa(\lambda_L,R)dR\right), \tag{16}$$

where $\kappa(\lambda_L,R)$ is the two-way attenuation coefficient. Equation (16) is the a special case of scattering lidar equation assuming elastic scattering, (Mie or Rayleigh), where the wavelength of the observed radiation is the same as that of the laser wavelength. This equation is used in the differential absorption lidar technique.

2.2. The DIAL Equation

Differential absorption lidar (DIAL) is a powerful technique used to selectively measure the density of specific molecules in the atmosphere as a function of altitude. This technique uses two laser pulses of slightly different wavelengths called the on-line wavelength (λ_{on}) and a wavelength that is less absorbed by ozone, which is called the off-line wavelength (λ_{off}) as shown in Fig. 2.1. Both wavelengths are assumed to experience the same molecular atmospheric scattering, but due to the difference in ozone cross-section, the on-line wavelength experiences more ozone absorption than the off-line wavelength. Thus, the difference in the on and off-line signal returns as a function of range is a measure of the atmospheric ozone present.

The derivation of the DIAL technique starts by considering the scattering lidar equation (16) and modifying the total attenuation coefficient κ(λ,R)to

$$\kappa(\lambda, R) \equiv \kappa'(\lambda, R) + N(R)\sigma(\lambda), \tag{17}$$

where κ'(λ,R) is the attenuation coefficient exclusive of the absorption contribution from the molecular of interest or ozone, N(R) is the number density of the molecular species or ozone at range R, and σ(λ) is the absorption cross section at wavelength λ. Therefore, applying the lidar equation (16) at both the on and off-line wavelengths respectively, we get

$$P(\lambda_{on}, R) = P_L\,|_{On}\,\frac{A_o}{R^2}\eta(\lambda_{on})\xi(R)\beta(\lambda_{on}, R)\frac{c\tau_L}{2}\exp\left(-2\int_0^R [\kappa'(\lambda_{on}, R) + N(R)\sigma_{on}(\lambda_{on})]dR\right) \tag{18}$$

$$P(\lambda_{off}, R) = P_L\,|_{Off}\,\frac{A_o}{R^2}\eta(\lambda_{off})\xi(R)\beta(\lambda_{off}, R)\frac{c\tau_L}{2}\exp\left(-2\int_0^R [\kappa'(\lambda_{off}, R) + N(R)\sigma_{off}(\lambda_{off})]dR\right) \tag{19}$$

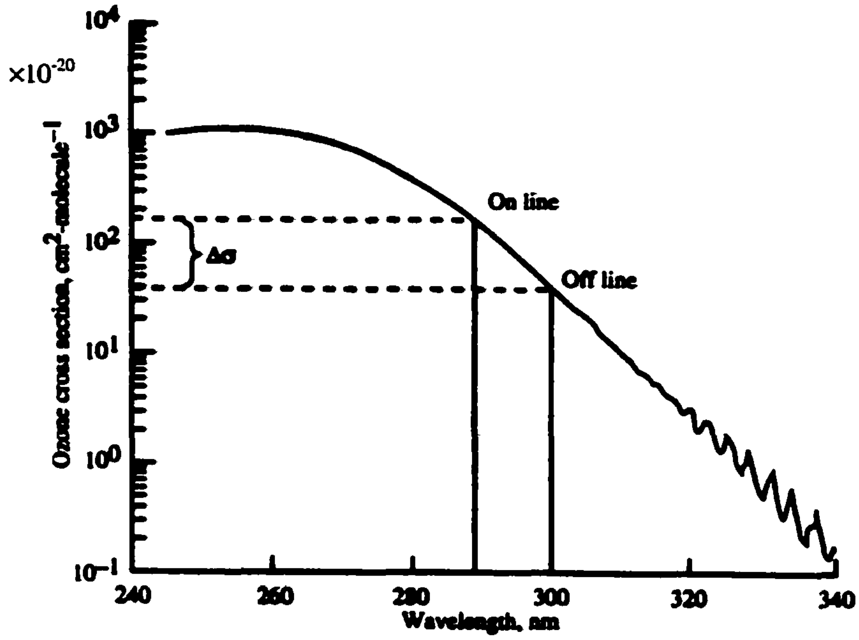

Fig. 2.1 Absorption cross section of zone with typical on-line and off-line wavelengths at 289 and 300 nm, respectively [4].

Then, the ratio of the return signals at the two wavelengths is obtained by dividing equation (18) by (19) to obtain

$$\frac{P(\lambda_{on},R)}{P(\lambda_{off},R)} = \exp\left(-2\int_0^R N(R)\Delta\sigma dR\right), \qquad (20)$$

where the difference between the on and off-line wavelengths is approximately 11 nm. Therefore, one can assume that the receiver spectral transmission factor is independent of wavelength over this small interval and similarly for the volume backscattering coefficients and atmospheric attenuation coefficients. Also, the output laser power is assumed equal for both wavelengths, and $\Delta\sigma = \sigma_{on}-\sigma_{off}$ is the differential absorption cross section.

To evaluate the integration in equation (20), two successive ranges, R_1 and R_2 are used respectively, to obtain

$$\frac{P(\lambda_{on},R_1)}{P(\lambda_{off},R_1)}=\exp\left(-2\int_0^{R_1}N(R)\Delta\sigma dR\right) \tag{21}$$

$$\frac{P(\lambda_{on},R_2)}{P(\lambda_{off},R_2)}=\exp\left(-2\int_0^{R_2}N(R)\Delta\sigma dR\right). \tag{22}$$

Therefore,

$$2\Delta\sigma\int_{R_1}^{R_2}N(R)dR=\ln\left[\frac{P(\lambda_{on},R_1)P(\lambda_{off},R_2)}{P(\lambda_{off},R_1)P(\lambda_{on},R_2)}\right]. \tag{23}$$

The ozone number density can be assumed constant in the small interval $\Delta R=R_2-R_1$, which defines the range cell as shown in Fig. 2. Hence, we get

$$N(R)=\frac{1}{2\Delta\sigma\Delta R}\ln\left[\frac{P(\lambda_{on},R_1)P(\lambda_{off},R_2)}{P(\lambda_{off},R_1)P(\lambda_{on},R_2)}\right]. \tag{24}$$

Equation (24) is known as the differential absorption lidar or DIAL equation, and it is used to obtain the number density of ozone molecules as a function of range.

Equation (24) shows that the DIAL equation is not affected by the pulse power P, as long as a return signal from both on- and off-line beams is received for every calculated altitude. The calculation is based on the slopes of the lidar returns within a range cell (R_1-R_2) as shown in Fig 2.2. The DIAL calculation of ozone gets more accurate with increasing range cell.

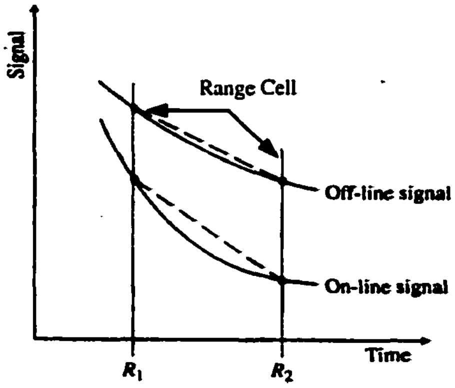

Fig. 2.2 On- and off line signal return within range cell (R_2-R_1) used to determine ozone concentration. The DIAL technique assumes a constant slope between R_2 and R_1. The on-line signal is always lower due to the increased absorption by ozone over the off-line signal [4].

References:

1. Schoulepnikoff, L.; Van Den Bergh, H.; Calpini,B; and Mitev, V.; Tropospheric Air pollution Mointering LIAR. *Encyclopedia of Environmental Analysis and Remediation*, Robert A. Meyers, Ed., John Wiley & Sons, Inc., 1988, pp.4873-4909.
2. Raymond Measures, *Laser Remote Sensing; Fundamental and Application*, John Wiley & Sons, Inc., New York (1984).
3. Browell, S. Ismail, W.B. Grant, "Differential absorption lidar (DIAL) measurements from air and space," *Appl. Phys. B* Vol.67, P399-410, 1998.
4. S. Goldschmidt, R.J.DeYoung, NASA/TM-1999-209716.

CHAPTER III

HISTORY AND BACKGROUND OF TI:SAPPHIRE LASER SYSTEM

In this chapter we will briefly discuss the history of the Ti:sapphire laser, its advantages over the other lasers and its suitability for constructing a laser transmitter to measure atmospheric ozone. Then we will furnish a background about the laser injection seeding and third harmonic generation processes.

3.1. History of Ti:sapphire laser

With the development of tunable lasers based on solid-state crystals, an opportunity exists for constructing an energetic tunable laser which can meet the requirements of aircraft based applications. The Ti:sapphire ($Ti:Al_2O_3$) laser is an attractive candidate for remote sensing since it has demonstrated a wide tuning range, including the wavelength region from 729 to 939nm [1]. The laser was first demonstrated in 1982 by Peter Moulton [2] at MIT Lincoln laboratory and many papers since then have reported the spectroscopic and laser characteristic of $Ti:Al_2O_3$ as a lasing material [3-7].

Since that time much effort has been made to build a Ti:sapphire laser system for remote sensing measurements as well as other applications. In 1987 Moulton [1] reported a design of a narrow-linewidth $Ti:Al_2O_3$ ring oscillator. He used the injected-locked technique to obtain a narrow linewidth (single frequency). This laser system did not offer the compactness that is needed in the laser transmitter DIAL system and the output energy of the laser was only 5 mJ.

In 1993 NASA Langley deployed the Lidar Atmospheric Sensing Experiment (LASE) [8] using a Ti:sapphire laser system to measure atmospheric water vapor. Since then this airborne DIAL system, with a Ti:sapphire laser transmitter at 815 nm [10], has been frequently operated to measure H_2O distributions throughout both the lower and upper atmosphere [9]. To date, there are no Ti:sapphire laser systems or designs that can meet all the ozone DIAL measurement characteristics.

3.2. Advantage of Ti:Sapphire laser.

The Ti:Sapphire (Ti:Al_2O_3) laser is an attractive candidate for remote sensing since it has demonstrated a wide tuning range including a wavelength regions from 729-939nm [2, 7]. Ti:sapphire has a relatively large gain cross section which is half of Nd:YAG at the peak of its tuning range, and is a rugged all-solid-state system. In a Ti:sapphire crystal, titanium is doped in sapphire, where the Ti^{3+} ion is substituted for the Al^{3+} ion in the Al_2O_3 laser crystals and are typically doped with 0.1 % Ti^{3+} by weight. The isolated Ti^{3+} ion has a single d electron in its outer orbit. When the Ti^{3+} ion is introduced into the sapphire host, the energy level of d electron splits into two levels [10], as shown in Fig. 3.1. Light in the blue-green region is absorbed by the ground state of the titanium ion causing it to excite the ^2E_g configuration. Then through a very fast phonon emission process, the ion shifts position in the lattice to the metastable position of the lowest ^2E_g excited electronic state. Stimulated emission occurs between the ^2E_g excited and $^2T_{2g}$ ground electronic states, followed by multiple phonon emissions, which transfer the ion back to the lowest energy position of the ground electronic state. A relatively weak absorption band is observed in the IR region, at the lasing wavelength. It has been shown that this absorption is caused by Ti^{3+}- Ti^{4+} ion pairs [11] and this residual IR absorption interferes with efficient laser operation. Optimized crystal growth techniques and additional annealing processes have drastically reduced this absorption band compared to earlier crystals [11]. Loss at the lasing wavelength in Ti:sapphire is characterized by a figure-of-merit, FOM, which is defined as the absorption coefficient at the peak of the pump absorption, about 490 nm to the absorption coefficient at the peak of the gain, about 800 nm. A typical value of FOM for the Ti:sapphire crystal used in our experimental setup is 250. It has been shown that the absorption at the lasing wavelengths increased quadratically with the Ti^{4+} concentration [12].

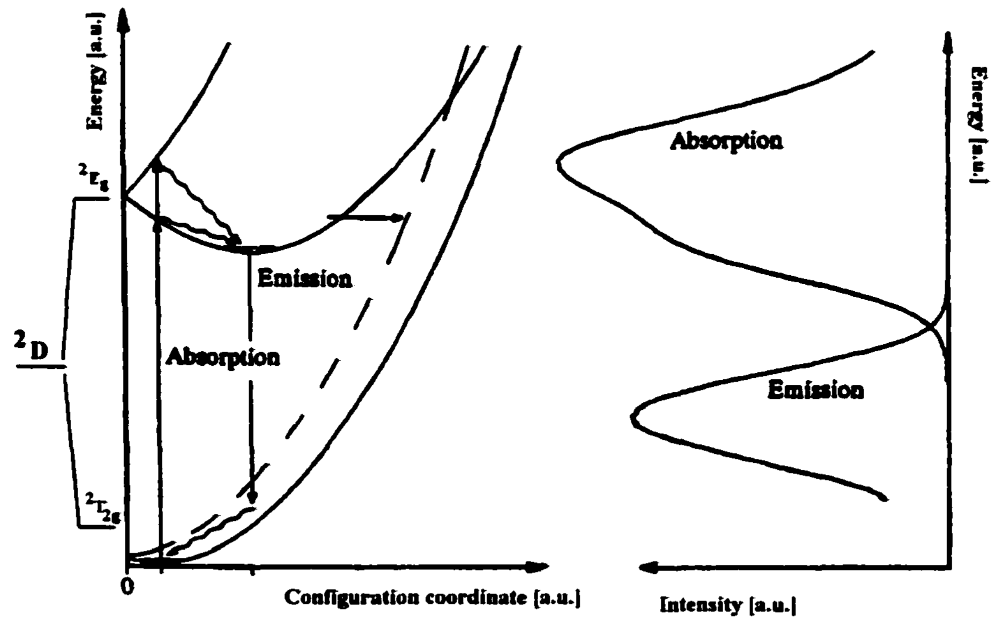

Fig. 3.1 Energy level diagram for Ti^{3+} in sapphire, showing the excitation process followed by phonon-assisted relaxation of the metastable excited state. The dashed line represents emission in the near infrared. Also shown are the corresponding absorption and emission curves. [13]

The absorption and emission curves for the Ti:sapphire crystal are shown in Fig. 3.2. The absorption and fluorescence bands are broad and widely separated due to the strong coupling between the Ti ion and host lattice, which is key to a broadly tunable laser.

Having the absorption peak of the Ti:sapphire laser at ~490 nm, makes the Nd:YAG laser at 532nm the best pumping source. The kinetic efficiency of converting a 532 nm pump photon into an inverted upper laser level is approximately 1 [11].

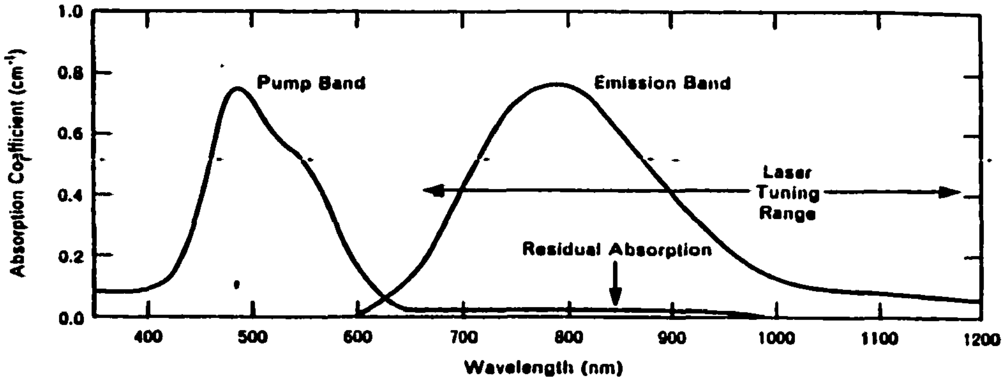

Fig. 3.2 The emission and absorption bands of Ti:Al_2O_3. [7]

The Ti:sapphire crystal is transparent from the ultraviolet to the infrared. The excellent mechanical, thermal, and optical properties of Ti:sapphire allow laser designs to be scaled to high average powers, and high efficiency. The laser parameters of the Ti:sapphire are listed in table 3.1.

Table 3.1 Laser parameters of Ti:sapphire [11]

Index of refraction	$n=1.76$
Fluorescent lifetime	$\tau = 3.2$ µs
Fluorescent linewidth (FWHM)	$\Delta\lambda \sim 180$ nm
Peak emission wavelength	$\lambda_p \sim 790$ nm
Peak stimulated emission cross section	
parallel to c axis	$\sigma_{p\parallel} \sim 4.1 \times 10^{-19}$ cm^2
perpendicular to c axis	$\sigma_{p\perp} \sim 2.0 \times 10^{-19}$ cm^2
Quantum efficiency of converting 532 nm pump photon into an inverted site	$\eta_Q \approx 1$
Saturation fluence at 795 nm	$E_{sat} = 0.9$ J/cm^2
Figure of merit	250
Absorption coefficient	1.67 cm^{-1}
Damage threshold	10 J/cm^2
Thermal conductivity	0.35 W/cm .K

When compared to the dye laser, the Ti:Sapphire laser has significant advantages in the development of high power and high efficiency. Being a solid-state gain medium it produces a stable and excellent optical quality laser, which is easy to operate and maintain. The upper state lifetime (3.2 µs) is longer than that of dye lasers; hence, more energy can be stored yielding pulses with higher peak powers. In the near infrared region the active medium solvents of many dye lasers are capable of handling significantly less power resulting in a lower output. In the case of dye lasers, typically four different dyes are needed to cover a spectral region from 660 to 1000 nm, each having a tuning range of about 120 nm, while the Ti:sapphire crystal covers the whole spectral range.

The upper state lifetime of the Ti:sapphire laser crystal is sensitive to temperature as shown in Fig. 3.3. This lifetime has a constant value up to 200 K, and then there is a clear reduction in the lifetime with increasing temperature. At room temperature the upper state laser lifetime is 3.2 µs. To have efficient laser performance, it is important to keep the temperature of the laser crystal near room temperature.

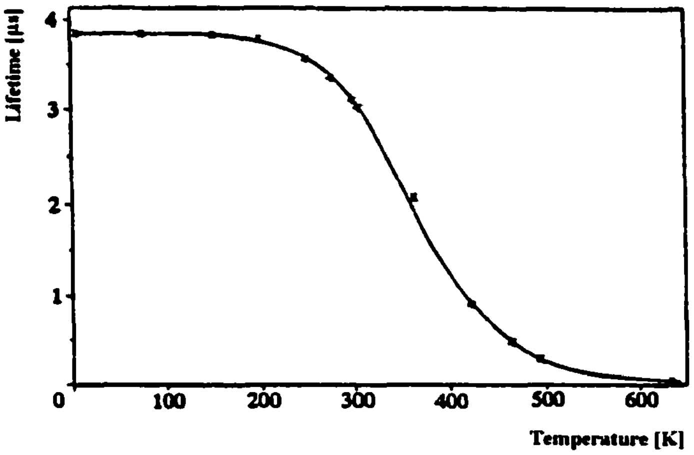

Fig. 3.3 Lifetime of the upper laser level of Ti:sapphire as function the temperature [14].

Ti:sapphire lasers have been pumped with a number of sources such as argon and copper vapor lasers, frequency doubled Nd:YAG and Nd:YLF lasers, as well as flashlamps. Flashlamp and diode pumping are difficult to use in the Ti:sapphire laser because a very high pump flux is required. The reason for that is the short fluorescent lifetime of 3.2 μs which results in a small product of stimulated emission cross-section times fluorescent lifetime ($\sigma.t_f$). The population inversion in a laser required to achieve threshold is inversely proportional to $\sigma.t_f$ [11].

A low laser threshold can be obtained by using laser pumping. For pulsed laser operation the most commonly used pump laser is the frequency doubled Nd:YAG laser. Because the beam quality of the pump can be relatively good, the pump radiation can be focused to a small beam radius. Thus in the volume of the pumped region, the inversion can be high even at relatively low pump energies. Coupled with a high effective stimulated emission cross section, gain in the pumped volume can then be high. By matching the mode radius of the Ti:sapphire oscillator to the pumped region, the gain of the lasing mode can be high and thus the threshold low. However, the use of a small pump beam radius will limit the amount of energy available from the Ti:sapphire laser, and exposing very small crystal areas to high energy pump pulses will result in laser induced damage. Although the laser induced damage threshold of this crystal is relatively high, the small pump beam radii will limit the amount of pump energy that can be used and thus the amount of laser output energy. Consequently, the pump beam radius is adjusted to accommodate the desired laser output energy without incurring laser-induced damage.

Using a frequency-doubled Nd:YAG pump laser has the additional benefit of producing a short Ti:sapphire output pulse, much like a Q-switched pulse. To achieve efficient frequency doubling, the Nd:YAG laser is usually Q-switched, where the pump pulse is short compared to the Ti:sapphire cavity buildup time. A short pump pulse produces gain-switched laser operation, though different than Q-switching; however, the effect is the same. With gain switching, the cavity gain varies quickly while with Q-switching the laser cavity loss varies quickly. In either case, a short pulse laser output is produced on the order of nanoseconds. For practical purposes, the dynamics of the pulse evolution for gain switching or Q-switched operation can be described using the same formulism.

3.3. Ti:sapphire laser cavity design.

As mentioned above when a Nd:YAG laser pumps Ti:sapphire, a gain-switched, single-pulse output will result from the Ti:sapphire system. Historically, experiments with gain-switched Ti:sapphire oscillators began with a stable resonator [15-17]. However, the stable resonator at that time could not provide more than tens of milli-jouls of diffraction limited output energy before reaching the optical damage limit. Rines and Moulton in 1990 [18] studied the performance of gain-switched Ti:sapphire unstable-resonator lasers in order to obtain high energy output. They conducted a series of experiments with positive branch, confocal unstable resonators in standing and ring cavity configurations. They investigated three types of output coupler mirrors for unstable resonators using special optics, namely, a high-reflectivity dot mirror (HRDM), a partial reflectivity dot mirror (PRDM), and a graded-reflectivity mirror (GRM). Since then, many unstable Ti:sapphire laser cavities have been reported, some of them using special optics like GRMs [19-25].

A flat-flat mirror resonant laser cavity with a high reflector and an output coupler mirror has been chosen to configure our laser cavity. This configuration has been chosen on the bases of the gain guiding effect which was introduced by Salin and Squier [26]. The gain guiding effect, induced in a solid-state medium pumped by another laser, can be used to produce high quality, near-diffraction limited, high energy beams of arbitrary large diameter from unstable resonators [27]. In turn, this results in better conversion efficiency in the nonlinear crystals used to triple the Ti:sapphire output. High energy from Ti:sapphire lasers is limited by the damage problems arising from the very high fluences that are often achieved in stable resonators. High energy and good spatial characteristics have been obtained in an unstable resonator using a graded reflectivity mirrors (GRM) [18-25]. However, this design requires specialized optics whereas with the gain guiding method a simpler design for the laser cavity, without a GRM output coupler, can be used. Additionally, it has been shown that there are advantages to designing a cavity with the gain guiding approach rather than a cavity with a GRM output coupler such as standard uniform-reflectivity mirrors can be used, which means the output beam preserves the quality of the intercavity beam, the size of the laser beam (i.e., the gain profile) can be continuously adjustable by varying the pump-beam size. Since the laser beam size scales with the pump size, high-energy laser-pumped solid state lasers such as Ti:sapphire are feasible [27]. It has been found that the most efficient gain guiding resonator is flat-flat resonator [26, 27].

3.4. Laser injection seeding for narrow linewidth operation.

Laser injection seeding provides a linewidth-narrowing mechanism for the Ti:Sapphire. For many applications, the narrow spectral linewidth and improved beam quality that result from seeding are important in themselves. For this application, the primary motivation for injection seeding is higher third harmonic conversion efficiency up to 30% in the seeded regime.

Injection seeding refers to the process of achieving single mode operation of a pulsed laser by injecting radiation from a very narrow linewidth "seed" laser into the pulsed laser cavity. For injection seeding to work properly, it is important that the seed laser emission be orders of magnitude more intense than any spontaneous noise emission also present in the laser cavity.

When the seed laser frequency is within the bandwidth of a pulsed cavity mode (i.e., it is resonate with the laser cavity mode) a pulse will develop more rapidly out of narrow band "seed" emission than it can out of background spontaneous broad band noise emission. Consequently, the pulse developing out of the seed will saturate the gain medium and extract the energy (thereby depleting the gain) before the pulse, which is simultaneously trying to grow out of noise emission, is able to do so. In this way all of the energy stored in a homogeneously broadened gain medium [11] such as Ti:sapphire is depleted by the pulse which developed from the seed laser source, resulting in a single frequency output from the pulsed laser.

The injection-seeded oscillator has advantages over other methods of producing a narrow linewidth high-energy laser pulse. One of the primary advantages is the relative ease of control of the seed laser output. In general, it is easier to control the spectral properties of a low output power seed laser rather than a high output pulsed laser.

Several researcher have reported on the injection seeding of pulsed Ti:sapphire lasers [28-34]. Most of them used continues wave (cw) diode lasers as an injection source.

3.5. Frequency conversion

Nonlinear optical devices, such as harmonic generators, parametric oscillators, and stimulated Raman shifting, provide a means of extending the frequency range of available laser sources [11, 35-37]. Frequency conversion is a useful technique for extending the utility of high power lasers. It utilizes the nonlinear optical response of an optical medium in intense radiation fields to generate new frequencies. It includes both elastic process (optical-energy-conserving) processes, such as harmonic generation, and inelastic processes (which deposited some energy in the medium), such as stimulated Raman.

There are several commonly used elastic processes. Frequency doubling, tripling, and quadrupling generate a single harmonic from a given fundamental high power source. The processes of sum-and difference- frequency generation also produce a single wavelength, but require two high-power sources. These processes have been used to generate high-power radiation in all spectral regions. Optical parametric oscillators and amplifiers generate two waves of lower frequency. They are capable of generating a range of wavelengths from a single frequency source, in some cases covering the entire visible and near-infrared regions.

For inelastic processes, Raman process can be utilized in solid-state lasers for the generation of additional spectral output lines. The strongest interaction is for the output shifted towards a longer wavelength (first Stokes shift), but at sufficiently high pump intensities additional lines at longer as well as shorter wavelength with respect to the pump wavelength will appear (Stokes and anti-Stokes line).

NASA Langley research center is exploring many approaches of generating UV sources to measure ozone from different platforms, aircrafts, and satellites. These approaches use, OPO, mixing, doubling and tripling, and stimulated Raman scattering to generate UV sources for ozone measurements.

For the case of Ti:sapphire laser, many scenarios are available for the development of highly efficient solid-state sources of coherent radiation tunable in the UV and the short visible spectral range. That is owing to the availability of nonlinear crystals that can be phase matched for second harmonic generation (SHG) and third harmonic generation (THG) of the Ti:sapphire laser tuning range. There were two candidate crystals that can be phase matched for SHG and THG over the entire

Ti:sapphire laser tuning range, and in addition have broad transparency, as shown in Fig. 3.4 and high damage resistance needed for use with the high peak-power, pulsed Ti:sapphire lasers. These crystals are namely LiB_3O_5 (LBO) and BaB_2O_4 (BBO).

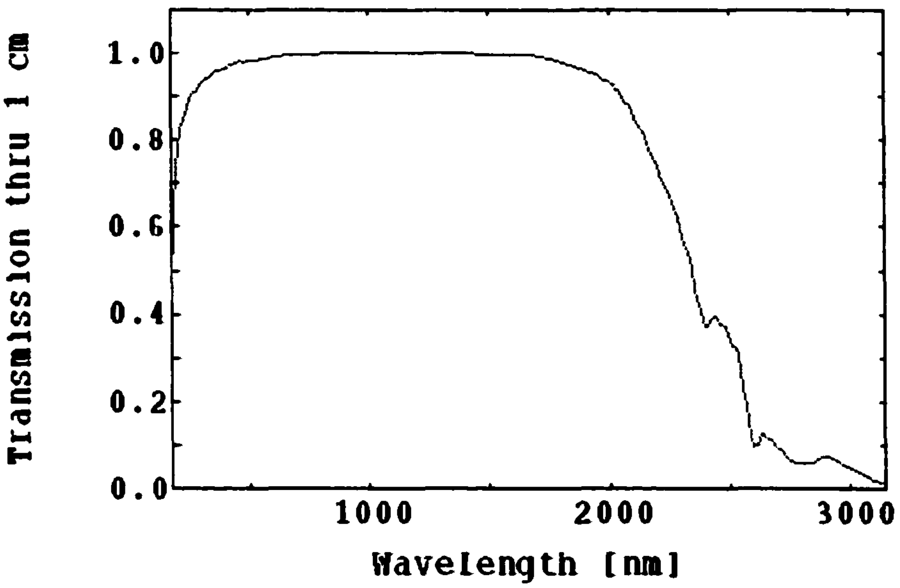

Fig. 3.4. Broad transparency of LBO crystals [38]

A few measurements have indicated that the LiB_3O_5 (LBO) crystal has several advantages compared with the relatively higher nonlinear coefficient crystal BaB_2O_4 (BBO), when applied to higher peak power Ti:sapphire laser frequency conversion [39]. These advantages relate to LBO's high damage threshold, smaller walk-off angle, larger angular bandwidth, larger acceptance angle, and nonhydroscopic nature. These features suggest that LBO could also be a better material than BBO for efficient frequency conversion of Ti:sapphire lasers at high peak powers, thus offering a tunable UV/blue coherent source in the range of 350-450 nm [40, 41]. LBO is a negative biaxial crystal in which the principle axes x, y, and z are parallel to the crystallographic axes a, c, and b, respectively, and $n_z > n_y > n$ [42, 43], see table (3.2,3.3).

Table 3.2 Main characteristics of SHG used in the present system [38]

Crystal	LBO
Temperature	300 K
Type of interaction	Type I, ooe
Square aperture, mm	5x5
Length, mm	20
Central wavelength, nm	867, 900
Cut angle: theta, degree	90
Cut angle: phi, degree	23
d_{eff}, pm/V	0.785, 0.798
Acceptance angle, mrad-cm	3.8, 4.31
Acceptance bandwidth, cm^{-1}-cm	34.34, 38.65
Temperature range, K°-cm	8.3, 7.73
Walkoff, mrad	12.99
Damage threshold (@ 1064 nm, 10ns)	2.5 GW/cm^2

Table 3.3 Main characteristics of SFG used in the present system [38]

Crystal	LBO
Temperature	300 K
Type of interaction	Type I, ooe
Square aperture, mm	5x5
Length, mm	20
Central wavelength, nm	867, 900
Cut angle: theta, degree	90
Cut angle: phi, degree	55
d_{eff}, pm/V	0.468, 0.536
Acceptance angle, mrad-cm	(3.14, 1.55), (3.03, 1.50)
Acceptance bandwidth, cm^{-1}-cm	(9.10 17.26), (9.99, 18.95)
Temperature range, K°-cm	5.61, 8.39
Walkoff, mrad	17.14, 18.48
Damage threshold (@ 1064 nm, 10ns)	2.5 GW/cm^2

References:

1. Moulton, NASA contractor Report 4093, "Titanium-doped sapphire laser research study," September 1987.
2. P.F. Moulton, Opt. News 8, 9 (1982).
3. G. F. Albercht, J. M. Eggleston and J. J. Ewing, "Measurements of Ti:Al_2O_3 as a lasing material," *Opt. Commun.*, Vol.52, no.6, 401-404, 1985.
4. P. Lacovara, L. Esterowitz, and M. Kokta, "Growth, spectroscopy, and lasing of titanium-doped sapphire," *IEEE J. of QE*, vol. QE-21, no. 10, 1614-1618, 1985.
5. Moulton, *J. Opt. Soc. Am. B*, Vol.3, no.1, 1986.
6. Antonio, *IEEE J. of QE*, vol. 24, no. 6, 1988.
7. K. F. Wall; A. Sanchez, "Titanium sapphire lasers," *The Lincoln Laboratory Journal*, vol. 3, no. 3, 447-462, 1990.
8. J. C. Barnes, W. C. Edwards, L. B. Petway, and L. G. Wang, "NASA lidar atmospheric sensing experiment's titanium-doped sapphire tunable laser system" in *OSA Optical Remote Sensing of the Atmosphere, Technical Digest* 5:459-565 (1993).
9. R. Ferrare, S. Ismail, E. Browell, V. Brackett, S. Kooi, M. Clayton, P. V. Hobbs "Comparisons of LASE, aircraft, and satellite measurements of aerosol optical properties and water vapor during TARFOX," *J. Geophys. Res.*, 105, 9935-9947, 2000.
10. C.E. Byvik and A. M. Buoncristiani " Analysis of vibronic transitions in titanium doped sapphire using the temperature of the fluorescent spectra," *IEEE, QE-21*, No. 10, 1619-1623, (1985).

11. W. Koechner, *Solid State Laser Engineering* (Springer-Verlag, New York, 1988).

12. F.J. Durate, *Tunable Lasers Handbook*, (Academic press, New York, 1995).

13. Hoffstat, "Bestimung des Spektralen wirkungrades eines gepulsten Ti:sapphire lasers," Diplomarbeit, Fechbreich physik, Techniscene Universitat Berline (1991).

14. P. Albers, E. Stark and Gtluber, "Continous-wave laser operation and quantum efficiency of titanium-dopped sapphire," J. Opt. Soc. Am. B. 3(1), 134-139 (1986).

15. N. P. Barnes and D. K. Remelius, *Tunable Solid-State Lasers For Remote Sensing*, (Stanford U. Press, Stanford, Calif., 1984), Vol 51, pp. 78-81.

16. G. F. Albercht, J. M. Eggleston and J. J. Ewing, "Measurements of Ti:Al_2O_3 as a lasing material," *Opt. Commun.*, Vol.52, no.6, 401-404, 1985

17. P. F. Moulton, *J. Opt. Soc. Am. B* 3, 125 (1986).

18. Glen A. Rines and Peter F. Moulon, " Performance of gain-switched Ti:sapphire unstable-resonator lasers," *Opt. Lett.*, Vol. 15, No. 8, (1990).

19. Chalres E. Hamilton, "Single-frequency, injection-seeded Ti:sapphire ring laser with high temporal precision," *Opt. Lett.*, Vol 17, No. 10, 1992.

20. T. D. Raymond and V. Smith, " Injection-seeded titanium-doped-sapphire laser," *Opt. Lett.*, 16, 33, (1991).

21. N. Finkelestein, W. R. Lempert, and R. B. Miles, "Narrow-iinewidth passband filter for ultraviolet rotational Raman imaging," *Opt. Lett.* Vol. 22, No. 8, (1997).

22. T. R. Steele, D. C. Gerstenberger, A. Drobshoff, and R. W. Wallace, "Broadlt tunable high-power operation of an all-solid-state titanium-doped sapphire laser system," *Opt. Lett.*, Vol 16, No. 6, (1991).

23. J. C. Barnes "Solid State Laser Technology Development For Atmospheric Sensing Applications," in *Proceedings of the 19th International Laser Radar Conference (ILRC)*, Upendra N Singh, Syed Ismail and Geary K. Schwemmer (eds.), (NASA, Annapolis 1998) pp. 619-622.
24. J. C. Barnes, W. C. Edwards, L. B. Petway, and L. G. Wang, "NASA lidar atmospheric sensing experiment's titanium-doped sapphire tunable laser system" in *OSA Optical Remote Sensing of the Atmosphere, Technical Digest* 5:459-565 (1993).
25. A. S. Moore, Jr., K. E. Brown, W. M. Hall, J. C. Barnes, W. C. Edwards, L. B. Petway, A. D. Little, W. S. Luck, Jr., I. W. Jones, C. W. Antill, Jr., E. V. Browell, and S. Ismail, "Development of the Lidar Atmospheric Sensing Experiment (LASE)-An Advanced Airborne DIAL Instrument" in *Proceedings of the 18th International Laser Radar Conference (ILRC)*, A. Ansmann (ed.) (Springer-Verlag, Berlin, 1996), pp. 281-288.
26. F. Salin, J. Squier, "Gain guiding in solid-state lasers," *Opt. Lett.* 17, 1352(1992).
27. F. Salin, F. Estable, E. Mottay, and L. Brunel, " High-Power, Gain Guided Ti:AL_2O_3 Laser: Theory and Experiment", *OSA proceedings on advanced solid-state lasers*, Albert A. Pinto and Tso Yee Fan, (eds.), (New Orleans, Louisiana, February 1-3, 1993), p294.
28. T.D. Raymond, A.V. Smith, "Injection-seeded titanium-doped sapphire laser," *Opt. Lett.* 16, 33 (1991).

29. N. J. Vasa, M Tanaka, T. Okada, M. Maeda, O. Uchino," Comparative study of narrowing of pulsed Ti:Sapphire laser using pulsed and CW injection seeding," *Appl. Phys. B* 62, 51-57 (1996).

30. C. H. Bair, P. Brockman, R. V. Hess, E.A. Moldin "Demonstration of frequency control and cw diode laser injection control of titanium-doped sapphire ring laser with no internal optical elements," *IEEE J. QE* 24, 1045 (1988).

31. P. Brockman, C.H. Bair, J.C. Barnes, R.V. Hess, E.V. Browell, "Pulsed injection control of a titanium-doped sapphire laser," *Opt. Lett.* 11, 712(1986).

32. M.R.H. Knowles, C.E. Webb, "Cavity configuration for copper vapor laser pumped titanium sapphire lasers," *Opt. Commun.* 89, 493(1992).

33. Y. Boucher, P.Georges, A. Burn, J.P. Pocholle, M. Papuchon, "Seeding of a Ti:Al_2O_3 laser by vertical cavity surface-emitting laser in the nanosecond range," *Tech Dig. CLEO* '94 (1994) p 124.

34. Charles E. Hamilton, "Single-frequency, injection-seeded Ti:sapphire ring laser with high temporal precision," *Optics Letter* Vol. 17, No. 10, p728, 1992.

35. N. Bloembergen : Nonlinear Optics (Benjamin, New York 1965).

36. W. Kaiser, M. Maierr: in *Laser Handbook* ed. By F. T. Arecchi, E. O. Schulz-Dubois (North- Holland, Amestrdam 1972).

37. Y. R. Shen: In light Scattering in Solids, Topics in Applied Physics, Vol. 8, ed. By M. Cardona (Springer, Berlin, Heidelberg, New York 1975).

38. SNLO nonlinear optics code available from A. V Smith at Sandia National laboratories, Albuquerque, NM 87185-1423 (2001).

39. Da-Wun Chen and J. T. Lin, "Temperature-Tuned Phase-Matching Properties of LiB_3O_5 for Ti:sapphire Laser Frequency Doubling," *IEEE Journal of Quantum Electronics*. Vol. 29, No.2, 1993.

40. A. Nebel and R. Beigang, "External frequency conversion of CW mode-locked $Ti:Al_2O_3$ laser radiation," *Opt. Lett.*, Vol. 16, pp 1729, 1991.

41. G. A. Skripko, S. G. Bartoshevick, I.V. Mikhnyuk, and I. G. Tarazevick, "LiB_3O_5, a higly efficient frequency converted for Ti:sapphire lasers," *Opt. Lett.* Vol 16, pp. 1726-1728, 1991.

42. S. Lin, Z. Sun, B. Wu, and Chen, "The nonlinear optical characteristics of LiB_3O_5 Crystal," *J. Appl Phys.*, vol67, pp. 634-638, 1990.

43. S. P. Velsko, M. Webb, L. Davis, and C. Huang, "Phase-matched harmonics generation in lithium triborate (LBO)," *IEEE J. Quantum Electron.* Vol. 27, pp. 2182-2192, 1991.

CHAPTER IV

EXPERIMENTAL SETUP OF TI:SAPPHIRE LASER

In this chapter, we will discuss the setup of the two Ti:sapphire, on-line and off-line laser systems, at wavelengths of 867 and 900 nm respectively, which will be tripled to produce 289 and 300 nm laser pulses. Both lasers have the same setup as shown in Fig. 4.1.

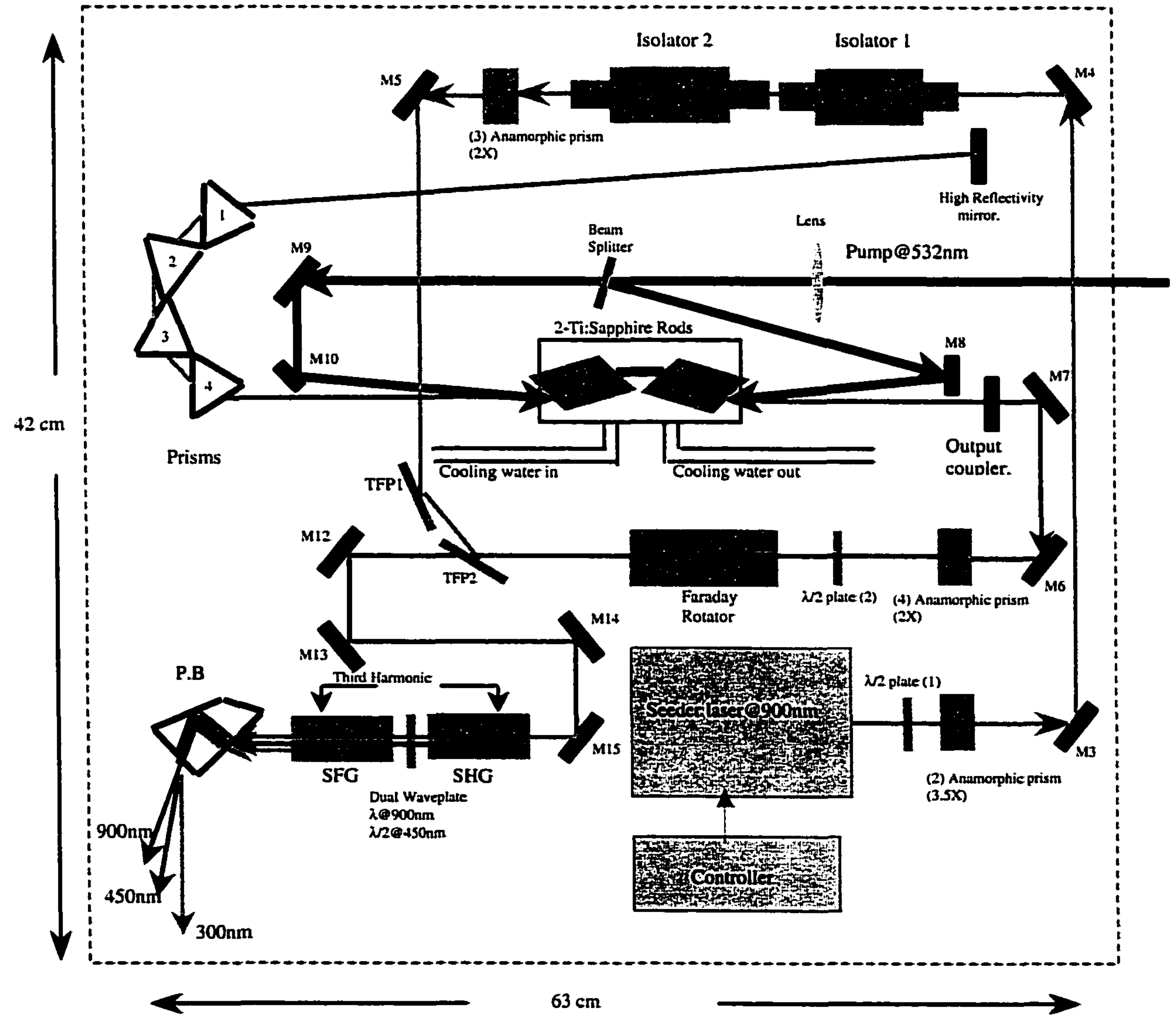

Fig. 4.1 Ti:sapphire laser layout for either 289 or 300 nm wavelength for ozone DIAL atmospheric measurements.

The method for injection seeding and how third harmonic conversion is accomplished will also be discussed. A description of each component shown in Fig. 4.1 is given in the appendix. In the following sections, the laser system is broken into subsystems, explaining step by step each subsystem and how the laser was configured to fit into a 42×63 cm^2 enclosed optical bench.

4. 1 Laser pumping of the Ti:Sapphire laser cavity

Ti:sapphire laser material (0.01% Ti by weight) was cut into Brewster angle bricks. The crystal c-axis of the laser bricks is perpendicular to the 532 nm pump beam propagation, and is parallel to the pump polarization vector. The anti-parallel Brewster faces of the two bricks serve to cancel dispersion effects and minimize damage at high pump energies. The bricks are 10-mm-diameter × 20-mm-length and were wrapped in a thin layer of indium then placed in a water cooled aluminum mount, which was thermally in contact with the Ti:sapphire crystal bricks. Thermal loading is an issue requiring that the two bricks be cooled by 26 °C flowing water. Without the water-cooling system, the mount could reach temperatures as high as 60°C when the Ti:sapphire lasers operated at a repetition rate of 30 Hz and a pump pulse energy of 475 mJ. Insufficient cooling results in clearly observable gain reduction of the Ti:sapphire bricks thus preventing high-energy pulse output from being obtained.

The pump for the Ti:sapphire oscillator was a commercial Q-switched, frequency-doubled Nd:YAG laser (Continuum 9030) producing 8 ns (FWHM) pulses and operating at a repetition rate of 30 Hz. The near flat top pump beam profile had an output diameter of ($1/e^2$) 10 mm. The 532 nm pump beam was split into two beams with a 50/50 beam splitter, as shown in Fig. 4.2, each of which was focused by a 66 cm focal length lens, to a 3.5 mm beam waist slightly beyond the two Ti:Sapphire bricks. More than 98% of the total pump beam laser energy was absorbed in the two bricks. The geometrical overlap of the pump beams and the power oscillator cavity mode was calculated to be better than 0.98 using a Gaussian beam profile approximation [1].

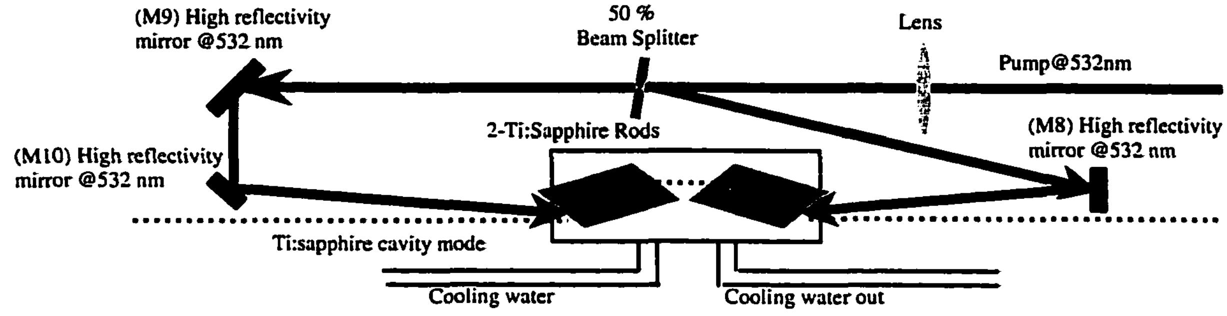

Fig. 4.2. Pumping schematic diagram of Ti:sapphire laser.

4.2. Laser Oscillator Cavity Design

The Ti:sapphire laser resonant cavity consisted of two 25.4 mm diameter flat surface mirrors on either side of the gain medium as shown in Fig. 4.3. The selection of the cavity configuration for a particular laser depends upon the following three factors: diffraction loss, mode volume, and ease of alignment. The plane parallel cavity configuration is very useful in pulsed solid-state lasers because of its large mode volume, which is the volume inside the laser cavity actually occupied by the laser beam and stimulated emission occurs only within this volume. The plane parallel cavity has high diffraction loss, but this loss is easily overcome in pulsed lasers by the high laser medium gain. Another advantage is that no focusing of the beam occurs in the laser cavity, which can damage solid laser rods and other optical components. The plane parallel cavity is makes a compact system. These four Brewster dispersion prisms provided a means of coarse wavelength selection in the region of 860 to 900 nm; without coarse wavelength selection, the laser would tend to lase at 790 nm, the peak of the Ti:sapphire gain curve causing the spectral purity to be lower. This makes the laser tunable and limits the linewidth of the unseeded Ti:sapphire laser. Each prism was set at Brewster angle for the resonant wavelength of 867 nm or 900 nm. The prisms have an apex angle of approximately 66.25 degree and an incidence angle of 56.5 degree (see Appendix). In this configuration, the output beam of the unseeded Ti:Sapphire laser was horizontally polarized for minimum loss in the prisms.

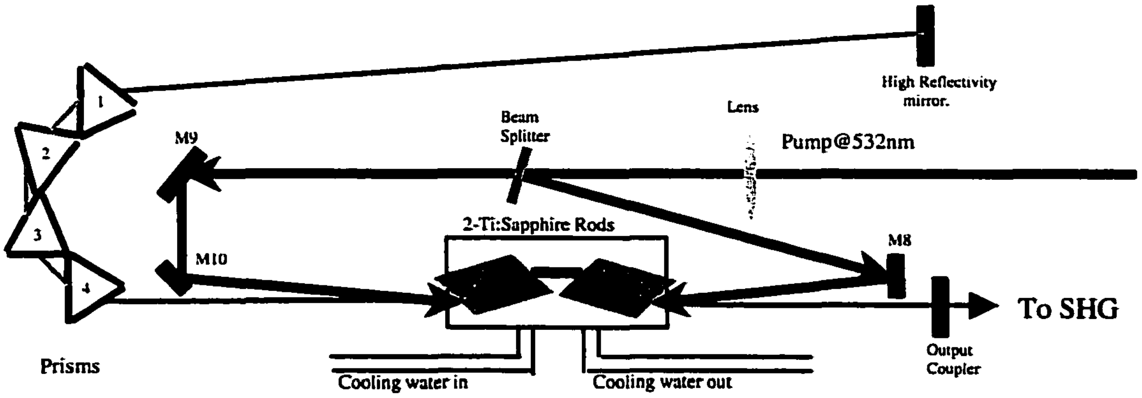

Fig. 4.3 Ti:sapphire laser cavity with dispersion prisms.

In order to achieve the best laser efficiency, it was important to put all the lossy components (eight optical surfaces in our resonator) on one side of the crystal and the output coupler on the other side as shown in Fig. 4.3, since a large part of the energy extracted occurs during the last pass in the Ti:sapphire brick.

4.3. Injection seeding of the Ti:sapphire laser

The seeder laser beam for injection seeding the Ti:sapphire laser is shown in Fig. 4.4, which consisted of two commercial, CW, single-longitudinal mode, external grating, temperature-stabilized, 5.5-mW diode lasers manufactured by Environmental Optical Sensors, Inc. (Boulder, CO). One laser is set to operate at 867nm and the other at 900 nm with a linewidth of ~3.7 MHz. The diode laser output was circularized using an anamorphic prism pair as shown in Fig. 4.4. The prisms are arranged to compress the long axis of the diode beam by a factor of 3.5. A half-wave plate orients the polarization of the diode beam for optimal transmission through the prisms. The diode laser is isolated from the Ti:sapphire laser cavity with two Faraday isolators that have a reverse attenuation of 60 db each, which is needed because of the sensitivity of the laser diode to any feedback from the Ti:sapphire laser which could destroy the cw diode laser. After the isolators, a thin film polarizer (TFP), Faraday rotator and second half-wave plate were used to reorient the polarization of the seed beam for injection into the Ti:sapphire cavity. The seed beam is injected into the cavity through the output coupler mirror. Owing to the loss in the isolators, Faraday rotator, and TFP the power of the seed beam injected inside the cavity is 2 mW at both wavelengths of 867 and 900 nm. This incident power is adequate to perform the injection seeding as the seeding operation of the Ti:saaphire laser has been demonstrated with incident powers as low as 1 mW.

The vertically polarized seeder diode laser beam (propagating towards the Ti:sapphire output coupler) is partially reflected by the TFP. The half wave plate rotates the polarization of the diode laser beam by 45 degrees. Then the Faraday rotator rotates the polarization of the diode laser beam by another 45 degrees so that this beam is now polarized horizontally. The diode laser beam is aligned to match the path of the Ti:sapphire laser beam at the corresponding wavelength.

The damage threshold of the Faraday rotator crystal was a concern at the high pulse energy. For this reason the output of the Ti:sapphire laser was reshaped by introducing an anamorphic prism pair (4) after the output coupler to compress the beam in one dimension and stretch it in the other dimension; thus, the vertical and horizontal fluence of the beam were now nearly the same. By introducing the beam shaping optics in the output beam of the Ti:saphhire laser, the damage threshold on the Faraday rotator was reduced such that the Ti:sapphire energy at the fundamental wavelength could be increased, which is favorable for increased third harmonic conversion efficiency.

The design of the Ti:sapphire laser did not incorporate any means to lock the frequency of the diode laser to the longitudinal mode frequency of the Ti:sapphire laser cavity. The temporal and spectral characteristics of the seeded and unseeded Ti:sapphire lasers have been studied and determined that without frequency locking the laser will run either on a single or two longitudinal modes as the linewidth of the seeder, 3.7 MHz, is less than the longitudinal mode spacing of the Ti:sapphire laser cavity of 107MHz. Such dual mode output is useful, since the dual mode output power is higher than single mode operation, thus leading to a higher harmonic generation conversion.

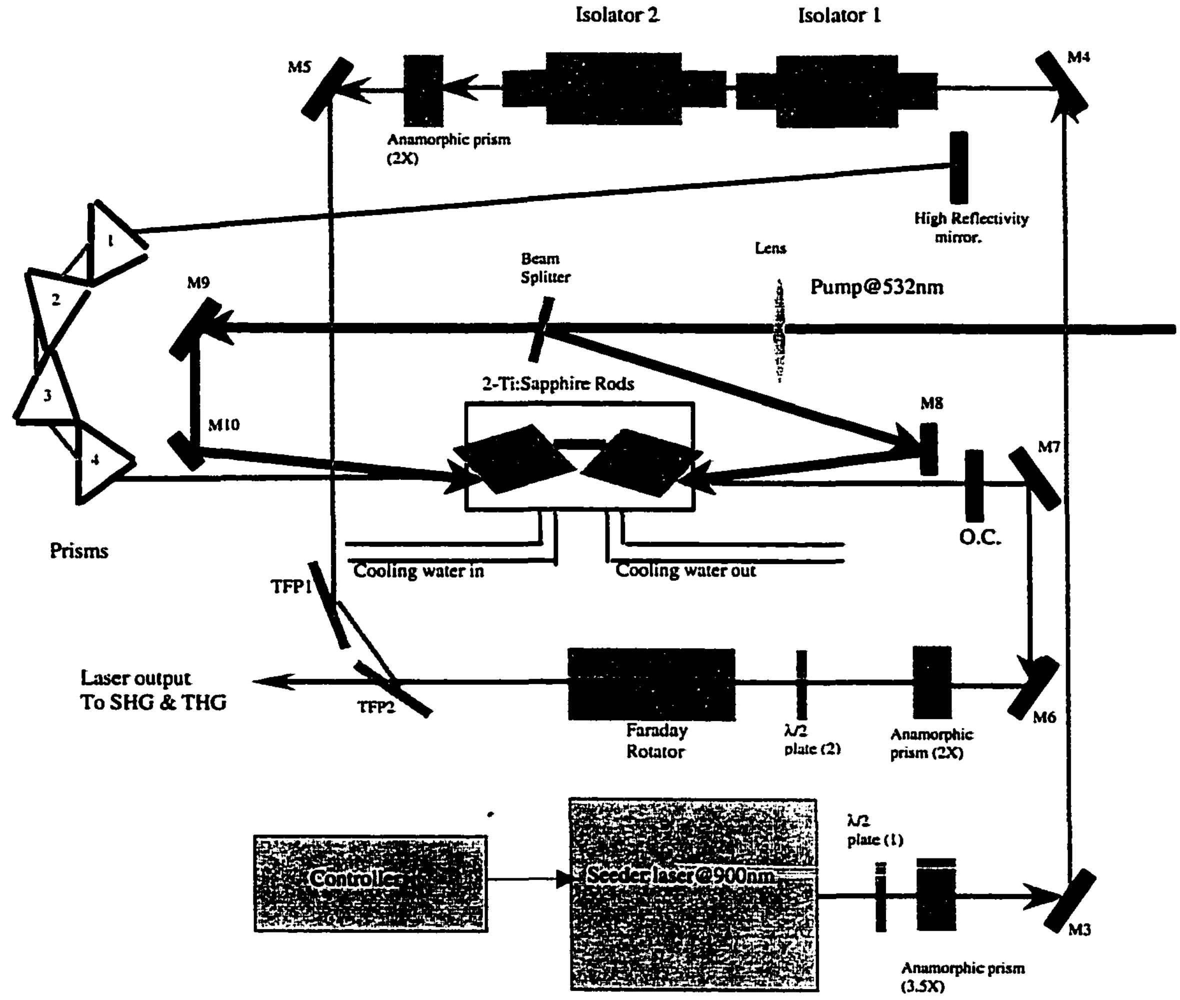

Fig. 4.4. Ti:sapphire laser layout with injection seeding.

The polarization of the Ti:Sapphire laser (propagating away from the output coupler) was rotated 45 degrees by the Faraday rotator, thus the half wave plate (2) is used to restore the original horizontal polarization orientation. The horizontally polarized laser beam is mostly transmitted through the thin film polarizer, TFP2, set at Brewster angle. This output is directed to the third harmonic generation setup.

4.4. Second and third harmonic generation setup

The third harmonic generation setup, shown in Fig. 4.5, employed two Lithium Triborate (LBO) nonlinear crystals (5×5×20 mm^3) because of LBO's good non-linearity, large acceptance bandwidth, and high optical damage threshold [4-6]. Type I phase matching (o-o-e matching) was selected for both LBO crystals. The first LBO crystal, for second harmonic generation (SHG), was cut at theta of 90° and phi of 23° ($\theta = 90°$ $\phi = 23°$) and coated with a double-V antireflection coating (AR) at both wavelengths of 900 and 450 nm or 867 and 433.5 nm on the input and output surfaces. The horizontally polarized fundamental laser beam at 900 or 867 nm from the Ti:Sapphire laser was directed into the LBO crystals and the vertically polarized second harmonic was generated by the first LBO crystal. To match the Type I setup of the second LBO crystal, a dual wavelength waveplate, half-wave for 450 nm and full-wave for 900 nm, with double-V AR coatings at 900 and 450 nm was used to rotate the polarization of the second harmonic from horizontal to vertical without changing the polarization of the fundamental. Behind the dual wavelength waveplate, the second LBO crystal was used for sum frequency generation (SFG), and was cut at theta of 90° and phi of 55° ($\theta = 90°$ $\phi = 55°$) and coated with a double-V AR coating at wavelengths of 900 and 450 nm or 867 and 433.5 nm on the input surface and AR coatings at the wavelength 300 or 289 nm on the output surface.

Following the first LBO crystal and the dual wavelength waveplate, the horizontally polarized second harmonic and the residue of the fundamental wave were directed into the second LBO crystal to generate the third harmonic by summing the frequencies. The three laser beams, generated third harmonic at either 300 or 289 nm, residuals of the fundamental at 900 or 867 nm, and the second harmonic at 450 or 433.5 nm, were spatially separated by a fused silica Pellin Broca prism (PB). The two LBO crystals used in this configuration were not temperature or pressure regulated.

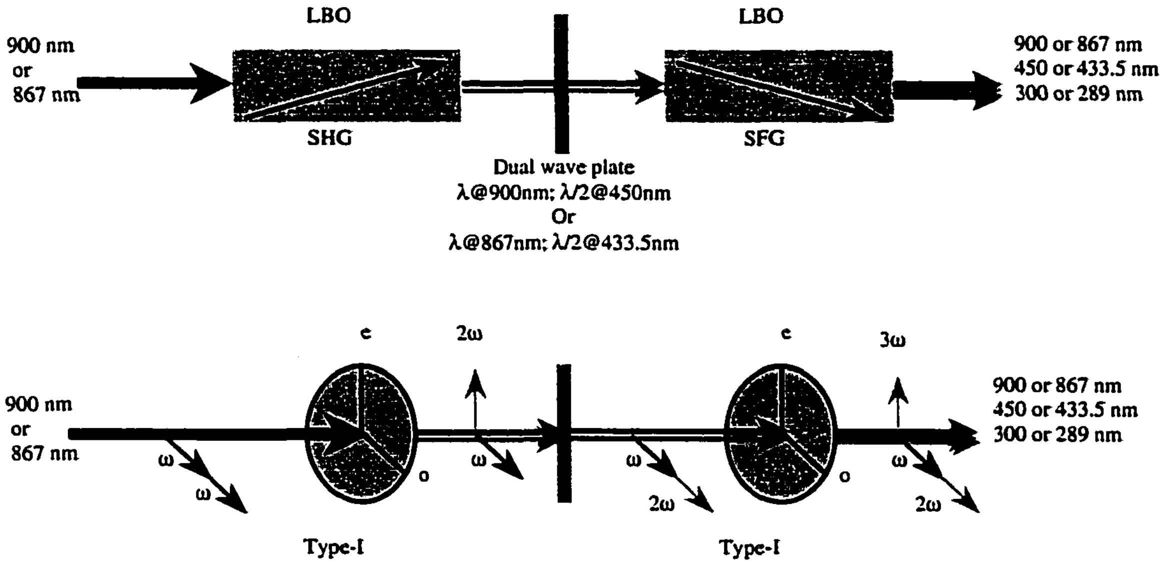

Fig. 4.5. Third harmonic generation setup using two LBO crystals resulting in an output at either 300 or 289 nm.

References:

1. N.Barn, and James C. Barnes "Injection seeding I: Theory," *IEEE Journal of Quantum Eelec*, Vol. 29, No., 10, 1993.
2. F. Salin, J. Squier, "Gain guiding in solid-state lasers," *Opt. Lett.* 17, 1352(1992).
3. F. Salin, F. Estable, E. Mottay, and L. Brunel, "High-Power, Gain Guided Ti:AL_2O_3 Laser: Theory and Experiment," in *OSA proceedings on advanced solid-state lasers*, Albert A. Pinto and Tso Yee Fan, (eds.), (New Orleans, Louisiana, February 1-3, 1993), p294.
4. Mikhnyuk, and I. G. Tarazevick, "LiB_3O_5, a higly efficient frequency converted for Ti:sapphire lasers," *Opt. Lett.* Vol 16, pp. 1726-1728, 1991.
5. S. Lin, Z. Sun, B. Wu, and Chen, "The nonlinear optical characteristics of LiB_3O_5 Crystal," *J. Appl Phys.*, vol67, pp. 634-638, 1990.
6. S. P. Velsko, M. Webb, L. Davis, and C. Huang, "Phase-matched harmonics generation in lithium triborate (LBO)," *IEEE J. Quantum Electron.* Vol. 27, pp. 2182-2192, 1991.

Appendix A:

Figures AIV-1 and AIV-2 are pictures of the Ti:sapphire laser system. Arrows show the paths of the 532-nm pump beam and the Ti:sapphire laser beam.

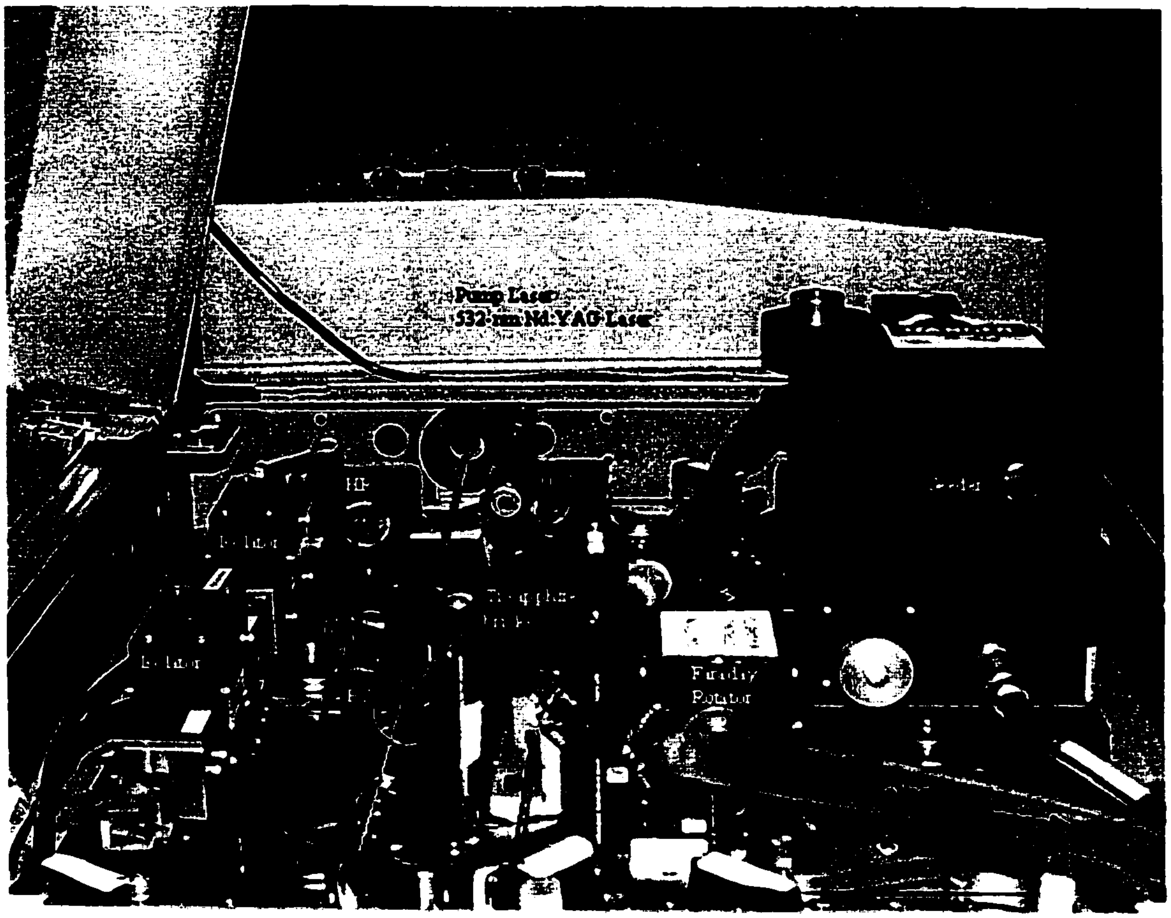

Fig. AIV-1 Ti:sapphire laser system with the 532-nm Nd:YAG pump laser

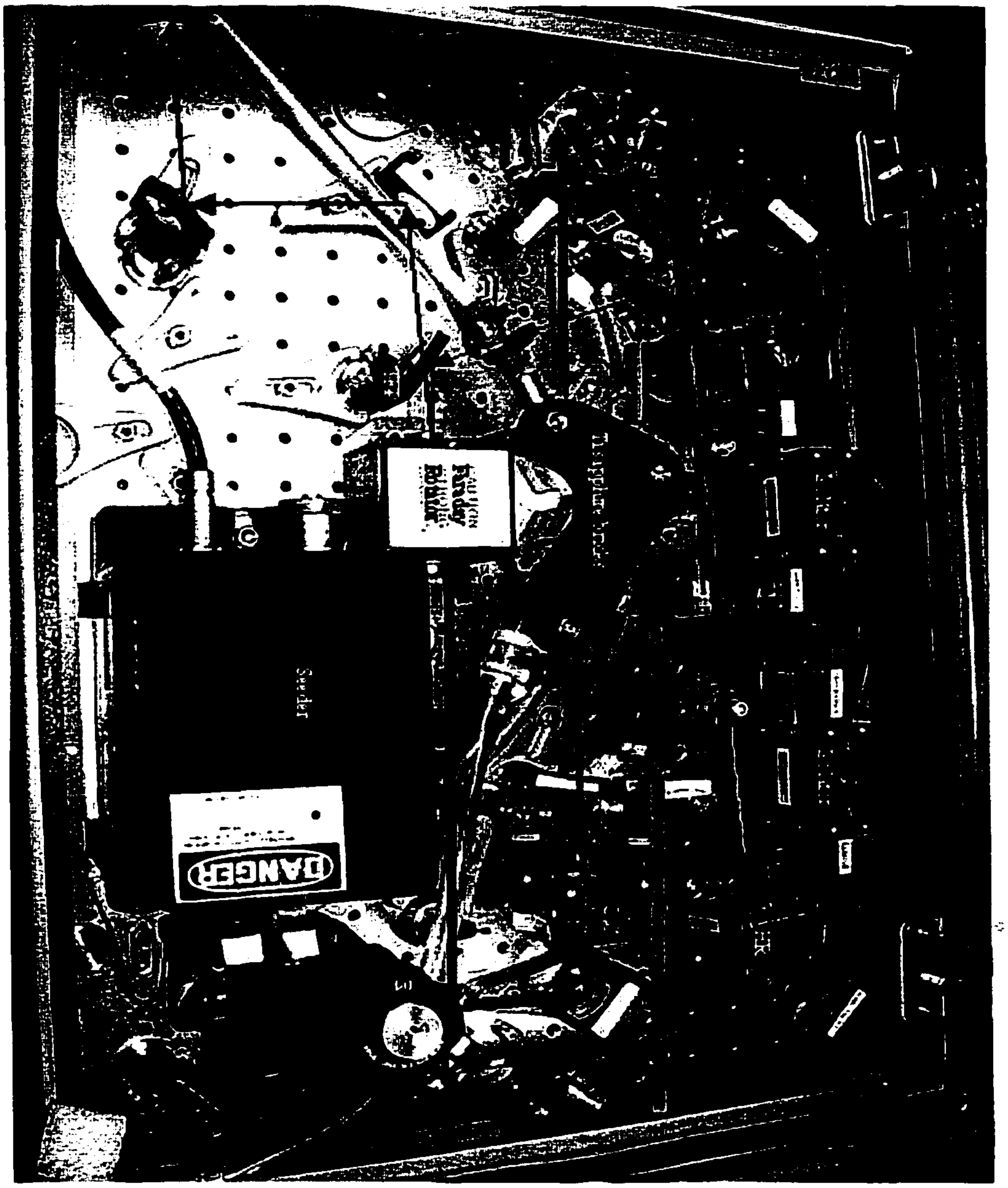

Fig. AIV-2 Complete Ti:sapphire laser system. The pump beam enter from the right and the Ti:sapphire beam exits to the left. The harmonic generation crystals are not shown.

Optical Components used in 867 and 900-nm Ti:sapphire laser systems:

Name in Fig. 1 of Ch IV	Component & Function	Part Number	Vendor
M1-M15	High reflectivity mirrors @ 860-900 nm @ 45 ° P Pol	Mirror 25.4×9.525 MM F/s or HR-W1-2509B-900-45	VLOC Laser optics or Lambda Research
Seeder laser	CW Laser Diode (EOSI)2010 Laser @ 867 or 900 nm	LCU2010	Environmental Optical sensors Inc
$\lambda/2$ plate (1)	½ waveplate at 867 or 900 nm	WP-25CQ-M2-867 WP-25CQ-M2-900	Lambda Research
Isolator (1)	Optical isolator	BB9-5I	Electro-Optics Technology, Inc.
Isolator (2)	Optical isolator	BB9-5I	Electro-Optics Technology, Inc.
(2)Anamorphic prism (3.5X)	Anamorphic prism	ANP-15 SF10	Lambda Research
(3)Anamorphic prism (2X)	Anamorphic prism	ANP-15 SF10	Lambda Research
(4)Anamorphic prism (2X)	Anamorphic prism	ANP-15 SF10	Lambda Research
High Reflectivity mirror	High Reflectivity mirror @ 867 or 900 nm, 0 degree	TLM1-867-0-1037 TLM1-900-0-1037	Lambda Research
lens	Plano-convex lens, AR coated at 532 nm	PLCX-25.4-309.1-UV	CVI Laser Inc.
Beam Splitter	50/50 beam splitter, AR @ 532 nm	HPR-2603U-50R-532	Lambda Research
Prisms 1,4	Bk7, Dispersion prisms	Triangle prism-15B	Lambda Research
Prisms 2,3	Fused Silica Dispersion prisms	Triangle prism-15B	Lambda Research
Output coupler	Output Coupler, R=40% @900nm or 35% @867nm	PRI-900-40-1037 PRI-867-35-1037	Lambda Research
TFP1, TFP2	Thin Film Polarizer, AR @ 867 or 900 nm	TFP-923PW-1025-UV TFP-870PW-1025-UV	Lambda Research
Ti:sapphire Rods	Ti:sapphire laser rods cut at Brewster angle	custom	Crystal Systems
SHG	Nonlinear LBO SHG crystal, see text for details	custom	CASIX
SFG	Nonlinear LBO, THG crystal, see text for details	custom	CASIX
Dual waveplate	Dual Waveplate, λ @867 and $\lambda/2$ @433.5 or λ@900nm and $\lambda/2$ @ 450 nm.	WP-25CQ-2/450-1/900 WP-25CQ-2/433.5-1/867	Lambda Research

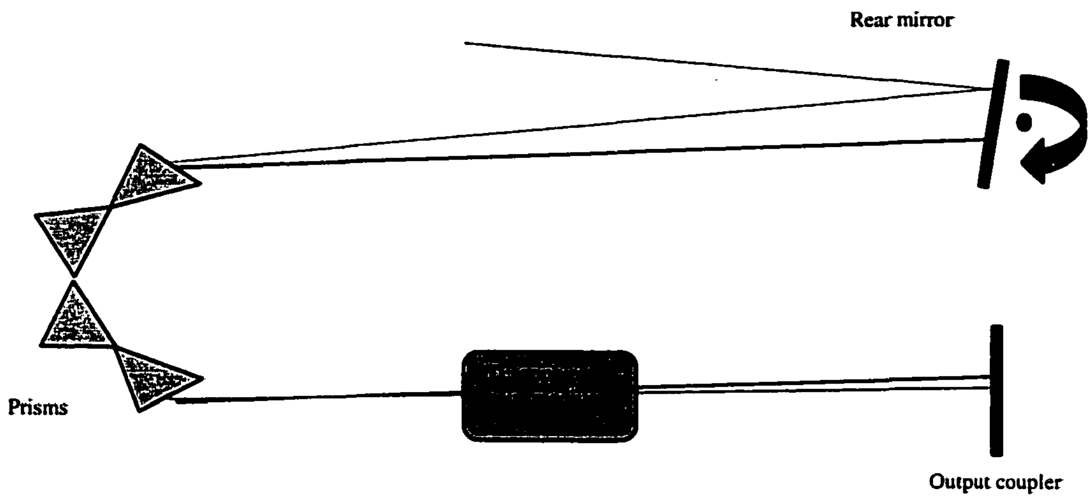

Fig. A2. Tuning of Ti:sapphire laser.

The prisms inserted in the cavity are at Brewster angle to minimize reflection losses since the laser in the cavity is p-polarized. The prism is designed to have both the incident beam and the emerging beam at Brewster angle; thus at the wavelength of design, the refracted beam is parallel to the prism base.

Dispersion formula:

The prism is inserted in the cavity at Brewster angle to minimize reflection losses. This prism is designed to have both the incident beam and the emerging beam at Brewster angles; thus at the wavelength of design, the refracted beam is parallel to the base of the prism.

For a dispersive Brewster prim we have,

$$\left\{\begin{array}{l}\theta_i = \theta_e = \theta_B \\ \theta_p = \theta_p^{*} \\ \tan\theta_B = \dfrac{n_p}{n_a} \\ \theta_p = \dfrac{\pi}{2} - \theta_B\end{array}\right\} \tag{B1}$$

The angular dispersion of a single prism is given by:

$$\frac{d\theta_i}{dn_p} = \frac{Sin\theta_p}{Cos\theta_B} + \frac{Cos\theta_p}{Cos\theta_{Bp}}\tan\theta_p \tag{B2}$$

using the relation of (1) we obtain

$$\frac{d\theta_i}{dn_p} = \frac{Sin(\pi/2-\theta_B)}{Cos\theta_B} + \frac{Cos\theta_p}{Cos\theta_B}\frac{Sin(\pi/2-\theta_B)}{Cos\theta_p} = \frac{Cos\theta_B}{Cos\theta_B} + \frac{Cos\theta_B}{Cos\theta_B} = 2 \tag{B3}$$

$$\frac{d\theta}{dn_p} = \frac{d\theta}{d\lambda}\frac{d\lambda}{dn_p} = 2 \tag{B4}$$

$$\frac{d\theta}{d\lambda} = 2.\frac{dn_p}{d\lambda} \tag{B5}$$

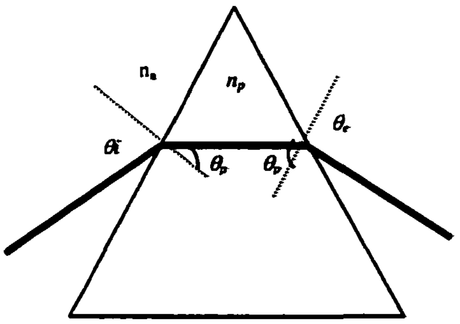

Fig. A3 Typical Brewster prism.

For a Brewster prism, the angular dispersion is equal to the abnormal dispersion of the prism material.

Dispersion of multiple prisms is given by

$$\frac{d\theta_r}{d\lambda} = r.\frac{d\theta_1}{d\lambda} \tag{B5}$$

where $\frac{d\theta_1}{d\lambda}$, is the dispersion of one prism, and r is the number of prisms.

To increase the angular dispersion in the laser cavity we introduced four prisms instead of one prism and turn the laser beam by 180° which makes the laser cavity more compact. Two of these four prisms made of fused silica and the other two prisms made of BK7 to ensure ~ 180° between the input and emerging beam. Then the equation B5 becomes

$$\frac{d\theta_r}{d\lambda} = 2.\frac{d\theta_{FS}}{d\lambda} + 2.\frac{d\theta_{BK7}}{d\lambda} \tag{B6}$$

CHAPTER V

TI:SAPPHIRE LASER EXPERIMENTAL RESULTS

In this chapter, we discuss the characteristics of the Ti:sapphire laser such as output energy, slope efficiency, linewidth, pulse width, and beam quality. The laser output wavelength is either 867 or 900 nm. This output will be harmonically converted to UV wavelengths as discussed in chapter VI.

1. Laser energy and slope efficiency

Two separate laser systems were built and configured, as shown in Fig. 4.1. The outputs of the two systems, though both horizontally polarized, differ in wavelength, one being at 867nm, the other at 900nm. Alignment of the Ti:sapphire laser cavity was achieved using the seeder beam to assure spatial mode matching between the Ti:sapphire and the 532-nm pump laser beams. This was achieved by spatially overlapping the seeder beam with the 532-nm pump beam. Fine adjustment of the alignment was accomplished using stepper-motor controlled mirrors. This was a one-time alignment procedure and need not be repeated upon every laser operation unless optical component changes take place in the laser cavity.

The average power output of both the Ti:sapphire and 532-nm pump laser were measured using a broadband power meter (Ophir, Model number 30A-HE-106). The pump laser energy was measured by setting up the power meter just before the thin lens shown in Fig. 4.1, while the power of the Ti:sapphire laser was measured after the thin film polarizer (TFP). The Ti:sapphire output energy was controlled by adjusting the pump laser energy.

The typical pulse energy output of the injection-seeded Ti:sapphire laser was in the range of 100-120 mJ. Figures 5.1 and 5.2 show the measured output pulse energy of the 30 Hz, injection-seeded, Ti:sapphire lasers either at 867 nm or 900 nm, as a function of the pump energy at 532 nm. The injection seeded slope efficiency of the laser at 867 nm was 40% with a threshold of 126 mJ while the slope efficiency at 900 nm was 32% with a threshold of 156 mJ. The maximum output pulse energy was 115 mJ with an optical energy conversion of about 30% from 532 to 867 nm. At 900 nm, the maximum output pulse energy was 105 mJ, with optical energy conversion of about 22% from 532-

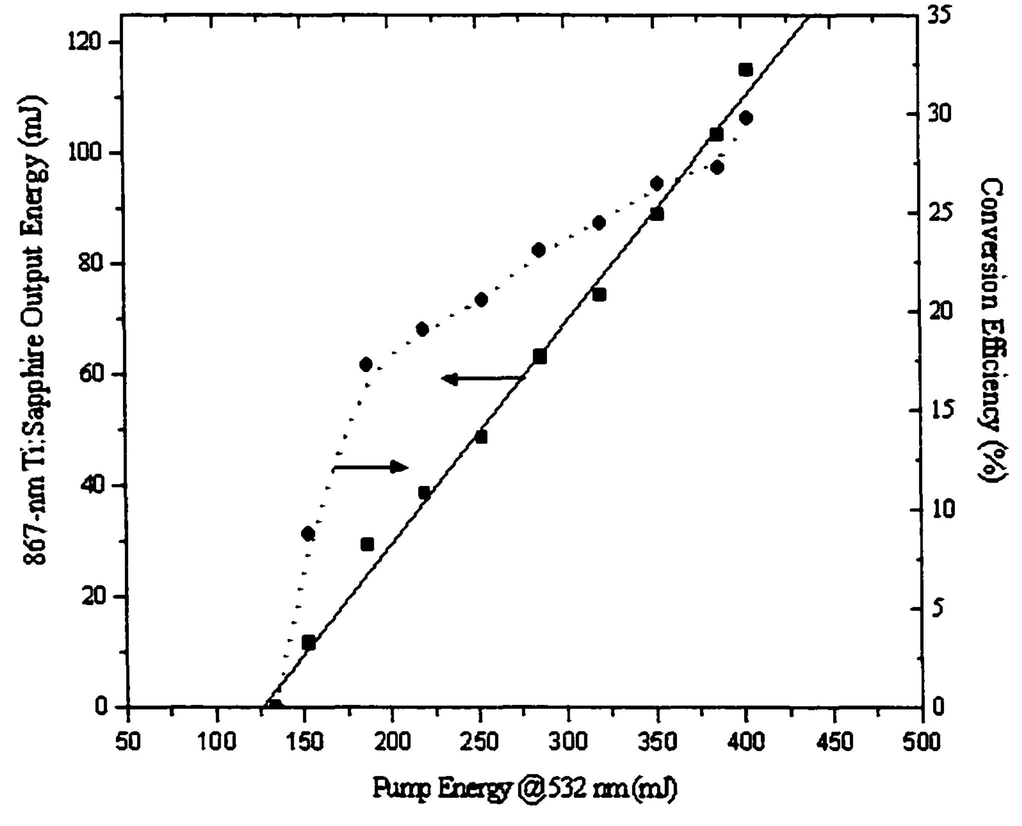

Fig. 5.1 Output pulse energy and efficiency of the 867 nm Ti:sapphire laser as a function of the 532-nm input pulse energy pump laser at 30 Hz.

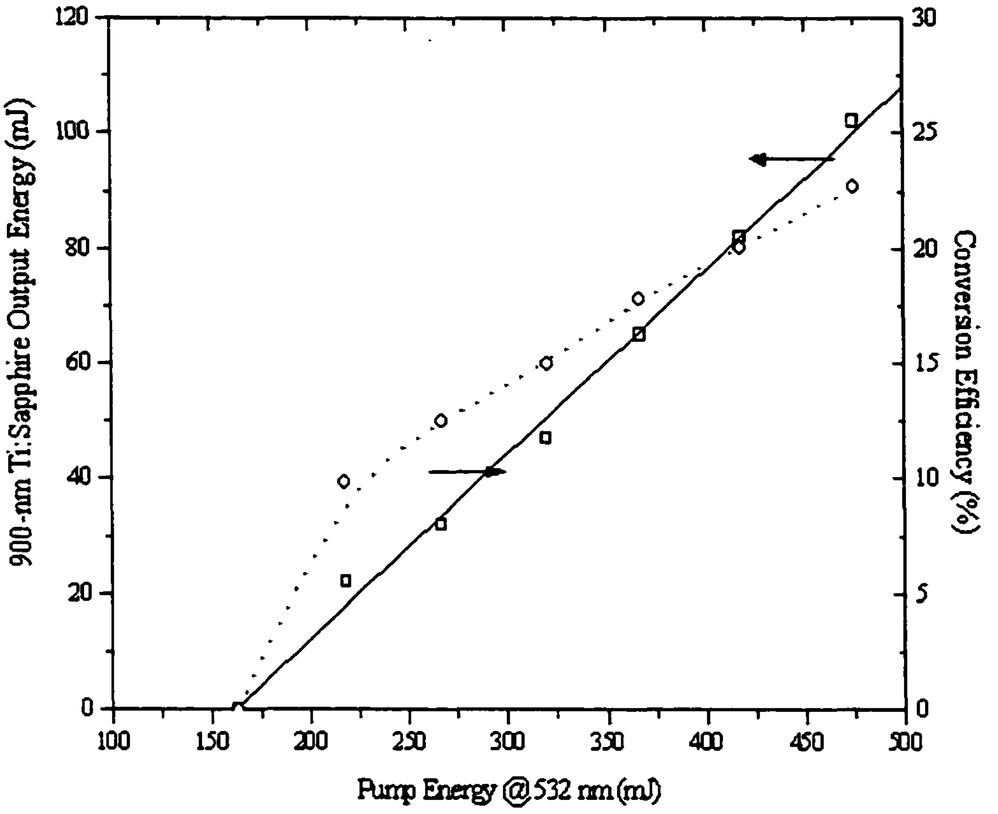

Fig. 5.2 Output pulse energy and efficiency of the 900 nm Ti:sapphire laser as a function of the 532-nm input pulse energy pump laser at 30 Hz.

nm to 900 nm. The output pulse energy of Ti:sapphire laser was limited by the 532-nm pump energy where the maximum energy available was 475 mJ.

2. Heating effect in Ti:sapphire laser brick

It was noted that the repetition rate of the pump beam had an effect on the output laser energy. As the repetition rate of the pump beam was increased from 20 Hz (no cooling) to 30 Hz (cooling), as shown in Fig. 5.3, the output of the Ti:sapphire laser decreased by ~ 10 % due to thermal effects resulting from energy deposition inside the laser brick. These effects include thermal lensing and a decrease in the upper laser level lifetime. The upper laser level lifetime decreases with increasing brick temperature due to phonon absorption to a higher level, which in turn decreases the stored energy in the upper laser state and hence decreases the output energy of the Ti:sapphire laser, as shown in Fig. 5.4. The represented temperature in Fig. 5.4 is measured on the Ti:sapphire brick mount and does not present the actual centerline temperature of the bricks, the actual temperature will be higher at the center of the bricks. This effect will be discussed in detail in Chapter

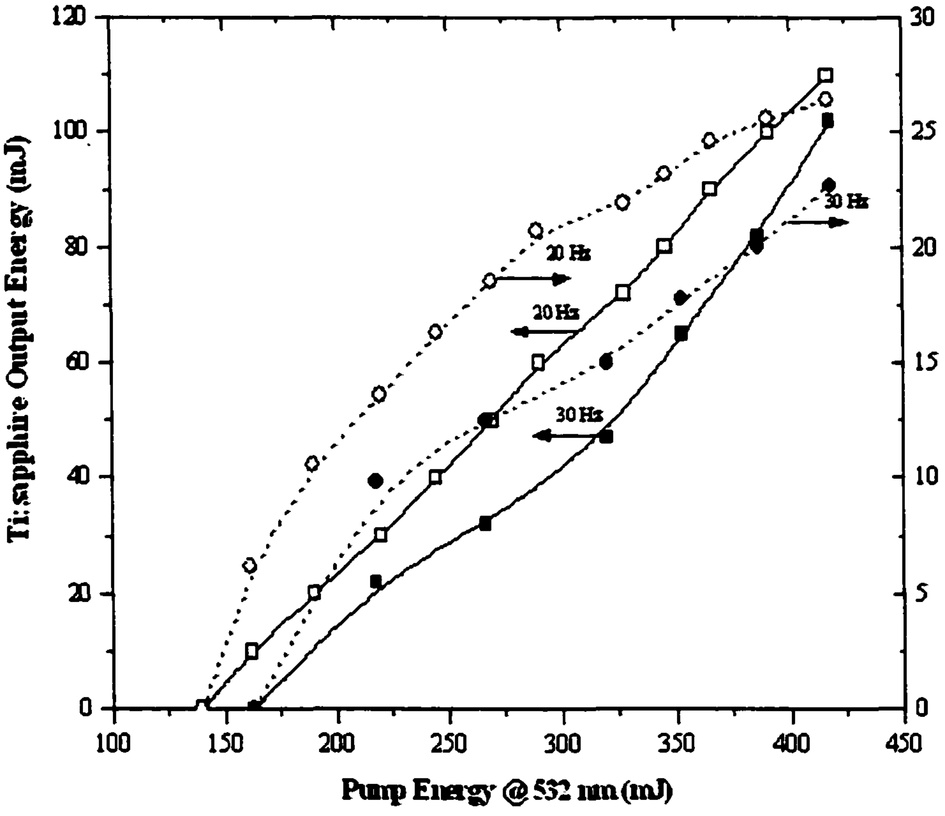

Fig. 5.3 Output pulse energy of the 900 nm Ti:sapphire laser as a function of the input pulse energy of the 532 nm pump laser at 20 and 30 Hz.

VII. To minimize these effects when operating at 30 Hz, the Ti:sapphire bricks were cooled by 20 °C flowing water. Without the water-cooling system, the brick mount could reach temperatures as high as 60°C when the Ti:sapphire lasers operated at a repetition rate of 30 Hz and pump pulse energy of 475 mJ. Insufficient cooling results in clearly observable gain reduction of the Ti:sapphire crystal and prevents high-energy pulse output from being obtained.

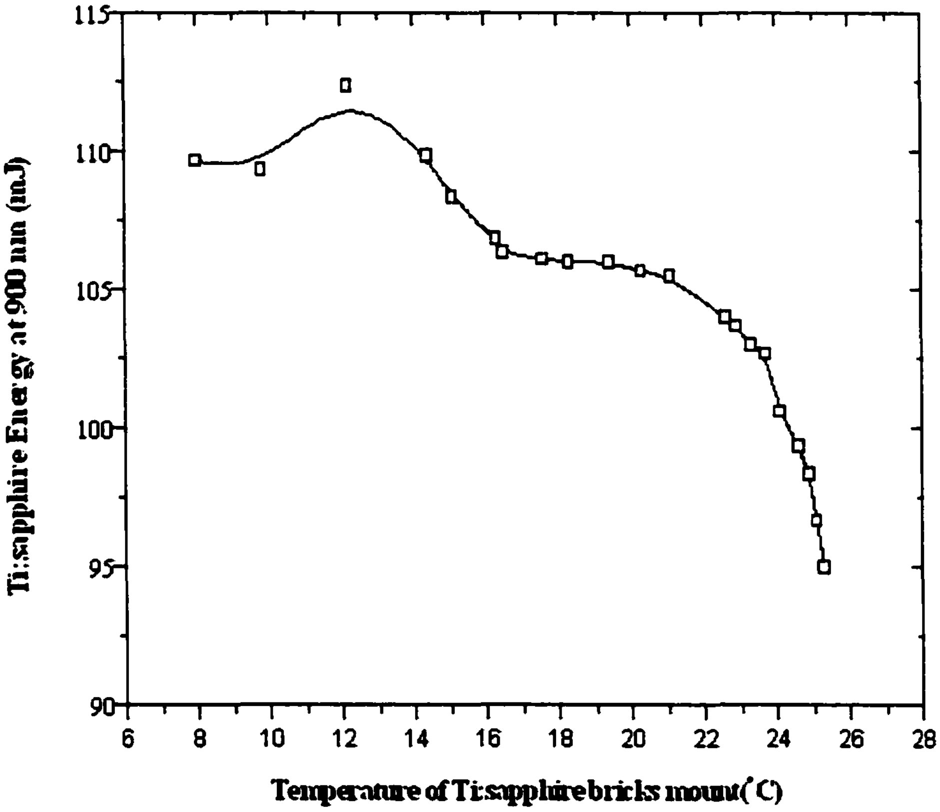

Fig. 5.4 900-nm Ti:sapphire laser energy at 30 Hz as a function of laser crystal temperature.

3. Pulsewidth and temporal measurements

As will be discussed later in Chapter VIII, the pulsewidth and temporal profile of the Ti:sapphire laser are important for harmonic generation processes so we recorded the temporal profile of the output pulses at both 867 and 900 nm wavelengths. The resulting laser fluorescence was detected by a high-speed photodiode detector, which has a spectral range of 200–1100 nm for broadband emission measurements (Thorlabs DET200, rise time < 1 ns); then, the photodiode signal was processed by a fast oscilloscope.

The measured pulsewidth of the 532-nm pump beam was ~ 8 ns (FWHM) while the measured output pulse widths of the Ti:sapphire lasers at 867 nm or 900 nm (30 Hz) were about 25 ns (FWHM) for both the seeded and unseeded case. Temporal profiles of the laser system while seeded and unseeded are shown in Fig. 5.5. For the injection-seeded case, there were usually at least two longitudinal modes oscillating and the mode-beating features of the two closely spaced cavity modes was obvious, as shown in Fig. 5.5, and the measured beat period was ~ 9.3 ns corresponding to ~ 107 MHz spacing of the pulsed cavity modes ($c/2l$, where c is the speed of light and l is the cavity length). The laser cavity temperature and vibration cause these cavity modes to vary; thus when the frequency of the seed beam lies between two oscillator cavity modes, the laser oscillator can operate on both cavity modes as the varying oscillator modes sweep through the seed laser frequency. Such dual mode output is useful, since the dual mode output power is higher than single mode operation thus leading to higher harmonic conversion [1], which allows higher UV output energy.

Noteworthy, in Fig. 5.5, is that the seeded cavity lases up to 7 ns before the unseeded cavity due to the presence of seed photons, rather than allowing laser action to start from intra-cavity noise. The buildup time (defined as the delay between the peak of the pump pulse and the peak of the Ti:sapphire pulse) for a 100 mJ unseeded Ti:sapphire laser pulse was ~ 95 ns while the buildup time for the 100 mJ seeded Ti:sapphire laser pulse was 89 ns.

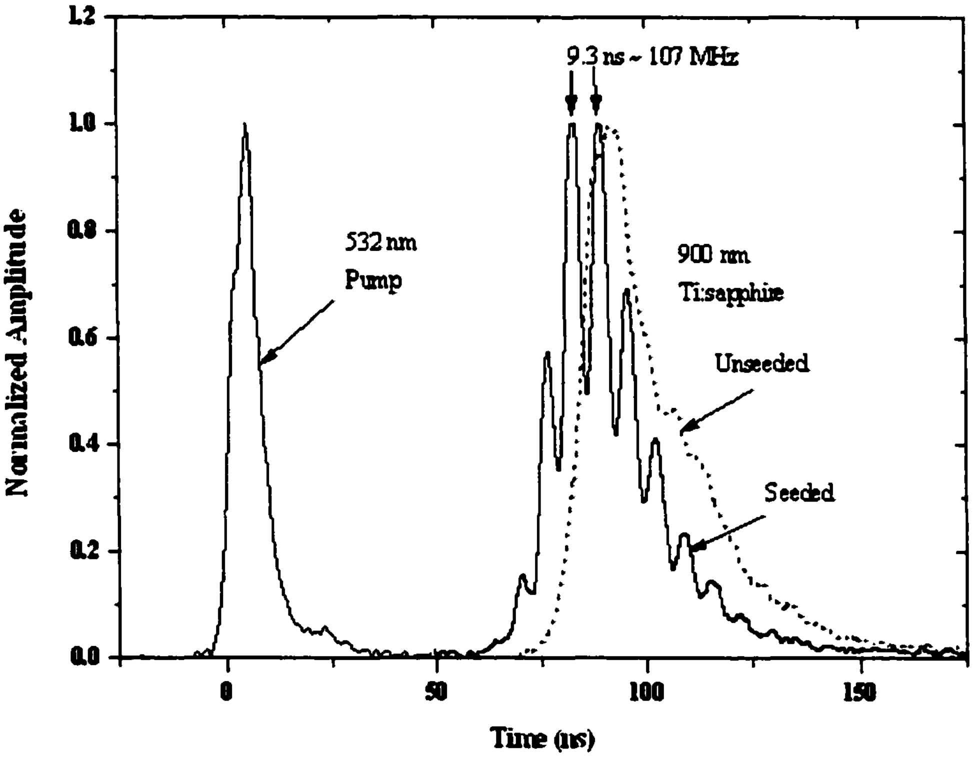

Fig. 5.5 Temporal profile of 532 nm pump pulse, seeded, and unseeded Ti:sapphire laser cavity at 900 nm at 400 mJ pump energy.

Since the pulsewidth of the Nd:YAG pump pulse was much shorter than the buildup time of the Ti:sapphire laser pulse, the Ti:sapphire laser pulse takes the form of a single gain-switched pulse. The pulse buildup time and the pulse width of the Ti:sapphire oscillator at 30 Hz were measured and plotted as a function of the pulse energy of the laser at the fundamental wavelength of 900 nm as shown in Fig. 5.6. The buildup time was defined as the delay between the peak of the pump pulse and the peak of the Ti:sapphire pulse. As is shown in the figure, the pulse width of the Ti:sapphire oscillator decreases as the pulse energy increases. The buildup time follows the same behavior as the pulse width. Both pulse width and buildup time approach asymptotic values as the pump power is increased. The buildup time depends on the ratio of the pump pulse energy to the threshold pulse energy. Injection seeding reduces the buildup time of the oscillator significantly as shown earlier in Fig. 5.5.

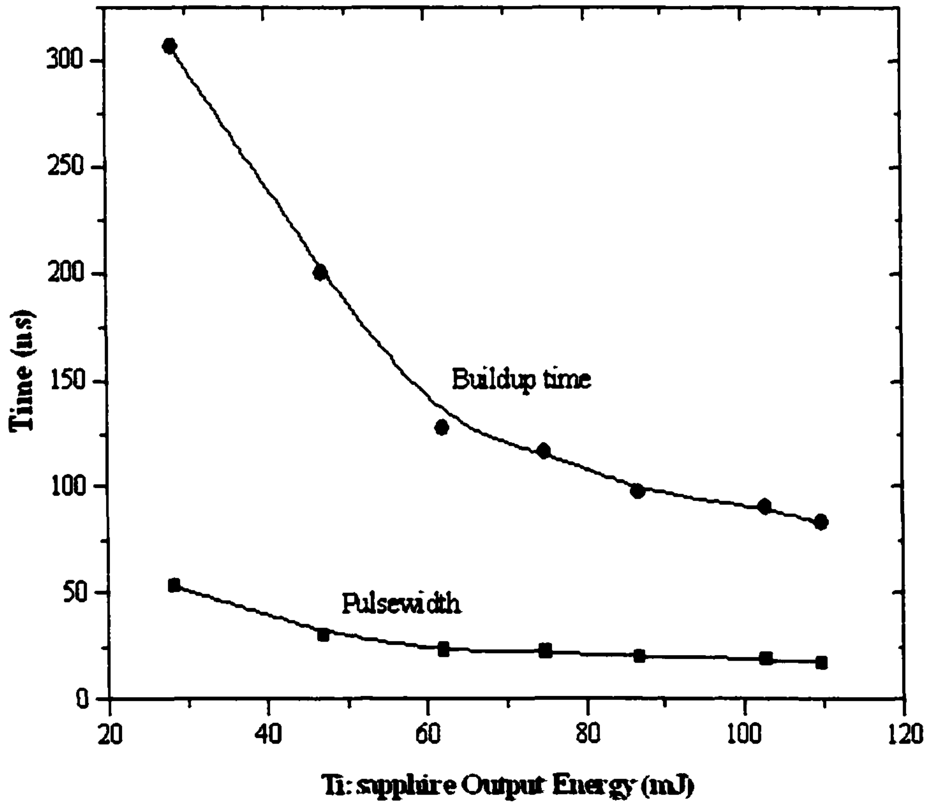

Fig. 5.6 30 Hz unseeded Ti:sapphire laser output pulse duration (FWHM) and build up time at 900 nm as a function of Ti:sapphire energy.

4. Temporal and amplitude stability of the output pulses

A significant property of the injection-seeded laser is the temporal stability of the output pulses [2]. The temporal stability of the pulses is most apparent in the low temporal jitter relative to the pump pulse as shown in Fig. 5.7, where the jitter is simply the variation in the buildup time. Jitter refers to time variation that cannot be corrected with alignment or tuning of the laser cavity.

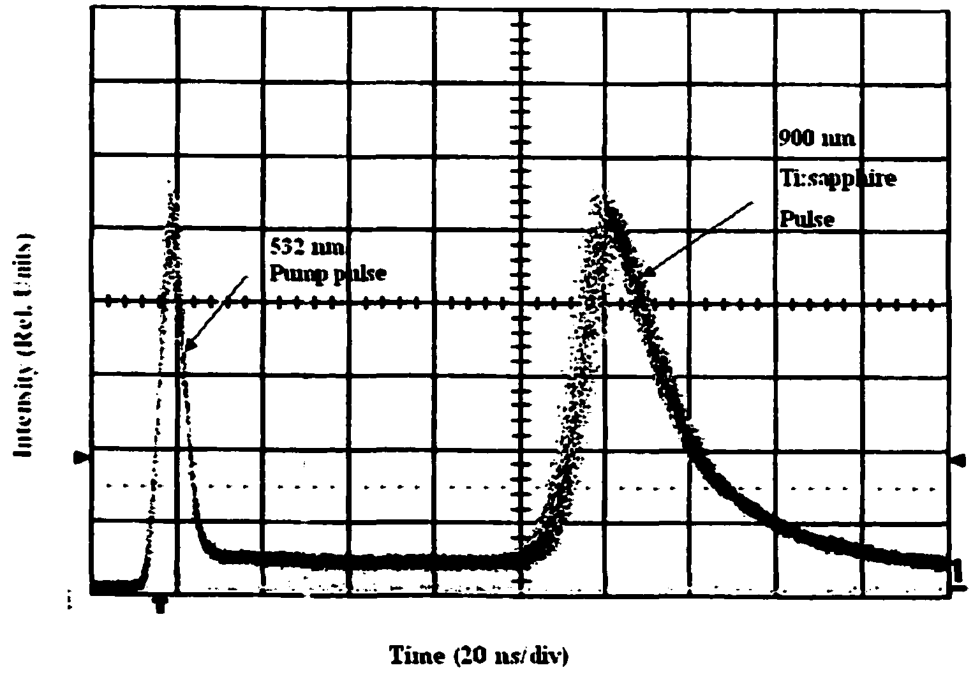

Fig. 5.7 Temporal and amplitude stability of the output pulses. The oscilloscope trace is a collection of 600 unseeded laser shots. The time scale is 20 ns/division.

Likewise, the variation in the pulse amplitude was ~ 2 %, which was due to the 532 nm pump laser. This can be seen from the amplitude jitter seen in Fig. 5.7. Jitter was less in seeded laser.

5. Linewidth and bandwidth of the Ti:Sapphire laser

As was mentioned earlier in Chapter III, injection seeding is essential to achieving high third harmonic conversion efficiency. A computer controlled pulsed wavemeter (Burleigh WA 4500) was used to measure the linewidth of the seeder and Ti:sapphire laser for seeded and unseeded cases. An optical wedge was used to direct a small portion of the beam into the wavemeter then the linewidth was measured. Without injection seeding the linewidth of the Ti:sapphire laser system was about 400 pm. This linewidth was not narrow enough to achieve efficient third harmonic generation. After using the injection seeding technique the linewidth was reduced to less than 3.5 pm (limited by the resolution of the wavemeter which was 3.5 pm), which is more than adequate to perform the ozone DIAL measurements and allow good third harmonic generation. To obtain an estimate of how well seeded the oscillator was, the spectral profiles of the laser diode seeder, the unseeded and the seeded Ti:sapphire cavity have been recorded and are shown in Fig 5.8. The beam is detected by a spectrometer followed by an optical multichannel analyzer (OMA) providing background correction. Without any seeding, the spectrum of the oscillator had a broadband character centered at 900 nm. In the presence of 900 nm seeding, it exhibited a much narrower lineshape, similar to the diode laser itself (0.01 pm).

The efficiency of the seeding depends on the power of the seeder diode coupled into the Ti:sapphire oscillator cavity. About 1.75 mW was coupled into the laser cavity, which was adequate for good seeding while a minimum of 0.75 mW of injection power was necessary to achieve injection seeding.

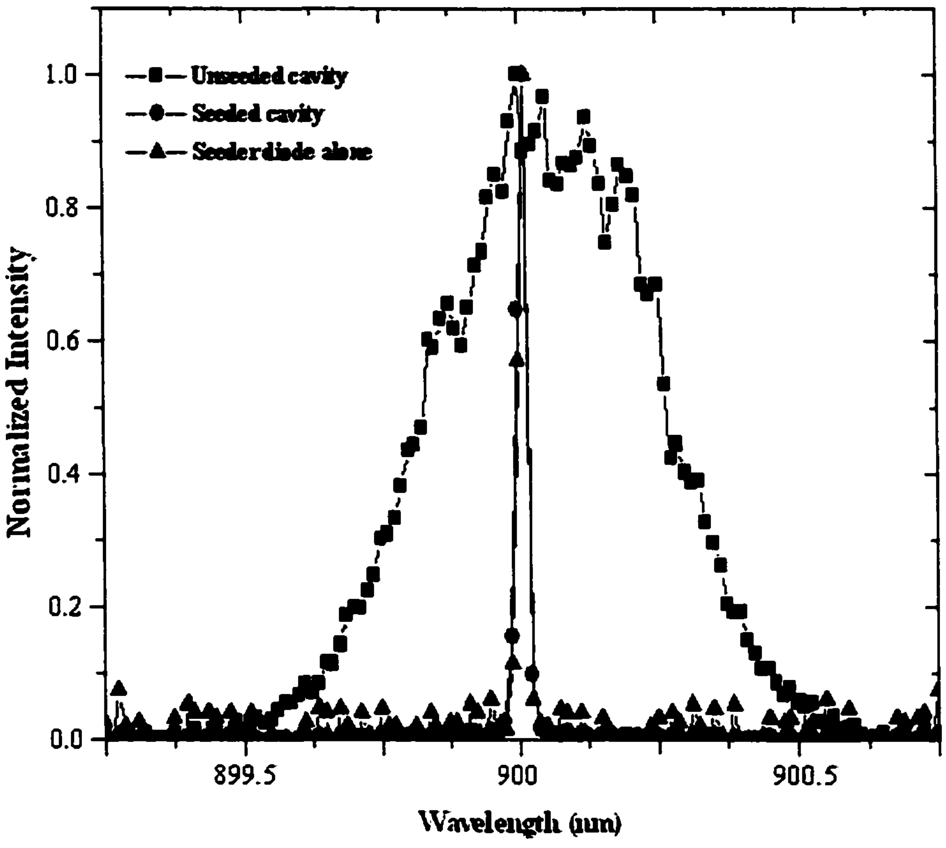

Fig. 5.8 Wavelength spectra of the Ti:sapphire laser cavity with and without injection seeding. Also shown is the seeder diode laser spectrum alone.

6. Laser beam quality and divergence

The spatial beam profiles of the pump, seeder, and Ti:sapphire laser beams were monitored and the beam diameters were measured using a two-dimensional array CCD (charged-coupled devices) detector and Beamview Analyzer. An optical wedge was used to direct 3% of the beam to a variable optical attenuator to bring the incident power below the damage and saturation level of the detector. The beam then was directed to a CCD camera (Cohu 4800), where the output was digitized and displayed on a computer using a Coherent BeamView Analyzer (Coherent, version 2.2.1). The near field profiles of the 532-nm pump, the 900-nm seeder laser, and the 900-nm unseeded and seeded Ti:sapphier laser beams are shown in Figs. 5.9, 5.10, 5.11, and 5.12 respectively. The pump beam was 9.5 mm ($1/e^2$) in diameter. The pump beam spatial profile was nearly a flat top with a hot spot in the geometrical center of the beam as shown in Fig. 5.9. In order to not produce laser damage, the pump laser was not focused on the Ti:sapphire brick surface, but about 3.5 mm on the brick's surface. Fig. 5.10 shows the near field spatial profile of the diode seeder laser at 900-nm wavelength. The beam profile was elliptic with diameters ($1/e^2$) of 1.8 and 2.2-mm in x and y-axis respectively. The spatial beam profile of the unseeded and seeded Ti:sapphire laser in the near field was Gaussian with a diameter of 1.8 mm ($1/e^2$) as shown in Figs. 5.11 and 5.12 respectively. The profile was taken at 100 mJ output energy. The output beam shape was always near Gaussian and did not follow the spatial gain shape of the 532-pump beam, shown in Fig. 5.9. This was due to diffraction in the laser cavity, which smoothes the gain profile. This is explained by the fact that high order transverse modes in the laser beam diffract more quickly than lower transverse modes and thus after a few passes in the cavity they do not enter the gain medium in the pumped region [3]. The gain profile acts as a mode filter, which leads to higher gain for low order transverse modes and thus smoothes the beam profile. Also, the long laser cavity lets the high order transverse modes diffract out of the pumped region leading, also, to a smooth laser beam profile. This Gaussian profile beam was well suited to provide efficient second and third harmonic generation processes which favor Gaussian profile beams. The spatial profile of the 867 nm laser beam (not shown) was similar to the 900 nm laser beam.

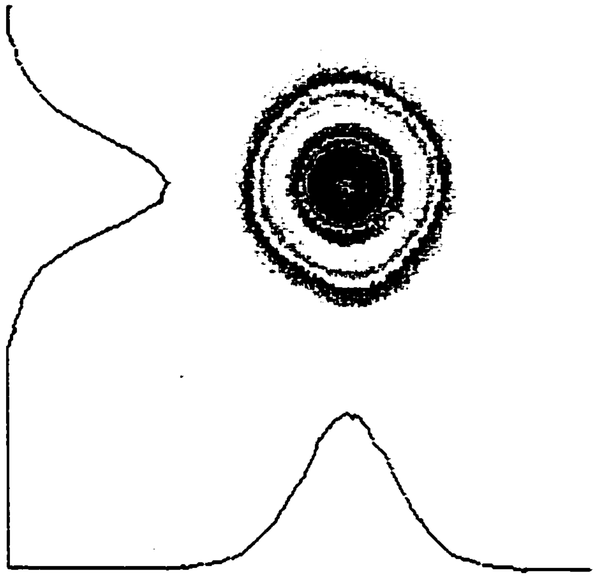

Fig. 5.11 Near field spatial profile of 900-nm unseeded Ti:sapphire laser. This picture is taken at 110 mJ output energy (30 Hz). The 1/e^2 diameter is 1.8 mm.

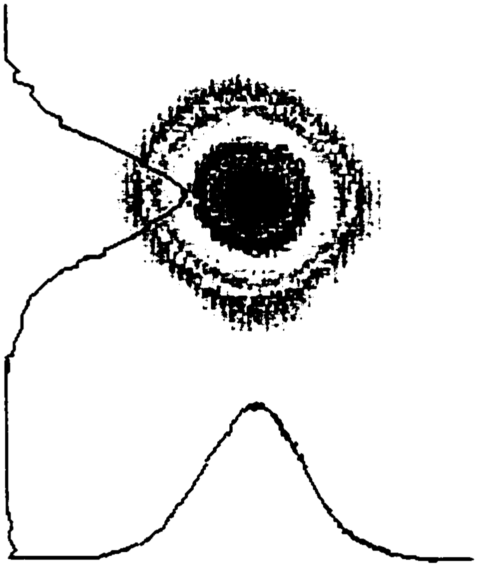

Fig. 5.12 Near field spatial profile of the 900-nm seeded Ti:sapphire laser. This picture is taken at 100 mJ output energy (30 Hz). The 1/e^2 diameter is 1.8 mm.

A convex lens of 100 cm focal length was used to determine the beam divergence and beam quality of a 100 mJ output laser beam using a Coherent Beamview Analyzer (version 2.2.1) and CCD camera (Cohu 4800). The $1/e^2$ beam diameter was measured at different locations as shown in Fig. 5.13, then the minimum beam waist was located from Fig. 5.14. Knowing the far field beam diameter, at the minimum waist and the beam diameter of the near field beam (a beam diameter measured ~ 50 cm away from the output coupler), the beam quality can be calculated using Eq. 1 [4].

$$M^2 = \frac{\pi \omega \omega_o}{4\lambda f} \tag{1}$$

where ω and ω_o are the beam diameters with and without the lens respectively, λ is the laser wavelength (900 nm), and f is the focal length of the lens (100 cm). It was found that the laser beam was near diffraction limited with an $M^2 = 1.3$ (the ideal diffraction limited beam has $M^2 = 1$).

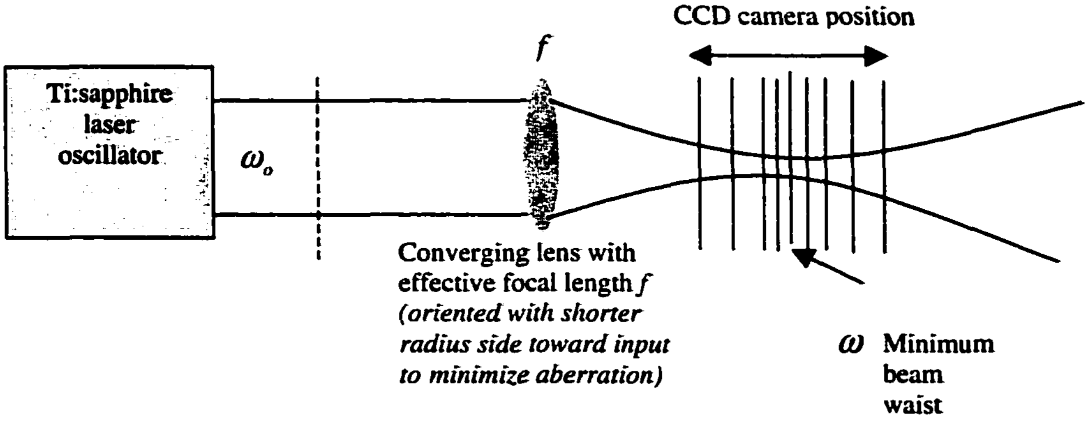

Fig. 5.13 Laser beam quality (M^2) experimental setup.

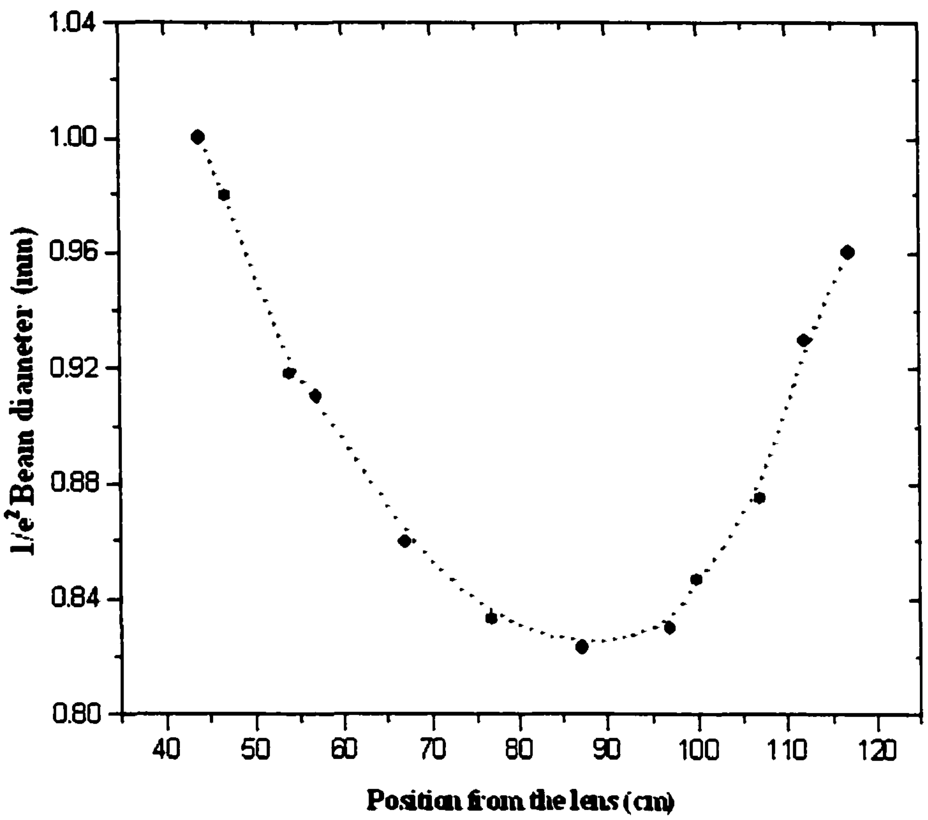

Fig. 5.14 The 900-nm laser (30 Hz) beam diameter ($1/e^2$) as a function of the position from the convex lens at 450 mJ pump energy.

The beam diameter at the focus was measured as shown in Fig. 5.15, then the 900-nm laser beam divergence was calculated using Eq. 2 [4].

$$\theta = \frac{\omega_f}{f} \qquad (2)$$

where ω_f is the beam diameter at the focus and f is the focal length of the lens (100 cm). It was found that the divergence of the Ti:sapphire laser beam was 0.8 mrad (full angle).

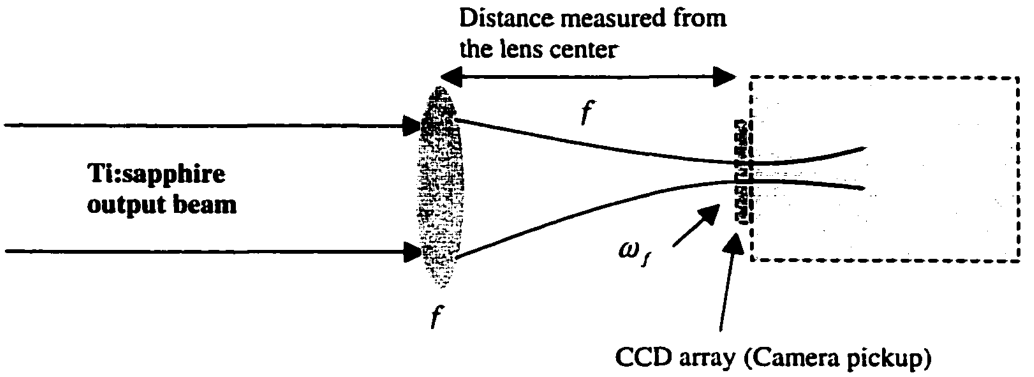

Fig. 5.15 Laser beam divergence experimental setup.

These measured quantities of beam quality and beam divergence are adequate to produce good harmonic conversion efficiency. As will be discussed in Chapter VIII, the second and third harmonic generation favor a diffraction limited laser beam ($M^2 = 1$) with a small divergence (< 0.8 mrad).

7. Thermal lensing measurements

There was concern about thermal lensing when operating the Ti:sapphire laser at 30-Hz repetition rate due to high heat loading in the Ti:sapphire bricks from the 532 nm pump laser. Those concerns motived interest in an experiment to measure the thermal lensing and the degree to which the energy deposited in laser bricks affects the performance of the Ti:sapphire laser due to thermal lensing.

A 1-m focal length lens was inserted inside the laser cavity after the intracavity prisms, and then the seeder beam (900-nm) was directed out of the cavity to the CCD camera by a periscope after it went through the bricks as shown in Fig. 5.16. The beam diameter was measured with the 532 nm pump beam off, by moving the camera back and forth to locate the smallest spot size. Then these measurements were repeated at different 532-nm pump energies. The idea was to monitor the change of the seeder beam diameter due to thermal loading in the bricks and then calculate the focal length of the resulting thermal lens. The focal length of the thermal lens was calculated at each pump energy using the general law of lenses.

$$\frac{1}{f_{th}} = \frac{1}{f_g} - \frac{1}{f_L} \qquad (3)$$

where f_{th}, f_L and f_g, are the focal length of the thermal lens, 100-cm lens, and group (thermal lens and 100-cm lens) respectively. As expected, the focal length of the thermal lens decreased with increasing pump energy, as shown in Fig. 5.17.

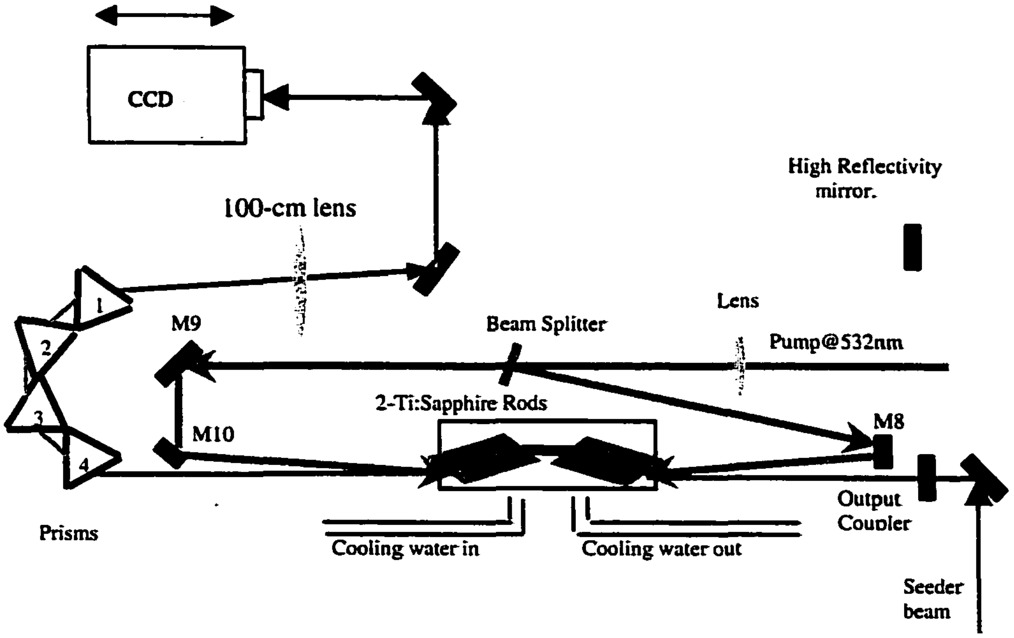

Fig. 5.16 Thermal lens measurement experimental setup. The CCD camera is moved to find the focal point due to thermal lens in Ti:sapphire bricks.

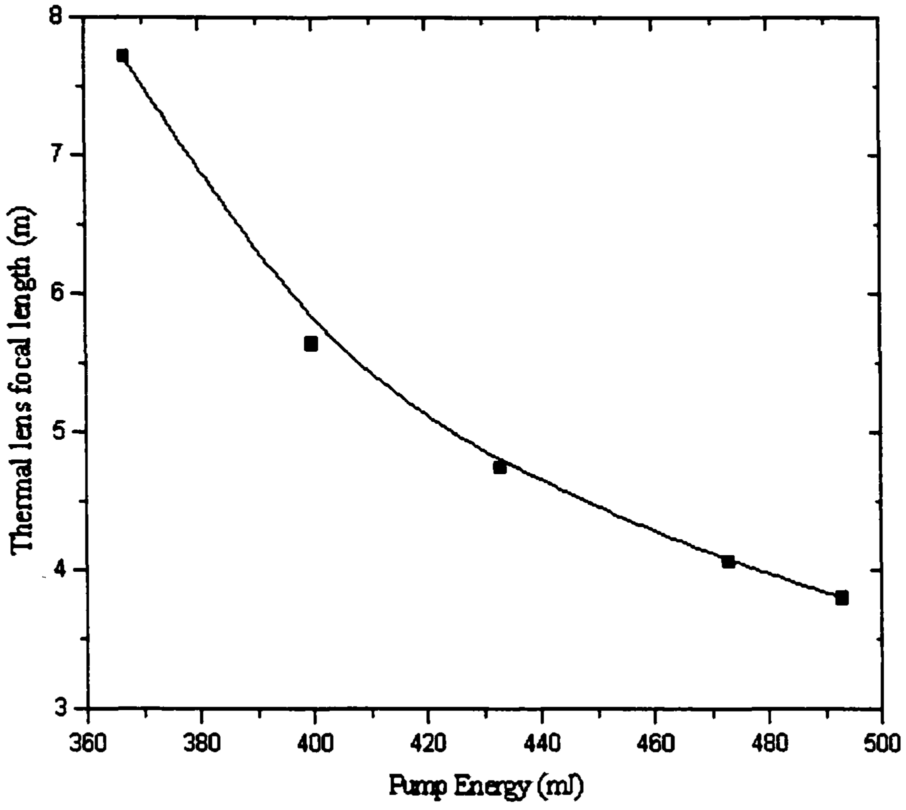

Fig. 5.17. Focal length of thermal lens as a function of the 532-nm pump energy.

The measurements of the thermal lens focal length as function of the pump energy presented in Fig. 5.17 was taken when the Ti:sapphire laser bricks were constantly cooled with 20 °C flowing water. This measurement can help design the Ti:sapphire laser to avoid any optical damage that might be caused by thermal lensing. Without cooling, the focal length of the thermal lens was short, within the range of the cavity length, causing frequent damage to the high reflectivity mirror of the laser cavity, but with cooling it became longer (as shown in Fig 5.17) than the laser cavity length, thus avoiding optical damage.

8. Long-term laser stability measurements

An experiment was run for the purpose of determining the long term stability of the Ti:sapphire laser output energy. This test, eight hours in duration, is the average length of an ozone data flight. Figure 5.18 shows the fluctuations in the 900 nm output energy over an 8-hour period for 30 Hz operation. These fluctuations are due to changes in the power of the 532-nm pump pulse. At the beginning of the test, the pump laser doubler crystal needed to be optimized and tuned every few minutes. After the second hour it was adjusted every 20 minutes and after the fourth hour the output of the pump laser became stable, resulting in a fairly stable Ti:sapphire laser output. In order to obtain a more stable Ti:sapphire output energy, it is recommended that the pump laser be run for several hours before using the 532-nm beam to pump the Ti:sapphire laser. The same test was run for one-hour period to the UV output and it was noted that the UV output was stable.

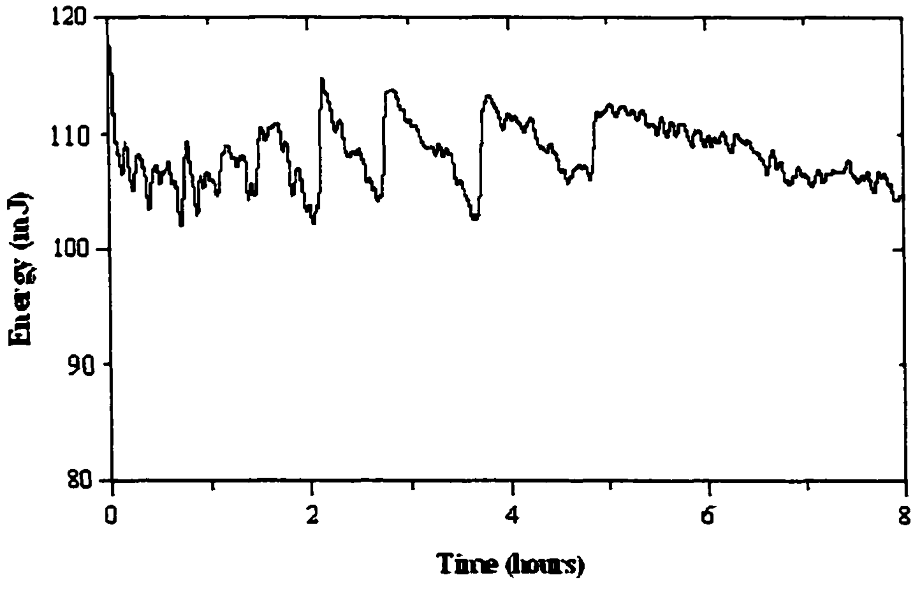

Fig. 5.18 Long-term laser stability of the 900 nm Ti:sapphire output laser energy at 30Hz.

9. Ti:sapphire system stability

There are many factors which can influence the stability of the Ti:sapphire laser output. One factor is sensitivity to alignment of the plano-plano laser cavity mirrors. However, for this particular application, cavity mirror realignment and optimization was not frequently necessary. One issue that did pose a problem was a result of the mounts used for the cavity mirror adjustment. Motorized mounts were utilized to aid in the optimization process; however, the spring loaded slide used to activate the motors did not always return to its center (no motion) position. Thus, over the course of a few hours the motors would slowly drift in one direction or another. It became necessary to disconnect the power to the motors after each realignment to ensure that the motors were not energized unintentionally.

Another factor effecting stability is related to how well matched were the Ti:sapphire laser mode and 532 nm pump volume. To increase stability, it was necessary to maximize this overlap as much as possible. The Ti:sapphire laser cavity was aligned using the seeder laser beam, then the Ti:sapphire laser was aligned to follow the same path as the seeder beam. An IR viewing card was used to assure the same spatial overlap between the seeder beam and the 532-nm laser beam, after the 532-nm laser beam intensity was reduced by optical filters. This is a one-time setup procedure and need not be repeated often unless optical component changes take place in the cavity.

Additionally, laser stability is dependent on how well the seed diode laser beam is aligned to the Ti:sapphire laser cavity. Therefore, it is also crucial that good mode matching be present between the seed laser and the laser mode volume of the Ti:sapphire brick. To ensure good mode matching between the seeder and the Ti:sapphire laser, a spectrometer along with OMA were used to monitor the seeding process. When the seeder and the Ti:sapphire laser were not matched, the spectra linewidth was broad with wings, but when they were well matched, a very shape line without any wings was noticed. This is, again, a one-time procedure and need not be repeated during every laser operation unless changes take place in the system.

References:

1. N. D. Finkelstein, W. R. Lempert, R.B.. Miles, A. Finsh, G.A. Rines, "Cavity locked, injection seeded, titanium: Sapphire laser and application to ultraviolet flow diagnostics," *AIAA paper 96-0177* (Aerospace Science Meeting and Exhibit, 34th, Reno, NV, Jan. 15-18, 1996).
2. Charles E. Hamilton, "Single-frequency, injection-seeded Ti:sapphire ring laser with high temporal precision," *Optics Lett.*, Vol. 17, No. 10, pp 728, 1992.
3. F. Salin, F. Estable, E. Mottay, and L. Brunel, " High-Power, Gain Guided Ti:AL_2O_3 Laser: Theory and Experiment," in *OSA proceedings on advanced solid-state lasers*, Albert A. Pinto and Tso Yee Fan, (eds.), (New Orleans, Louisiana, February 1-3, 1993), pp294.
4. C. Roundy, *Laser Focus*, December 1999.

CHAPTER VI

ULTRAVIOLET HARMONIC GENERATION EXPERIMENTAL RESULTS

In this chapter, we will discuss the experimental results of second and third harmonic generation from the Ti:sapphire fundamental wavelength of 867 or 900 nm. These experimental results will then be compared later to the harmonic generation model of chapter VII.

1. Second harmonic generation results

As was mentioned in Chapter V, both Ti:sapphire laser outputs are frequency doubled and tripled by two LBO nonlinear type I crystals to obtain ultraviolet laser outputs at 289 or 300 nm. Though BBO crystals were originally used, better output was achieved with LBO crystals, resulting in 31 and 30 mJ/pulse at 289 nm and 300 nm respectively, with a resulting total conversion efficiency from IR to UV of 27% and 31% for the on-line and off-line 30 Hz lasers respectively.

The energy of the fundamental Ti:sapphire laser beam and second harmonic laser beam were measured using a broadband power meter (Ophire, Model number 30A-HE-106). The energy of the fundamental Ti:sapphire laser was measured just before the second harmonic crystal. In this experiment, using a Pellin Broca prism, we separated the unconverted fundamental beam from the second harmonic, after the beams exit the second harmonic crystal. At enough distance from the Pellin Broca prism, the power meter was set to measure the second harmonic beam after blocking the unconverted fundamental beam.

The results of the second harmonic generation are shown in Figs. 6.1 and 6.2 together with the energy conversion efficiency from the fundamental to the blue. The maximum energy of the laser output pulse at 433.5 and 450 nm were 56 and 50 mJ with conversion efficiencies from IR to blue of 49 and 52 % respectively. The 49% and 52% are an external conversion efficiency value, that is, second harmonic energy exiting the crystal divided by the total fundamental output from the oscillator.

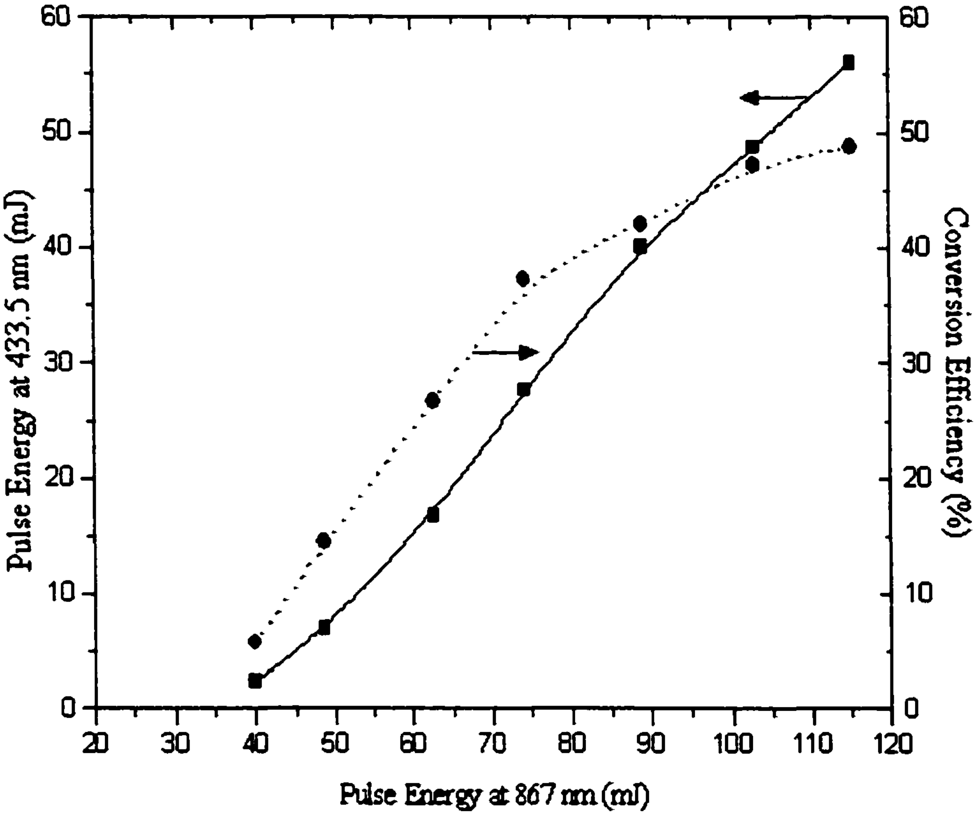

Fig. 6.1 Doubled Ti:sapphire laser energy at 433.5 nm and energy-conversion efficiency versus the fundamental 867 nm laser energy. Solid curve is the output energy at 433.5 nm and doted curve is the conversion efficiency from the fundamental to 433.5 nm.

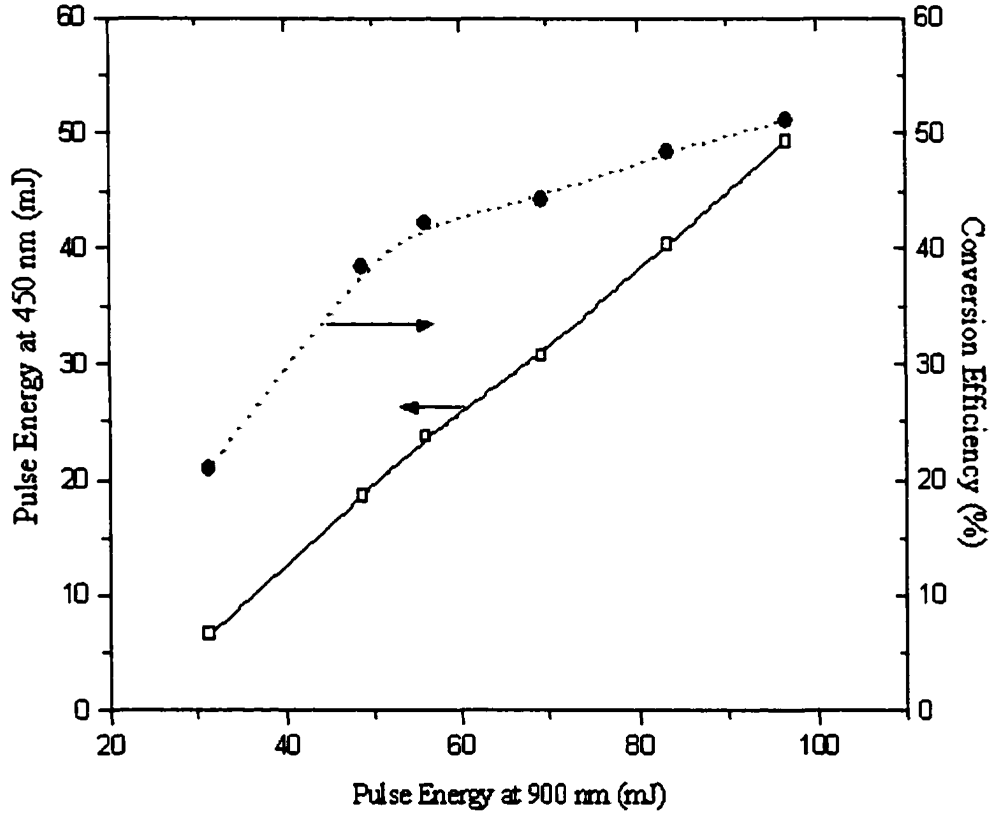

Fig. 6.2 Doubled Ti:sapphire laser energy at 450 nm and energy-conversion efficiency versus the fundamental 900 nm laser energy. Solid curve is the output energy at 450 nm and doted curve is the conversion efficiency from the fundamental to 450 nm.

2. Third harmonic generation

The fundamental and second harmonic beams are orthogonaly polarized. The output from the SHG crystal can be prepared for the THG crystal by passing the beams through a dual waveplate (full waveplate for the fundamental beam and half waveplate for the second harmonic) such that the fundamental and second harmonic polarizations are made parallel before they enter the third harmonic crystal. Then, the THG crystal was oriented so that the fundamental and SHG polarizations were correctly aligned for phase matching within the sum frequency generation (SFG) LBO crystal.

The power of the fundamental Ti:sapphire laser beam and third harmonic laser beam were measured using the same broadband power meter (Ophire, Model number 30A-HE-106). The power of the fundamental Ti:sapphire laser was measured just before the second harmonic crystal. In this experiment, a Pellin-Broca prism was used to spatially separate the unconverted fundamental beam, the second harmonic, and the third harmonic beam after the beams exit the LBO crystal. At some distance from the Pellin Broca prism, the power meter was set to measure the third harmonic beam after blocking the unconverted fundamental and second harmonic beams.

The results of the third harmonic generation are shown in Figs. 6.3 and 6.4 together with the energy conversion efficiency from the fundamental to the ultraviolet. The maximum energy of the laser output pulse at 289 and 300 nm were 31 and 30 mJ with conversion efficiencies from IR to ultraviolet of 27 and 30% respectively.

In order for THG to take place efficiently a photon-mixing ratio of 1:1 between red photons and blue photons is needed. This can only happen with plane waves and an ideal SHG conversion efficiency of 66.6%. The blue photons at 433.5 or 450 nm are twice as energetic as the red photons at 867 or 900 nm, therefore two-thirds of the energy must be at 433.5 or 450 nm and one-third of the energy must be at 867 or 900 nm for there to be a 1:1 photon number ratio. Under this condition, all the photons will most efficiently be utilized.

However, this condition could only occur ideally with a top hat profile beam with a square wave temporal profile, but in practice we have a Gaussian beam profile in time and space. The central part will have high conversion efficiency while the wings will have low conversion efficiency. With the Gaussian beam, the total average SHG conversion efficiency will be less than 66.6%. In order to improve the THG, the SHG efficiency has been intentionally reduced by de-tuning the SHG crystal or by tilting it off perfect phase matching so that the ratio between the photons at the fundamental and the second harmonic can be close to the 1:1 ratio needed for maximum mixing efficiency resulting in optimum UV generation.

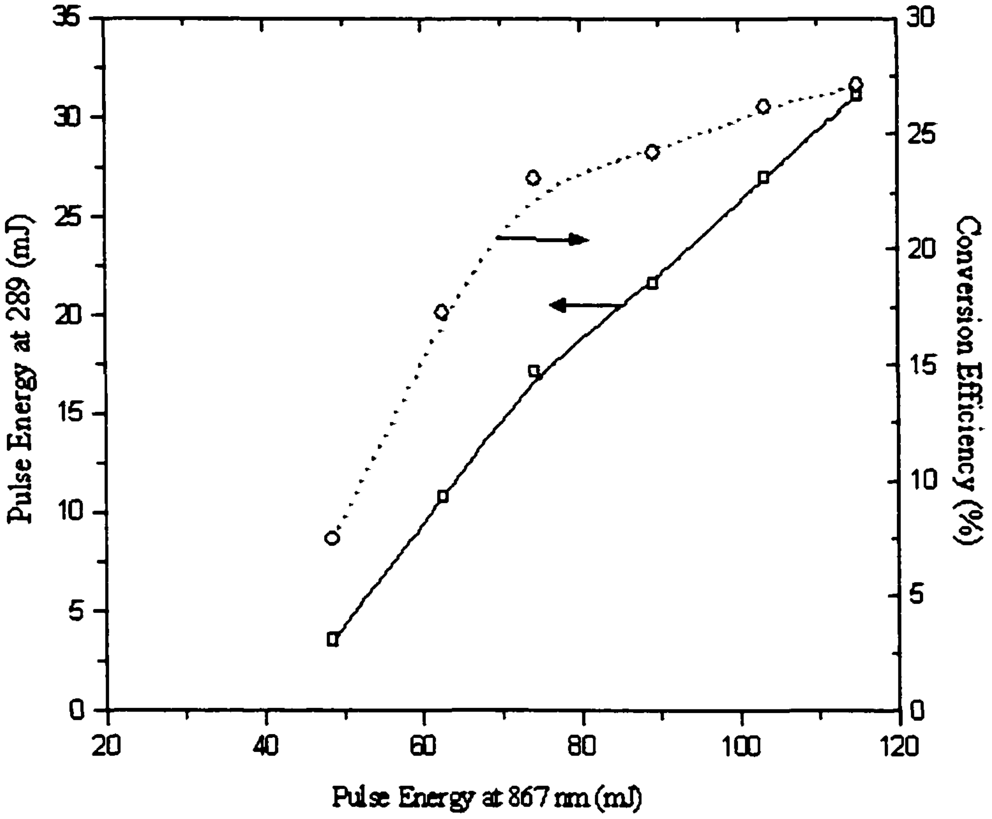

Fig. 6.3 UV laser energy at 289 nm and energy-conversion efficiency versus the 867 nm Ti:sapphire energy. Solid curve is the output energy at 289 nm and the dotted curve is the conversion efficiency from the fundamental to 289 nm.

No noticeable effect of either room temperature or crystal heating by the laser input was observed for the LBO crystals since all the experimental results have been run at room temperature where the change in the ambient temperature is very small. No external cooling or heating was incorporated with the LBO crystals during this experiment. It is probable that when the system is deployed in the field where there will be a change in the ambient temperature, the LBO crystals may need to be installed in a temperature-controlled oven to keep the temperature constant. The main feature of the oven is to provide precise temperature control as well as long-term stability, which is suitable for non-critical phase match applications when LBO crystals are used.

The maximum output energy of the UV laser was measured during many different days and when it showed consistency, the data presented in this chapter was taken. Each point on these figures was an average of two readings.

Since the Ti:sapphire laser cavity was aligned using the seeder laser beam then the Ti:sapphire laser followed the same path that the seeder took. Knowing that, the seeder beam was used to roughly align the LBO crystals and to trace the fundamental beam through the system. The alignment can be accomplished by tweaking the LBO crystal in the XY plane. When the LBO crystals were aligned, the output energy of the second and third harmonic beams was stable for almost one hour except a slight change in the UV output due to mode beating discussed earlier. The crystals did not need further alignment after the first alignment was made.

CHAPTER VII

TI:SAPPHIRE LASER CAVITY MODELING

1. Model development

To understand the physics of the laser, a computer model was developed to simulate the operation of the Ti:sapphire laser. The Ti:sapphire oscillator was pumped by 532 nm laser pulses, which have a short pulsewidth compared to the buildup time of the oscillation within the Ti:sapphire laser cavity (see Fig. 5.5); thus, the initial conditions for the oscillating mode are equivalent to Q-switched resonators [1]. Therefore, past analysis of Q-switched lasers can be extended to this oscillator [2,3]. Since the Q value of the cavity is constant, this operation is referred to as gain switching, and results in a single gain-switched (Q-switched) pulse. The Ti:sapphire laser system is an ideal four-level laser system, and a schematic diagram of this system is shown in Fig. 7.1. The transitions from the pumped level to the upper laser level are fast compared to the purely radiative spontaneous decay of the upper laser state. Also the transition from the lower laser level to the ground state is fast. Since the pump pulsewidth is short, the spontaneous decay occurring during the pulsewidth can be neglected, but there is another non-radiative mechanism due to the increase of the brick's temperature was included.

A laser model that describes the dynamics of laser action was based on the laser rate equations, which describe the time dependent change in the population inversion, n, and the photon density, ϕ [2-4] as,

$$\frac{dn}{dt} = -\gamma c \sigma_{se} n \phi \qquad (1)$$

$$\frac{d\phi}{dt} = c \sigma_{se} n \phi - w_L \phi \qquad (2)$$

where n is the difference between the population in the upper and lower laser levels, n_2, n_1 as shown in Fig. 7.1, σ_{se} is the stimulated emission cross section, c is the speed of light, w_L is the loss rate, and γ is the inversion reduction factor. The inversion reduction factor is a constant, which can take a value between zero and two [3].

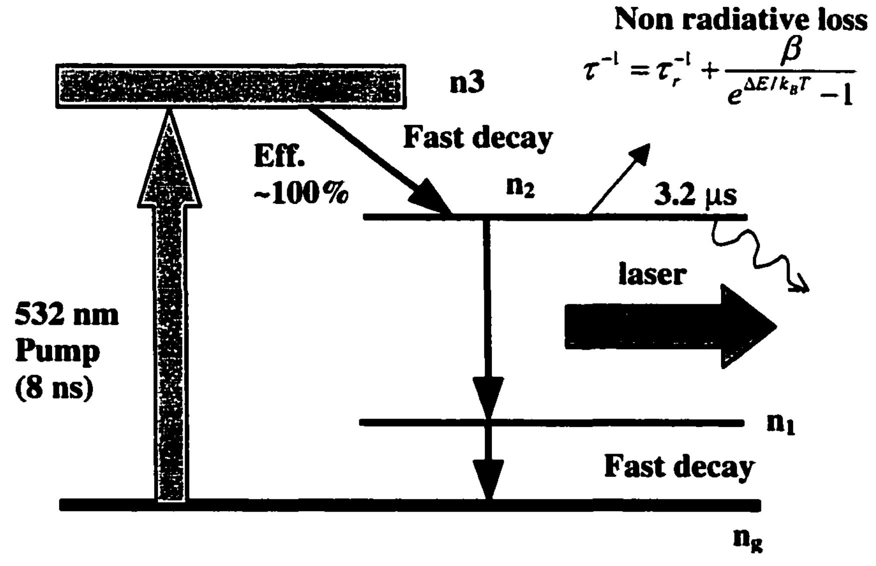

Fig. 7.1 Energy level diagram for the four-level laser that can describe the operation of the Ti:sapphire laser.

Eqs (1) and (2) are implemented in the model to simulate the evolution of the Ti:sapphire laser pulse by an iterative process. Each variable of these two equations depends on the initial conditions such as pump efficiency, inversion density, gain, losses, thermal lensing, and cavity parameters. All these are calculated before solving these two coupled equations. A diagram of the Ti:sapphire cavity model is shown in Fig. 7.2, which shows the different steps used to calculate the Ti:sapphire energy and pulsewidth.

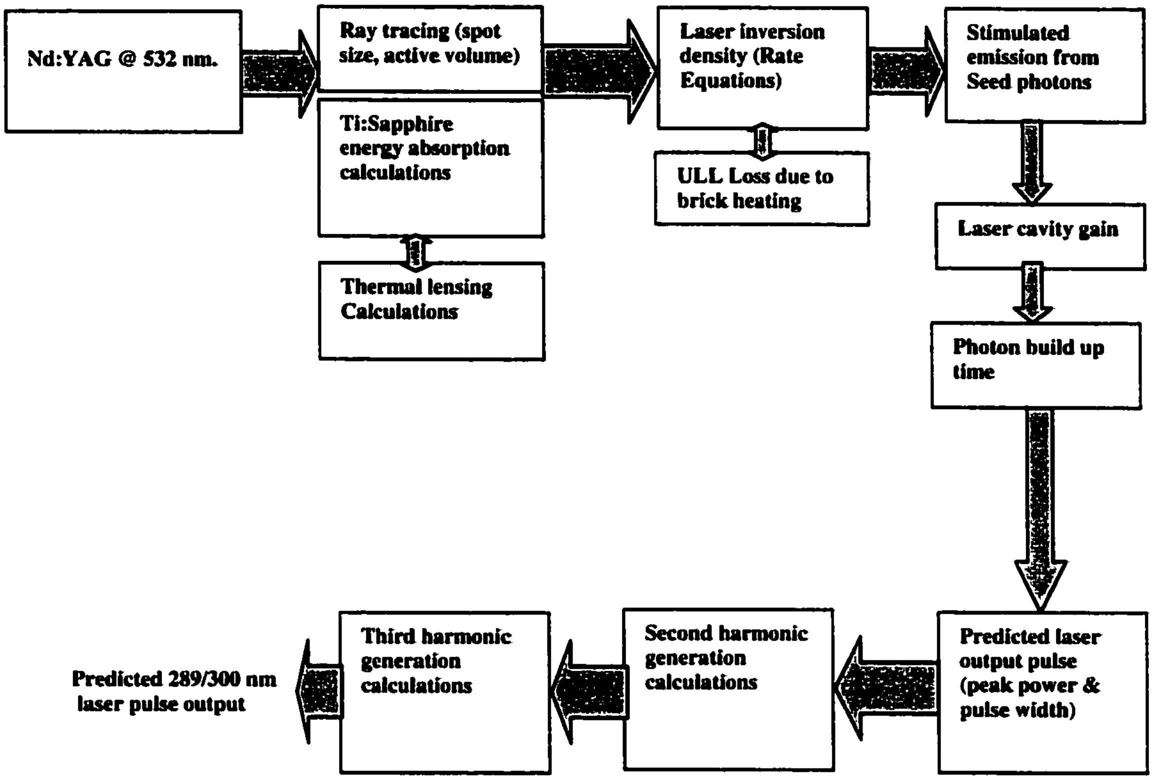

Fig. 7.2 Diagram of laser cavity model.

To obtain the initial conditions the pump energy is entered into the model as,

$$E_{pump} = P\,T_p\,, \tag{3}$$

where P is the pump power, and T_p is its pulsewidth. The stored energy, E_{st} is then determined from

$$E_{st} = \eta_1 \eta_2 \eta_3 \eta_4 E_{pump} \quad (4)$$

where η_1 is the 532 nm absorption efficiency, η_2 is the optical coupling efficiency, η_3 is the color efficiency, and η_4 is the fluorescence storage efficiency. These efficiencies are calculated from

$$\eta_1 = \frac{E_{abs}}{E_{pump}} \quad \text{where}$$

$$E_{abs} = E_{pump} - E_{att} \text{ and } E_{att} = E_{pump}\left(e^{-\sigma_{532} N_{ion} x}\right)$$

thus $$\eta_1 = 1 - e^{-\sigma_{532} N_{ion} x} \cong 1 \quad (5)$$

where, σ_{532} is the absorption cross section of the 532 nm beam inside the Ti:sapphire crystal, ($\sigma_{532} = 5.13 \times 10^{-20}$ cm^2). N_{ion} is the number of Ti active ions in the laser crystal, ($N_{ion} = 4.85 \times 10^{19}$ ion/cm^3). and x is the total length of the active medium, (x = 4 cm).

Based on measurements we assumed there was one percent loss of the pump energy at each surface of the two Ti:sapphire bricks; thus,

$$\eta_2 = 98\% \quad (6)$$

The color efficiency is given by

$$\eta_3 = \frac{E_L}{E_p} = \frac{\lambda_L}{\lambda_p} = \frac{532}{900} = 0.59 \quad (7)$$

and the fluorescence storage efficiency is $\eta_4 = 1$ for gain switched lasers. (8)

The population inversion is obtained from the stored energy, the energy of the pump photon, E_p, and the laser pump volume, V, from

$$N = \left(\frac{E_{st}}{E_p}\right) / V \quad (9)$$

The pump volume, *V*, can be estimated using a ray tracing program to calculate the laser beam radius inside the cavity, which has a beam waist of w_p and brick length of *x*

$$V = \pi(w_p)^2 x \tag{10}$$

The inversion density is then stretched across the length of the laser cavity to account for the ratio of the crystal length to the cavity length that is x/L. This stretching fills the cavity with a uniform inversion density. Thus the stretched inversion density has the form

$$n = N\left[\frac{x}{L}\right] = \left[\frac{E_{st}/E_p}{V}\right]\left[\frac{x}{L}\right] \tag{11}$$

The small signal gain coefficient g_0 is then calculated from the stretched inversion density and the stimulated emission cross-section, σ_s, as,

$$g_o = \sigma_s n \tag{12}$$

The loss rate is computed from the loss coefficients. The loss due to the leakage of photons from the cavity mirrors is computed as

$$\alpha_r = -\frac{1}{2L}\ln(R_1 R_2), \tag{13}$$

where R_1, R_2 are the reflectivities of the output coupler and the end mirror respectively. The loss due to intercavity elements is computed as

$$\alpha_s = -\frac{1}{2L}\ln(1 - l_c), \tag{14}$$

where l_c is the cavity loss from all optical elements except the cavity mirrors. Then the total loss can be obtained from

$$\alpha = \alpha_s + \alpha_r \tag{15}$$

As temperature is increased in the Ti:sapphire brick, the inversion density of the Ti:sapphire changes significantly. The fluorescence lifetime decreases with increasing temperature above 300 K as we discussed before in chapter III. The temperature dependence of the upper laser level lifetime can be interpreted using the expression [7]

$$\tau_f^{-1} = \tau_r^{-1} + \frac{\beta}{e^{\Delta E / k_B} - 1} \tag{16}$$

where τ_r^{-1} represent the radiative decay rate of the upper laser level ($\tau_r^{-1} = 3$ μs). The second term describes radiationless quenching due to phonon absorption to a higher level. β is the rate constant for the radiationless transition ($\beta = 2.62 \times 10^6$ μs^{-1}) and ΔE is the potential barrier for the process (ΔE = 0.496 eV). This can be assumed as a temperature dependent loss mechanism and can be added to the cavity loss mechanisms. The loss rate W_L is then calculated from

$$W_L = \alpha c + \tau_f^{-1} \tag{17}$$

where c is the speed of light.

Starting with initial values as shown in table 7.1 for loss, gain, and cavity parameters, the simulation of the Ti:sapphire laser pulse can be started after assuming the initial value energy, E_o and photon flux, ϕ_o. Assuming the initial seed emission into a solid angle, dΩ of 1 mrad from the optical axis of the laser cavity, the initial energy available for lasing is calculated from

$$E_o = E_p N A x \frac{L}{c\tau_f} \frac{d\Omega}{4\pi} \tag{18}$$

where A= $\pi\omega^2$ is the area of the beam in the laser crystal, and τ_f is the fluorescence lifetime. The initial photon flux is calculated using (18) as

$$\phi_o = \frac{E_o}{AxE_p} \tag{19}$$

Table 7.1: Model parameters.

Number of active ions	4.8 x 10^{19} ion/cm^3
Cavity length	130cm
Wavelength	900 nm or 867 nm
Pump diameter	2 mm
Laser diameter	2 mm
Loss per pass	6 %
High reflectivity mirror	99%
Output coupler mirror reflectivity	40% @ 900 nm or 35% @867nm

These values along with the initial loss rate, w_L, are used in solving the rate equations (1) and (2) numerically for n_i and ϕ_i using the Euler method [4]. In the Euler form, the equations for the population inversion can be written as

$$n_{i+1} = n_i - (n_i \sigma_{se} c \phi_i)\Delta t \tag{20}$$

$$\phi_{i+1} = \phi_i + [(n_i \sigma_{se} c \phi_i) - (w_l \phi_i)]\Delta t, \tag{21}$$

The variables in equation (20) and (21) represent the same components as those in equation (1) and (2) and *i* is used as the incremental time-step counter. The two equations are coupled so they must be solved in an iterative manner that allows successive values of population inversion density and photon density to be used to calculate the next value of each. The initial values of the population density and photon density must be calculated from Eqs. (11) and (19) before solving these two-coupled equations.

The output laser pulse energy is calculated by summing the power at the output coupler over time as

$$E_{out} = \phi_i\,(1 - R_1)\,E_L\,A\,c\,\Delta t \tag{22}$$

where E_L is the energy of the laser photon and A is the area of the output beam spot, (Ac Δt) is the volume of the laser beam in a unit of time Δt, ϕ_I E_L is the energy density of the photons inside the cavity and $(1-R_1)$ is the percentage of the energy that leaks out of the cavity through the output coupler mirror.

The comparison of this model with experimental results will be given in section 3.

2. Thermal lensing effect in Ti:sapphire bricks

In any laser material, there are optical distortions, which are a result of both temperature and stress gradients due to the energy absorbed in the laser material from the pump laser beam. The energy deposition in the Ti:Sapphire laser bricks is high enough at repetition rates of 30 Hz that the production of a thermal lens is possible. The laser brick will act as a lens within the laser cavity, which might cause optical damage as well as affect the doubling and tripling conversion processes. For this reason we included in our model a computation accounting for the effect of thermal lensing.

The change of the refractive index N(r) in any cylindrical media can be separated into a temperature and stress-dependent variation, given by [7]

$$N(r) = n_0 + \Delta n(r)_T + \Delta n(r)_\varepsilon \tag{23}$$

where n(r) is the radial variation of the refractive index, n_0 the refractive index at the center of the brick, and $\Delta n(r)_T$, $\Delta n(r)_\varepsilon$ are the temperature and stress-dependent changes of the refractive index, respectively. The temperature dependent change of the refractive index can be expressed as

$$\Delta n(r)_T = [T(r) - T(0)]\left(\frac{dn}{dT}\right) \tag{24}$$

$$\Delta n(r)_\varepsilon = -\frac{Q}{4K}\left(\frac{dn}{dT}\right)r^2 \tag{25}$$

where K, is the thermal conductivity and Q is the heat generated in a unit volume. In equation (25), the refractive index in a laser brick shows a quadratic variation with radius r. This perturbation is equivalent to the effect of a spherical lens. Innocenzi et al. [5] published a thermal model for continues-wave (CW), end-pumped solid state laser crystals. The effective focal length of the laser crystal is given by [5]

$$f_{eff} = \left[\frac{\pi K_c \omega_p^2}{P_{ph}(dn/dT)}\right][1 - \exp(-\alpha l]^{-1} \tag{26}$$

where K_c is the thermal conductivity (0.35 W/cm. K) of Ti:sapphire, *dn/dT* is the change in the index of refraction due to temperature for Ti:sapphire (1.28×10^{-5} K^{-1}), ω_p is the pump radius, α the absorption coefficient of the Ti:sapphire crystal at 532-nm, l is the length of laser crystal and P_{ph} is the fraction of pump power that results in heating. This thermally induced focal length f_{eff} produced in Ti:sapphire is then added to the curvature of the end laser cavity mirror. A comparison of the calculated thermal lens focal length from this model with experiment will be given in the section 3.

3. Ti:sapphire Modeling Results

With this model, a simulation of the Ti:sapphire laser pulse evolution has been made. The input parameters used in this model are listed in Table 7.1. Figure 7.3 shows the simulated 900-nm output of the Ti:sapphire laser pumped with a 450 mJ Nd:YAG laser pulse along with the measured experimental results.

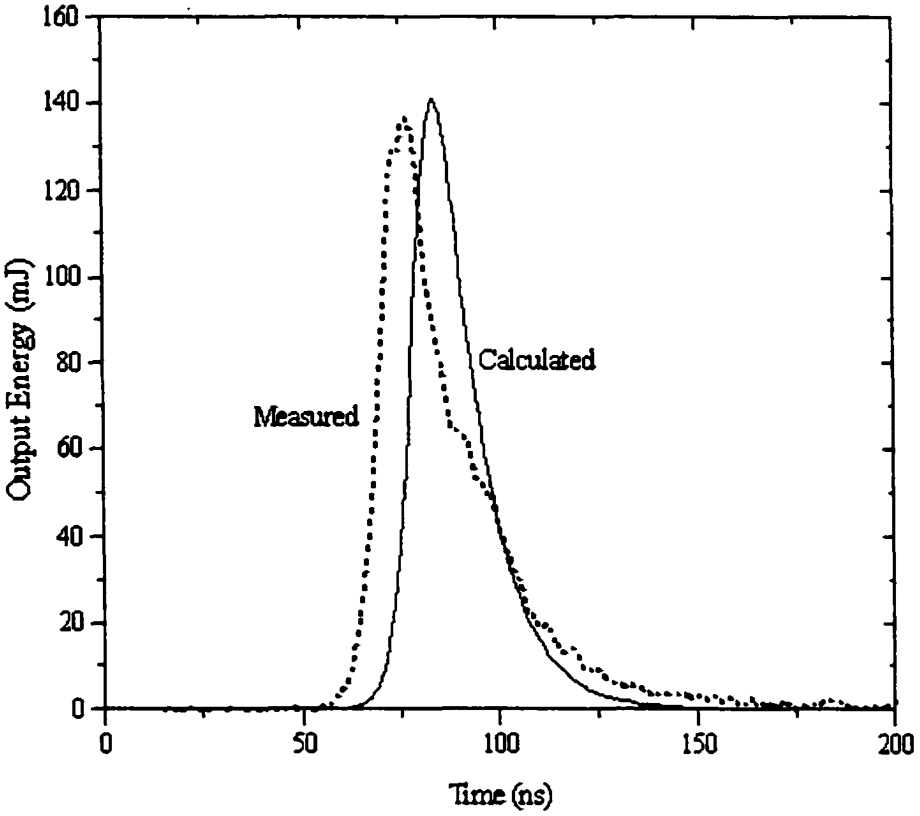

Fig. 7.3. Simulated output pulse of the Ti:sapphire laser at 900 nm, with a pump energy of 450 mJ measured (dashed) and simulated (solid). The measured output energy and pulse width are 137 mJ and 16 ns respectively, while the calculated output energy and pulse width are 141 mJ and 15.9 ns respectively.

The results from this model are in good agreement with the corresponding experimentally measured pulse shape and energy. The calculated pulse energy and width were 141 mJ and 16 ns while the measured pulse energy and width were 137 mJ and 15.9 ns.

Figure 7.4 shows the measured and calculated pulse energy output of the Ti:sapphire laser at 900 nm and 30 Hz repetition rate as a function of the 532 nm pump energy at different temperatures. From Fig. 7.4 we can see that the theoretical results are in agreement with the experiment at high pump energy but they differ at laser threshold. The model gives lower values for the lasing threshold that might indicate that at high pump energies the thermal lens acts to make the laser cavity stable, but at low pump energies there is no thermal lens and thus the cavity experience higher loss due to the unstable flat-flat mirror cavity configuration.

The calculated slope efficiency at low pump energies was 33.3% at 300 K and is close to the 33.6% slope efficiency of the experiment. Noteworthy, as the temperature of Ti:sapphire crystal increases the non-radiative loss increases leading to a decrease in output energy and slope efficiency. The slope efficiency of the experiment was close to the calculated slope efficiency at 500 K.

The instantaneous increase in the bricks temperature can be calculated using Eq.27

$$Q = mc\Delta T \tag{27}$$

where Q is amount of heat deposited in one second, m is the mass of the brick, and ΔT is the change in the bricks temperature. The change in temperature at 500 mJ pump energy is 557 K.

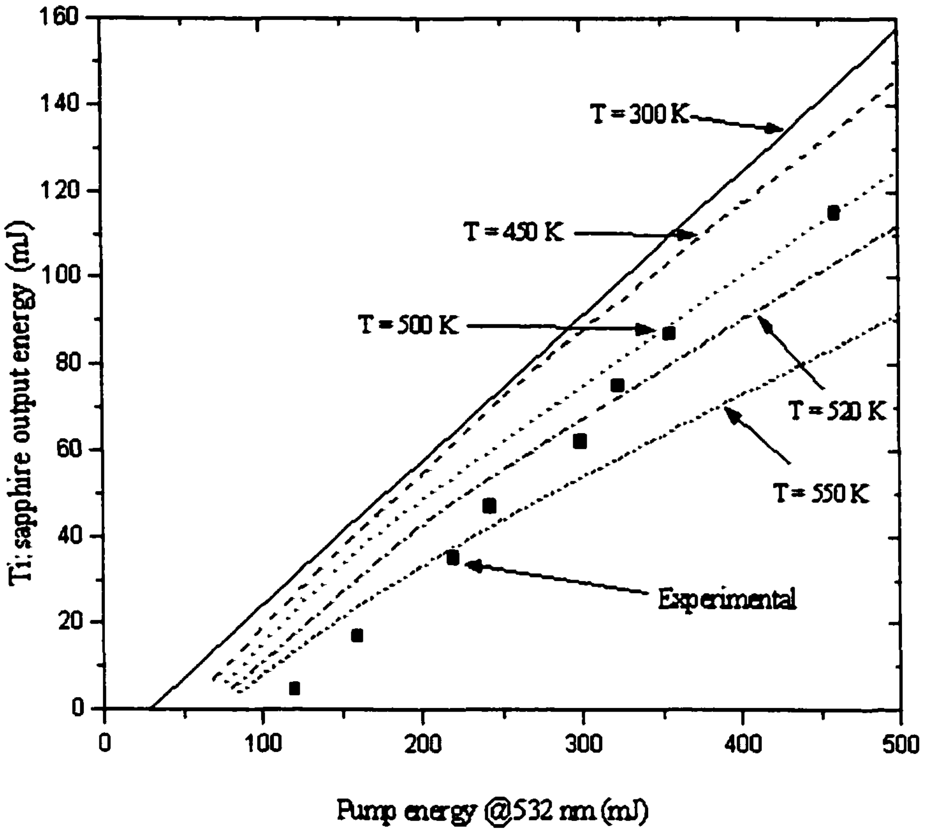

Fig. 7.4 Measured and calculated pulse energy output of the Ti:sapphire laser at 900nm and 30 Hz repetition rate as a function of the 532 nm pump energy at different temperatures. Solid line is modeled results and squares are the experimental results.

Since the pulsewidth of the Ti:sapphire laser is an important factor that characterizes the laser output pulse profile, the model was used to calculate the pulsewidth of the 900-nm laser pulse at different output energies and compared to experiment results at 30 Hz as shown in Fig. 7.5. As expected as the laser energy increases, the higher gain in the cavity causes the pulsewidth to decrease. The model adequately represents this phenomenon.

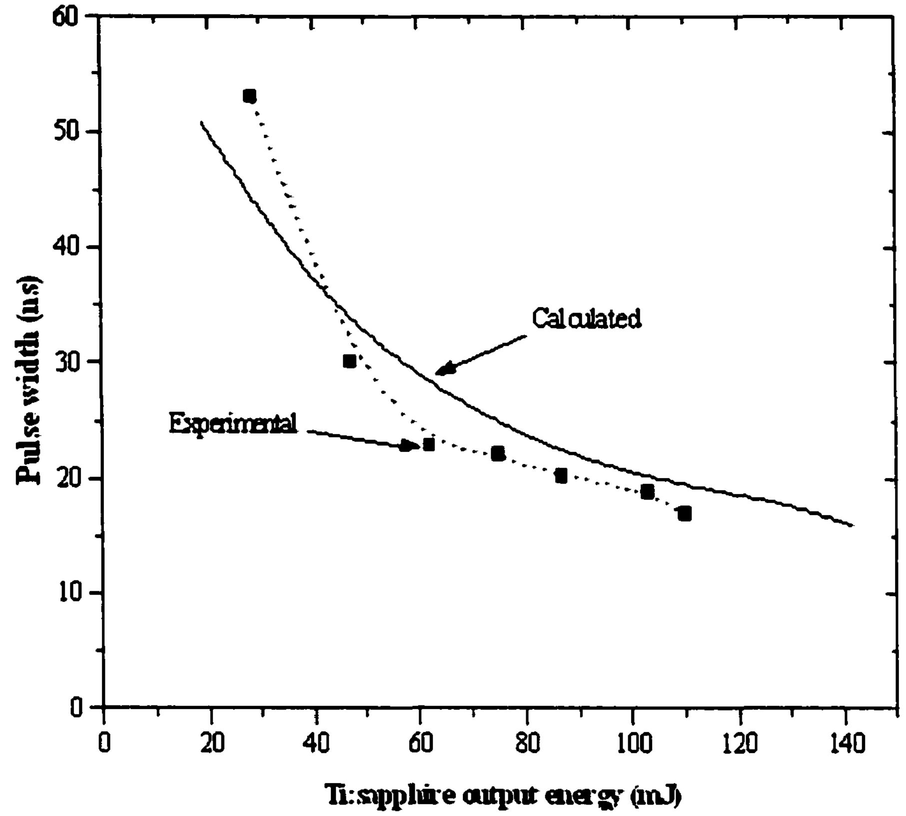

Fig. 7.5 Pulsewidth of the Ti:sapphire laser as a function of the Ti:sapphire output energy at 900 nm. Solid line is the model results and squares are the experimental results.

As was mentioned in the earlier section, the Innocenzi model [5] of thermal lensing was used to calculate the focal length of the induced thermal lens. Figure 7.6 shows the calculated focal length due to thermal lensing using Innocenzi compared with the experiment. There is poor agreement at low pump power because this model was designed for a continuous Nd:YAG laser and we assumed that steady state heat transfer exist after a short time of laser operation [5]. But at higher pump average power, the model is in good agreement with the experiment. The model assumes water cooling of the bricks, and when no cooling was present, the thermal lens was much shorter than shown in Fig. 7.6, resulting in optical damage to the high reflectivity mirror of the laser cavity due to thermal lensing so it was necessary to cool the laser brick to reduce the thermal lensing.

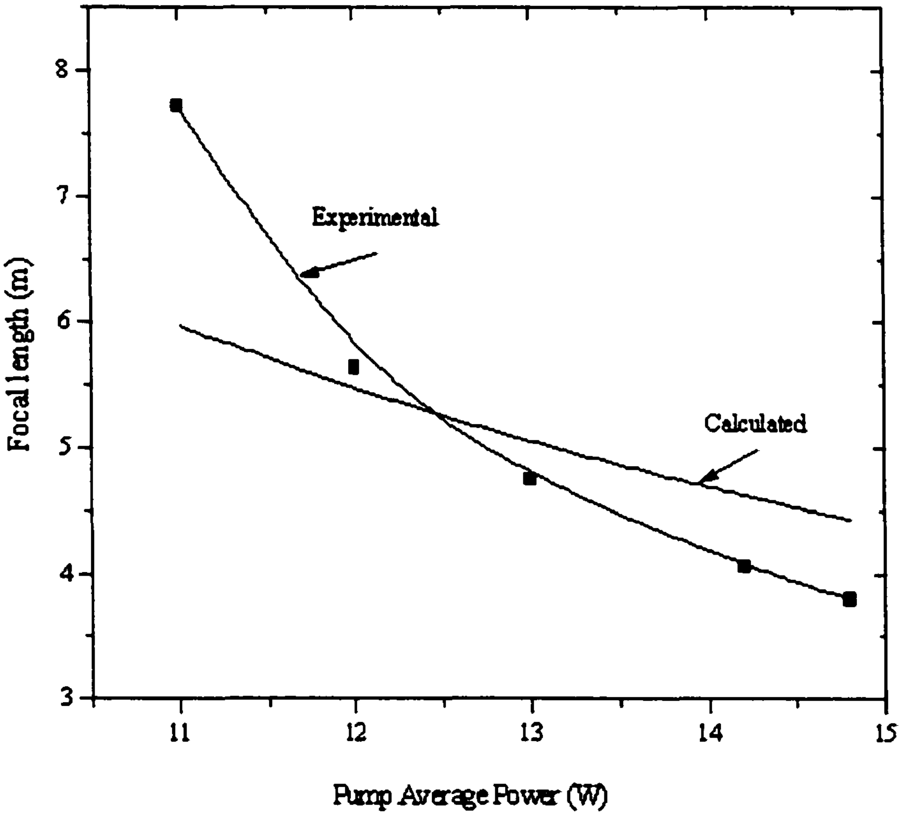

Fig. 7.6. Thermal focal length as a function of the 532-nm pump average power.

4. Model sensitivity.

Model outputs such as pulse energy and pulsewidth are sensitive to a few parameters namely the reduction factor, internal cavity loss and the pump beam diameter. Thus these parameters were varied in the model to determine their sensitivity.

It is clear from Fig. 7.7 that the inversion reduction factor γ affects the output energy while it has little effect on the laser pulsewidth. For each stimulated photon created, the population inversion changes by a value of γ. The inversion reduction factor γ has been chosen in the model to have a value of 1. With this value we could obtain results that are in good agreement with the experiment. The model results, presented in Fig. 7.7, were taken at pump energy of 500 mJ.

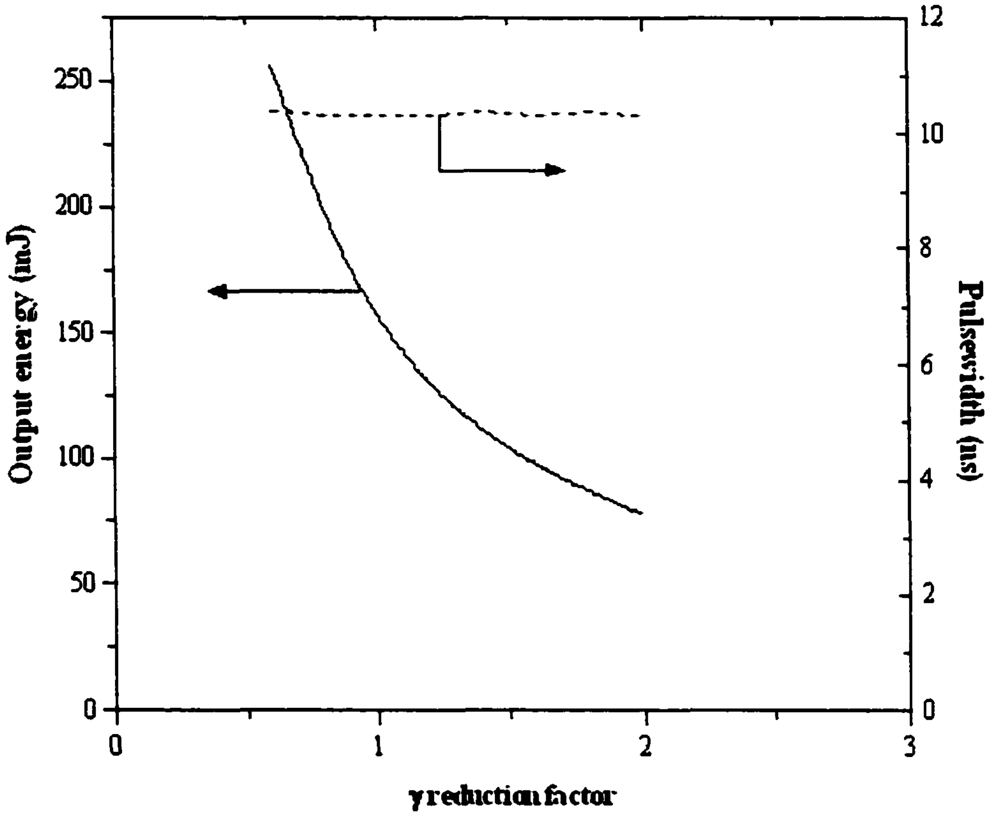

Fig. 7.7. Reduction factor versus output energy and pulsewidth of the Ti:sapphire laser.

There are four dispersive elements and two Ti:sapphire bricks in the laser cavity which combine to have more than 6% loss per cavity round trip. To see how the intercavity loss will affect the pulse output energy and its pulsewidth, the laser pulse energy and its pulsewidth have been calculated at different values of intercavity loss, as shown in Fig. 7.8.

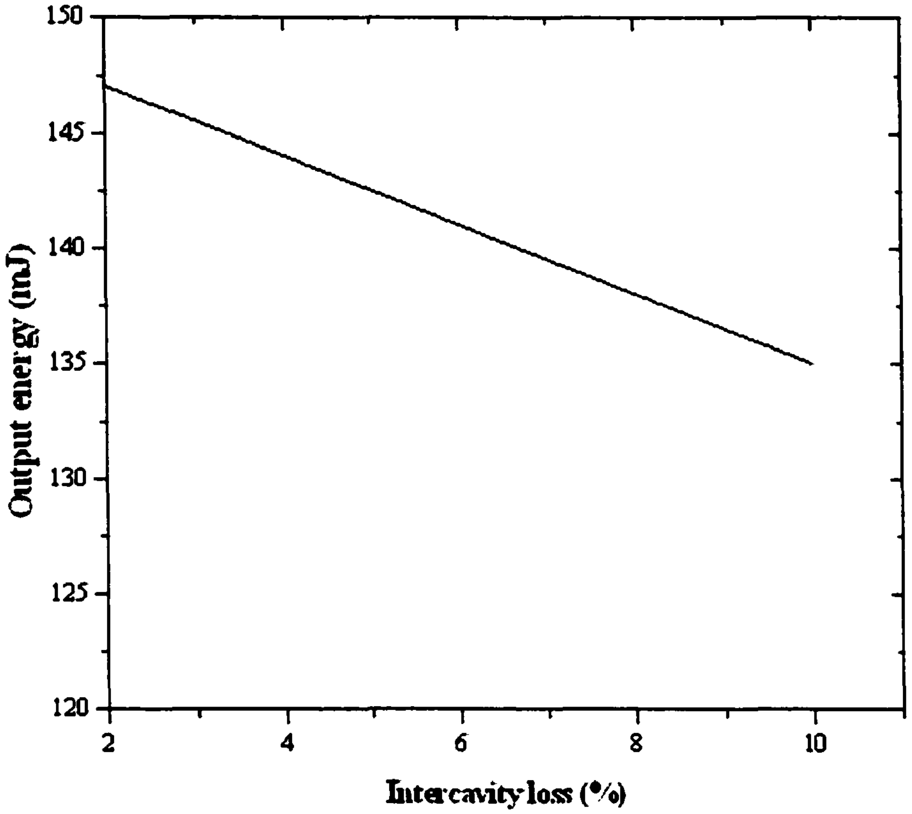

Fig. 7.8. Output pulse energy of Ti:sapphire laser (900 nm) as a function of the intercavity loss percentage at 500 mJ pump energy.

As shown in Fig. 7.8 the intercavity loss has a small effect on the output pulse energy.

It was found experimentally that the overlap between the pump beam and the Ti:sapphire laser cavity mode in the laser brick has a large effect on the output pulse energy. To understand how much the overlap affects the output energy, the output energy of the laser model has been studied as a function of the ratio of the diameter of the laser beam to the diameter of the pump beam. The results are shown in Fig. 7.9 at a pump energy of 500 mJ.

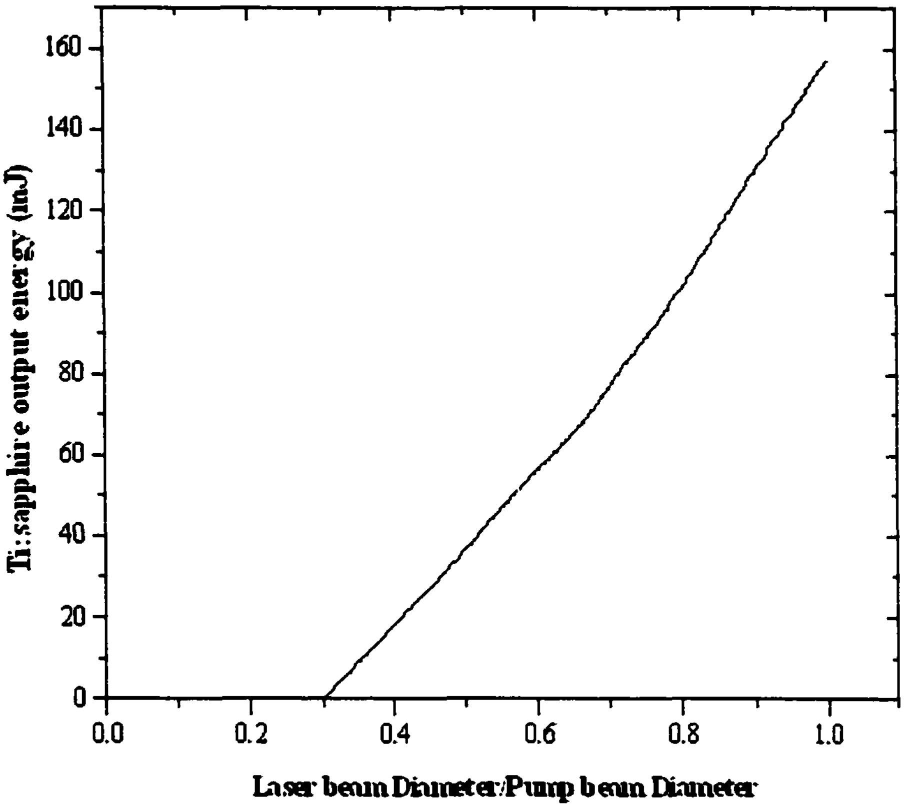

Fig. 7.9 Output pulse energy as a function of the overlap ratio.

It was found that the overlap ratio has a very large effect on the output pulse energy. To maximize the output pulse energy, great care must be given to the overlap between the pump and the laser mode volume.

5. Model limitations

A laser model has been developed to understand the physics of the Ti:sapphire laser operation and guide the experimental work to improve the laser performance. It has been shown that the model results agree with the experimental results and can reasonably predict the output energy and the pulsewidth of the Ti:sapphire laser pulse. However, this model cannot be used to study the spatial or spectral properties of the laser. It is limited to the temporal characteristics of the output laser pulse. The model is based on the assumption that we have only one mode oscillating inside the laser cavity; thus, it cannot be used to predict the linewidth or cavity modes of the output laser beam. Additionally, this model cannot account for the pump repetition rate, which has an obvious effect on the output of the laser pulse because no detailed account of the brick thermal loading is calculated.

References:

1. John M. Eggleston, Larry G. DeShazer, and Keneth W. Kangas, "Characteristic and kinetic of Laser-Pumped Ti:Sapphire Oscillators," *IEEE J. Quantum Electron.* Vol 24, No.6, 1009 (1988).
2. William G. Wagner and Bela A. Lengyel, "Evolution of the Giant Pulse in a Laser," *J. Appl. Phys.* Vol 34, No. 7, 2040, (1963).
3. John J. Degnan, "Theory of the Optimally Coupled Q-Switched Laser," *IEEE. J. Quantum Electron.* 25 (2), 214-220 (1989).
4. D Barry Coyle, David V Guerra and Richard B Kay, " An interactive numerical model of diode-pumped, Q-switched/cavity-dumped lasers," J. *Phys, D:Appl. Phys.*, 28, 452-462, (1995).
5. M. E. Innocenzi, H. T. Yura, C. L. Fincher, and R. A. Fields, "Thermal modeling of continous-wave end pumped solid-state laser," *Appl. Phys. Lett.* 56, 1831-1833, (1990).
6. Koechner, Walter, *Solid-State Laser Engineering*, Springer-Verlag Berlin Heidelberg New York, 1988, p. 478.
7. Powell, Richard, *Physics of Solis-State Laser Materials*, AIP Press, New York, 1998.

CHAPTER VIII

HARMONIC GENERATION MODEL

Since the 532 nm pump laser energy is limited and the relation between the input energy and third harmonic conversion efficiency is not a linear relation at high values of the input fundamental energy, we need to maximize the THG efficiency. In order to do this we need to have a good understanding of harmonic generation in nonlinear crystals and what laser parameters drive the THG efficiency. This chapter will discuss briefly the physics of the second and third harmonic generation and the different laser parameters that affect them. Then results of the harmonic generation model will be presented and compared to experiment.

1. Basic Equations of Second-Harmonic Generation

In the process of harmonic generation a wave of frequency ω_l is incident on a SHG crystal producing a polarization wave at the second harmonic of $2\omega_l$ inside the crystal, which has a phase velocity and wavelength determined by the index of refraction of the fundamental wave, ω_l. A transfer of energy from this polarization wave to an electromagnetic wave at a frequency $2\omega_l$ takes place and the index of refraction for the doubled frequency determines the phase velocity and the wavelength of this electromagnetic wave [1]. For efficient second harmonic generation, it is important that the phase velocities of the two waves be identical so that the second harmonic generated at different points along the path of the nonlinear crystal add in phase [2]. If the created electromagnetic wave has the same phase as the original wave, the created waves will principle plane) waves in an anisotropic medium. One of the waves, called the ordinary wave, sees a constant index of refraction n^o independent of its direction of propagation. The second wave, or the extraordinary wave, sees a refractive index n^e (θ) that is dependent on its direction of propagation. The angle θ describes the direction of propagation relative to one of the principal axes of the crystal. In a crystal where n^e is greater than n^o, phase matching may be achieved by finding the angle of propagation θ_{pm} to satisfy the equation

$$n_\omega^o = n_{2\omega}^e(\theta_{pm}) \qquad (2)$$

where n^o and n^e are the ordinary and extraordinary indices respectively and θ_{pm} is the phase matching angle.

There are two types of angle phase matching in birefringent crystals [4]. In second harmonic generation, type I phase matching refers to the case where either the ordinary or the extraordinary wave has the same polarization. In type II phase matching, the pump wave is polarized so that one of its orthogonal components is ordinary and the other is extraordinary. The phase matching used in the present experiment was of type I.

The control of the refractive indices at each wavelength is important in order to establish the phase matching condition $\Delta k = 0$ shown in Eq.1. In practice, angle tuning and temperature tuning are two methods used to achieve this phase matching. Angle tuning involves the precise angular orientation of the crystal with respect to the propagation direction of the incident beam and was used in the present experiment.

It is very important that the laser source in second harmonic generation have a high power density, small beam divergence, and a narrow linewidth in order to achieve maximum second harmonic power conversion [1]. Conversion efficiency, the ratio of the power generated at the second harmonic wavelength to that incident at the fundamental is given by [1]:

$$\frac{P_{2\omega}}{P_{\omega}} = l^2 K \frac{P_{\omega}}{A} \frac{\sin^2(\Delta kl/2)}{(\Delta kl/2)} \tag{3}$$

where P_{ω} and $P_{2\omega}$ are the powers of the fundamental and second harmonic beams respectively, l is the length of the nonlinear crystal, A is the area of the fundamental beam, and K is a constant for a given wavelength and a given nonlinear material given by [3].

$$K = \frac{\omega_1^2 d_{eff}^2}{nc^3 \varepsilon_0} \tag{4}$$

where d_{eff} is the nonlinear coefficient of the crystal used, c is speed of light, ε_o is permitivity, and n is the refractive index. From Eq. 3, it is clear that the second harmonic power generation is strongly dependent on the phase mismatch expressed by the sinc^2 function which is unity at Δkl=0.

The conversion efficiency depends on the laser parameters such as power density, beam divergence, and spectral linewidth, and parameters associated with the nonlinear crystal such as the nonlinear coefficient value, the angular and thermal deviation from the optimum operating point, crystal length, and absorption. To improve the conversion efficiency the laser beam must exhibit a high power density, small finite divergence and a narrow linewidth. The nonlinear crystal should have a high value of nonlinear coefficient and low absorption. Also the temperature of the nonlinear crystal should be controlled and kept at the optimum operating point.

2. Harmonic Generation Model

Theoretical calculations of conversion efficiency to the second and third harmonic of the Ti:Sapphire laser were made for an LBO nonlinear crystal, to provide a baseline for this research. This model was developed originally at NASA Langley Research Center [5]. Nonlinear three wave mixing processes can be described by three Maxwell's equations with slowly varying amplitudes ε_s, ε_i, and ε_p, shown as equations 5a-c [6]. These amplitudes represent the signal, idler, and pump wave amplitudes, respectively, and $\omega_{(s,i,p)}$ are the corresponding angular frequencies. Equation 7 is the phase matching condition, where the Δk term for the phase matching condition can be calculated from several different input parameters. The input parameters used were: the energy of the incident Ti:sapphire fundamental laser beam, the spectral linewidth of the laser, the diffraction limited divergence, the diameter of the laser beam, the spontaneous emission lifetime of the laser, and the length of the LBO crystal used in this experiment.

$$\frac{d\varepsilon_s}{dz} = i\frac{d_{eff}}{c}\frac{\omega_s}{n_s}\varepsilon_p\varepsilon_i^* \exp(i\Delta kz) - \alpha_s\varepsilon_s \qquad \text{Signal beam} \qquad (5\text{-a})$$

$$\frac{d\varepsilon_i}{dz} = i\frac{d_{eff}}{c}\frac{\omega_i}{n_i}\varepsilon_p\varepsilon_i^* \exp(i\Delta kz) - \alpha_i\varepsilon_i \qquad \text{Idler beam} \qquad (5\text{-b})$$

$$\frac{d\varepsilon_p}{dz} = i\frac{d_{eff}}{c}\frac{\omega_p}{n_s}\varepsilon_s\varepsilon_i \exp(i\Delta kz) - \alpha_p\varepsilon_p \qquad \text{Pump beam} \qquad (5\text{-c})$$

The electric field E_ω at frequency ω is given by

$$E_\omega = \tfrac{1}{2}\left\{\varepsilon_\omega \exp[-i(\omega t - kz)] + \varepsilon_\omega^* \exp[i(\omega t - kz)]\right\} \qquad (6)$$

and the phase velocity mismatch is defined by

$$\Delta k = k_1 + k_2 - k_3 \qquad \text{and} \qquad \omega_p = \omega_s + \omega_i \qquad (7)$$

The subscripts p, s, and i refer to the pump, signal, and idler waves, respectively, as is customary. The coefficients d_{eff} and α are the effective nonlinear mixing coefficient and the linear absorption coefficient, respectively. Equation (4) can be broken into six differential, coupled equations, which are the real parts and the imaginary parts of the original three differential equations (1).

Given that most nonlinear interactions are preformed with pulsed laser beams, one must make a conversion from intensity to absolute energy before final efficiencies are calculated. To perform such a calculation we need to know how much energy a beam has for a given intensity distribution. However, since these equations can only describe a plane wave and not a Gaussian beam, the experimental Gaussian laser beam has been broken into different intensity steps. Each step can be treated as a plane wave and the six differential equations can be applied to describe it. Therefore, in this case, the intensity distribution, or laser pulse envelope, was approximated as a collection of twenty intensity stair steps, where the field amplitude of each step-wise function is considered constant.

Solving each of the six-coupled differential equations for each of the twenty intensity steps allows for calculation of the conversion efficiency for each step. After obtaining the conversion efficiency for each step, each value must be multiplied by the corresponding weighting factor. Then the final conversion efficiency can be obtained by summing the twenty weighted efficiencies over the entire Gaussian beam in time and space. Constant temperature and optimum tuning were assumed. This process first was used to calculate the SHG conversion efficiency and then repeated for the case of THG after using the outputs of the SHG as an input for the THG.

3. Model results

The model has been used to simulate the total conversion efficiency for second and third harmonic conversion which is then compared to experimental results. To test the model's reliability, its output was compared to the experimental results and to another independent model called the SNLO model [3]. The parameters used in the thesis model are presented in Table 1. These results for second and third harmonic generation are shown in Figs. 8.1, 8.2, 8.3, and 8.4, for 867 and 900 nm laser beams, respectively. The Experimental results represented in these graphs are the same results mentioned in Chapter V. We replaced the pulse energy of the fundamental beams at 867 and 900 nm with irradiance, which were calculated using the measured values of beam diameter and pulsewidth reported in Chapter V.

Table 1 Harmonic generation model parameters.

Wavelength	900-nm	867-nm
Linewidth	3.5 pm	3.5 pm
Divergence	800 μrad	800 μrad
$\Delta k\|_{SHG}$	43.9 m^{-1}	49.8 m^{-1}
$\Delta k\|_{THG}$	84.9 m^{-1}	81.37 m^{-1}
Crystal length (SHG&THG)	20 mm	20 mm
$d_{eff}\|_{SHG}$	0.798 pm/v	0.785 pm/v
$d_{eff}\|_{THG}$	0.536 pm/v	0.468 pm/v

The thesis and SNLO model results for the SHG conversion efficiency results along with the experimental results are shown in Fig. 8.1 and 8.2 for both wavelength 867 and 900-nm laser beams as a function of the laser irradiance. Figures 8.3 and 8.4 show the calculated and experimental results of the THG as a function of the laser irradiance at 867 and 900-nm, respectively.

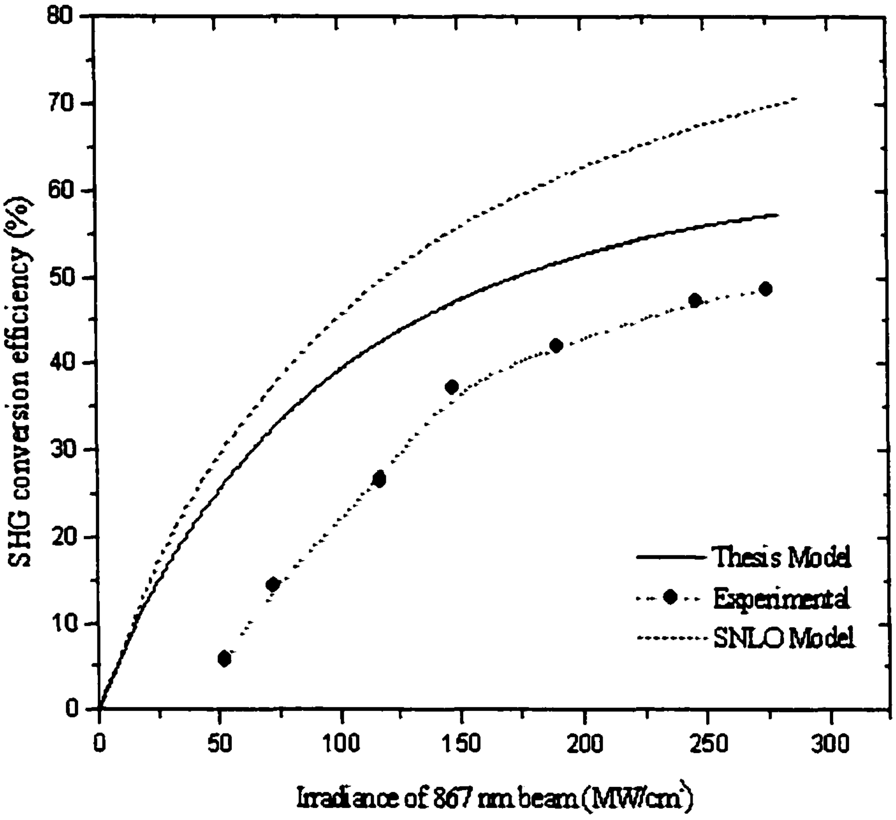

Fig. 8.1 Second harmonic generation of the 867 nm laser beam as a function of the laser irradiance.

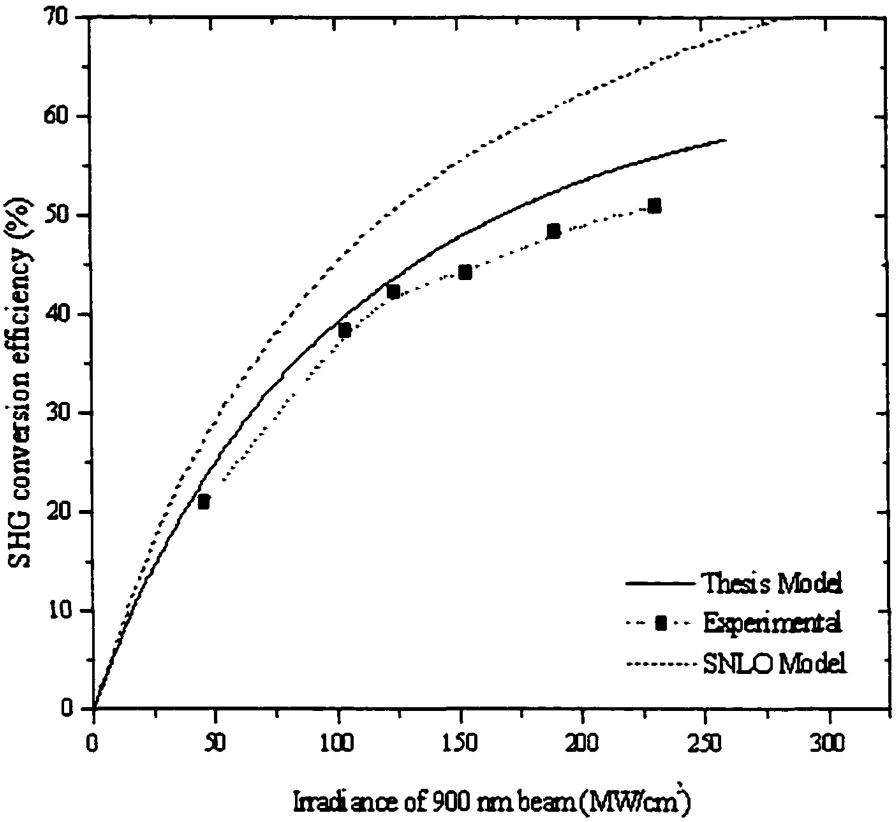

Fig. 8.2 Second harmonic generation of the 900 nm laser beam as a function of the laser irradiance.

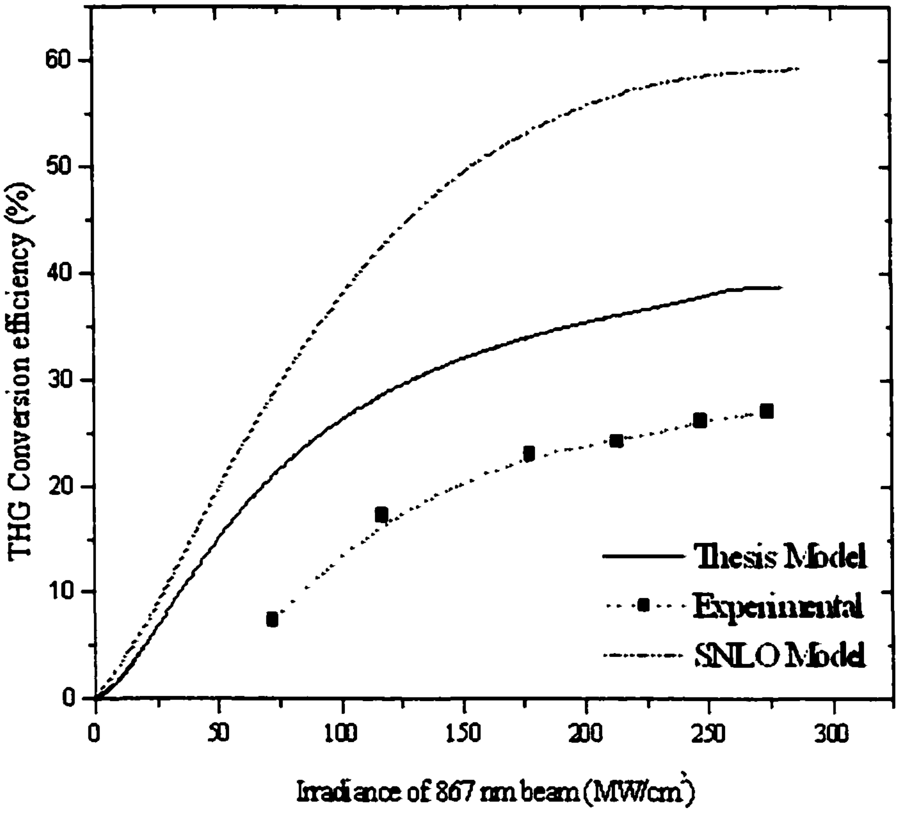

Fig. 8.3 Third harmonic generation of the 867 nm laser beam as a function of the laser irradiance.

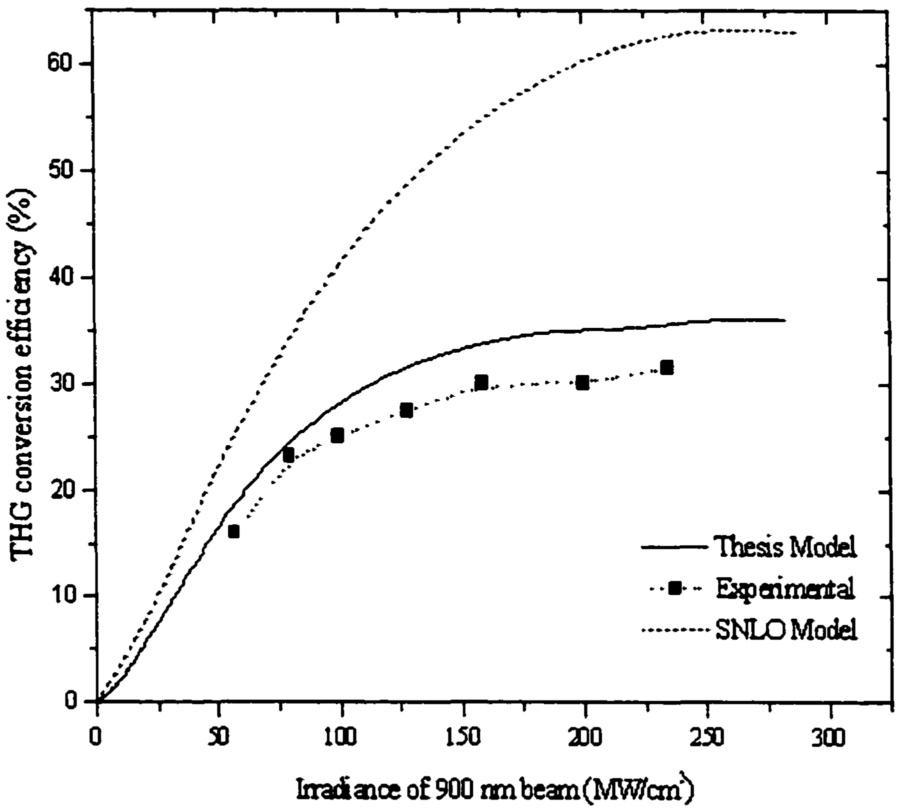

Fig. 8.4 Third harmonic generation of the 900 nm laser beam as a function of the laser irradiance.

It is shown in Figs 8.1, 8.2, 8.3, and 8.4 that the model can adequately simulate the SHG and THG processes. Our model yields results in fair agreement with the experimental results while the SNLO program results are much higher than the experimental values. This is clearly noticeable in the case of the third harmonic generation. One possible explanation for this is that the SNLO model does not account for the correct phase matching of Δk. Instead, the SNLO model assumes a perfect laser beam with Δk=0 and thus represent the SHG and THG for the ideal case.

Noteworthy, though, is that the thesis model can describe the SHG and THG conversion efficiencies of the 900 nm laser beam more adequately that the 867 nm laser beam.

To study the effect of linewidth on the harmonic generation process (especially on the process of the THG) by using our model, the conversion efficiencies of the SHG and THG have been calculated as a function of the fundamental beam linewidth and compared to the available experimental data as shown in Fig. 8.5. It was clearly observed that the conversion efficiency decreases as the linewidth of the fundamental laser beam increases. The linewidth has a very strong effect on the THG while having a less

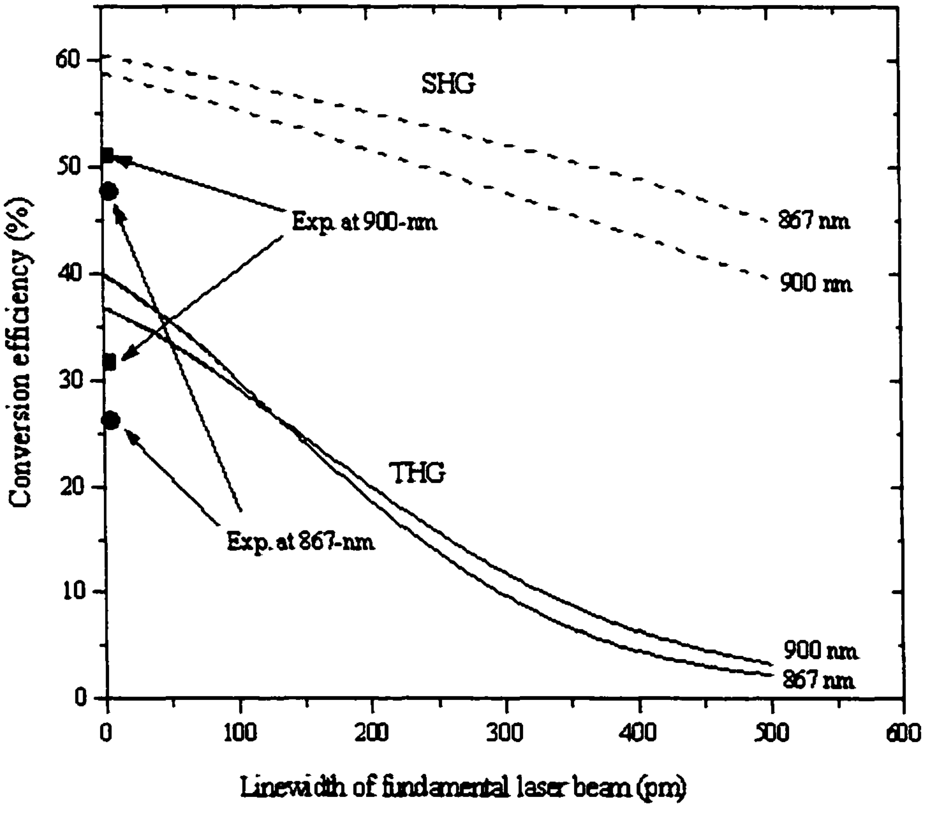

Fig. 8.5 Conversion efficiency of SHG and THG of 867 and 900 nm laser beams as a function of the fundamental laser linewidth. Shown also are the seeded Ti:sapphire SHG and THG results.

significant effect on SHG. In the worst case, when the laser is unseeded and the linewidth is 400 pm, the SHG generation efficiency reduces from approximately 60% to 48%, while the THG reduces more drastically from approximately 37% to 5 %. To achieve high conversion efficiency it is crucial that the laser be well seeded at the fundamental wavelength.

Another important factor to consider is the effect of the laser pulsewidth on the process of harmonic generation. Therefore, the SHG and THG conversion efficiencies of both 867 and 900nm have been calculated as a function of the fundamental laser pulsewidth at different crystal lengths and compared to the available experimental data as shown in Figs. 8.6 and 8.7. This data was recorded while maintaining a constant pulse energy of 120 mJ. As is shown in Figs 8.6 and 8.7, the SHG and THG conversion efficiencies of both wavelengths, 867 and 900 nm, have a peak around 20 ns at L = 20 mm (experimentally used crystal length). When the laser pulsewidth increases, irradiance decreases leading to lower conversion efficiency for both SHG and THG. For short pulse lasers, a back conversion could occur leading to a low conversion efficiency. For each crystal length, there is an optimum value for the laser pulsewidth to maximize the conversion efficiency. To achieve maximum conversion efficiency it is important to adjust the laser cavity to have a pulsewidth of around 20 ns.

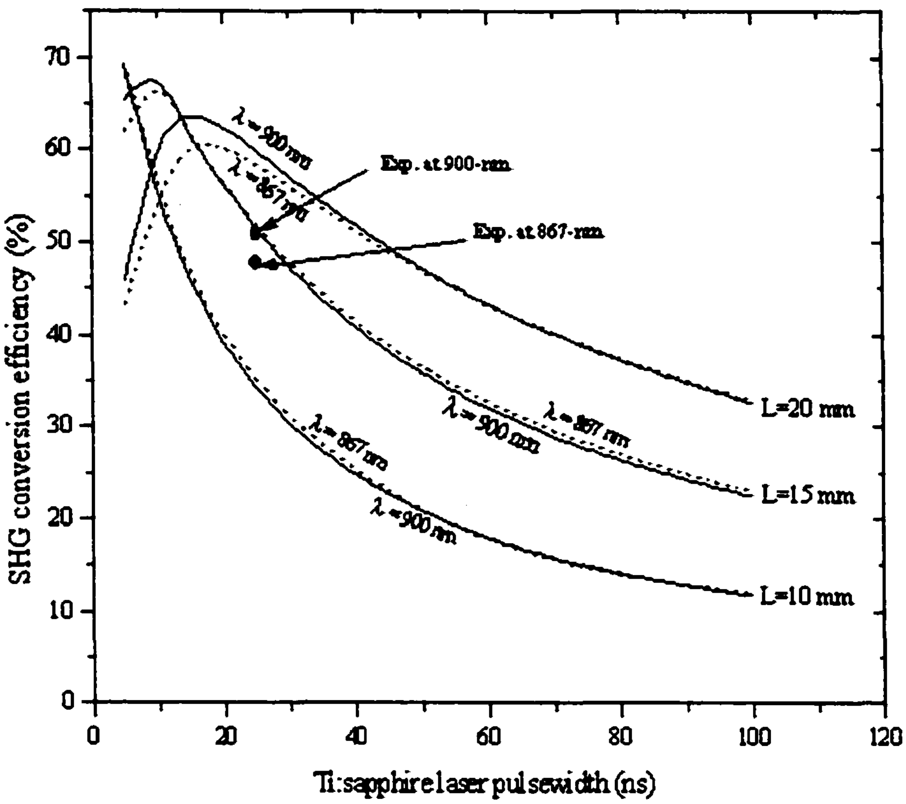

Fig. 8.6 Conversion efficiency for SHG of 867 and 900 nm laser beams as a function of the fundamental laser pulsewidth for different LBO crystal lengths. The experimental points are shown for crystal length of 20 mm.

Both SHG and THG conversion efficiencies decrease when the laser beam divergence exceeds 800 mrad. A laser beam with large divergence will lead to poor conversion efficiency due to the phase mismatch of phase fronts, which causes back conversion. This effect is so pronounced that efforts must be directed to obtain and maintain a high laser beam quality.

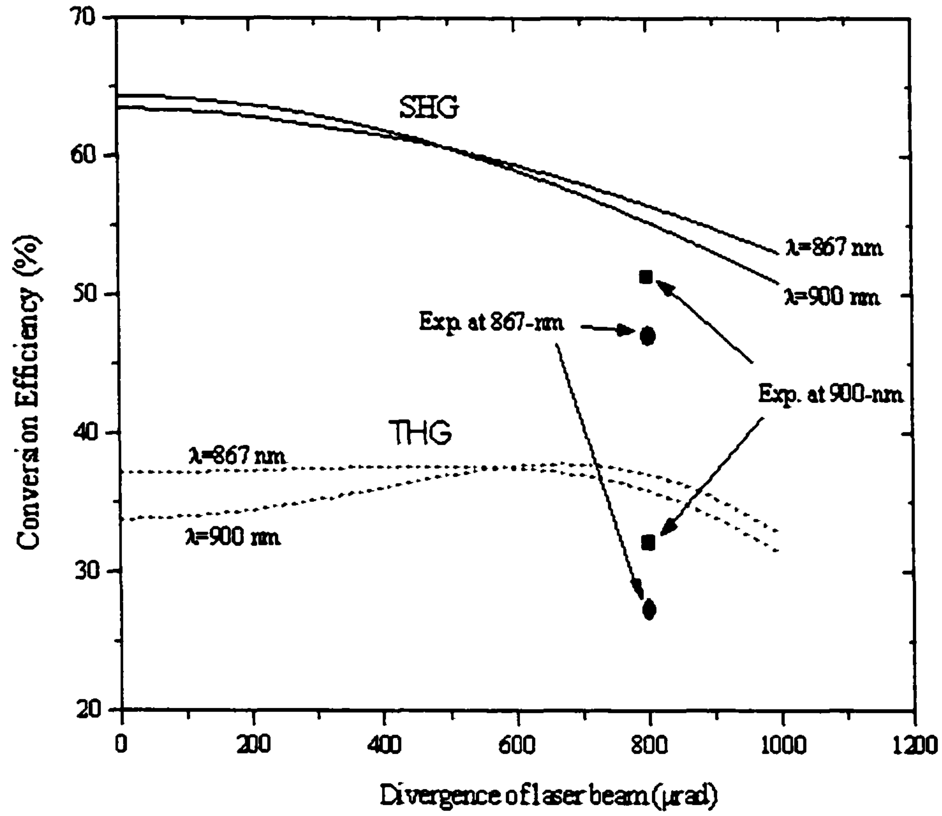

Fig. 8.8 Conversion efficiency for SHG and THG of 867 and 900 nm laser beams as a function of the fundamental laser divergence. Also shown are experimental points at 867 and 900-nm for an experimental divergence of 800 μrad.

4. Model limitations

In this model, it has been assumed that the laser beam is Gaussian; thus, the model cannot be applied to non-Gaussian laser beams. In addition, the model does not account for the walk-off angle of the doubling crystal, though the model prediction is accurate if the walk-off ratio (walk-off distance to beam diameter) is not larger than 20-30%, we concede that this is a limitation of the model for higher walk-off ratios or extremely small beam diameters, which is not the case for our beam. This thesis model is more realistic than SNLO model and is thus useful to guide the experiment in optimizing SHG and THG.

References:

1. Koechner, Walter, *Solid-State Laser Engineering*, Springer-Verlag Berlin Heidelberg New York, 1988, p. 478.
2. R. L. Byer and R. L. Herbst, "Parametric oscillation and mixing," in *Nonlinear Infrared Generation,* Y. R. Shen, ed. (Springer-Verlage, Berlin, 1977).
3. Dmitriev, V.G., Gurzadyan, G.G., Nikogosyan, D.N., *Handbook of Nonlinear Optical Crystals*, Springer-Verlag Berlin Heidelberg New York, 1991, p. 5.
4. Boyd, R.W., *Nonlinear Optics*, Academic Press, Inc.: San Diego, CA, 1992, p. 4.
5. Waverly Marsh, *personal communication.*
6. A .V. Smith and M. S. Bowers, "Phase distortion in sum and different-frequency mixing in crystals," *J. Opt. Soc. Am B* Vol. 12, No.1, pp. 49-57, (1995).
7. SNLO program, Written by Smith Arlee at Sandra Laboratories.

CHAPTER IX

CONCLUSIONS

The impetus of this research was to develop an all solid-state Ti:sapphire laser transmitter to replace the current dye lasers that could provide a potentially compact, robust, and highly reliable laser transmitter at the required on-line and off-line wavelengths for ozone differential absorption lidar aircraft measurements of atmospheric ozone.

Two compact, high-energy pulsed, and injection-seeded Ti:sapphire laser systems, operating at a pulse repetition frequency of 30 Hz and wavelengths of either 289 nm or 300 nm, were designed, constructed, and evaluated. The two laser systems consist of three main parts: the Ti:sapphire laser resonator, seeder laser, and harmonic generators. The whole system is mounted on a 42 × 63 cm^2 enclosed optical bench. A flat-flat mirror laser cavity configuration was chosen on the bases of the gain guiding effect. The gain guiding effect, induced in a solid-state medium pumped by another pump laser, can be used to produce a high quality, near-diffraction limited, high energy beam of arbitrary large diameter. The Ti:sapphire oscillator was pumped with a commercial Q-switched, frequency-doubled Nd:YAG laser operating at a repetition rate of 30 Hz. Laser injection seeding was used to provide a linewidth-narrowing mechanism for the Ti:Sapphire resulting in a < 3.5 pm linewidth. One Ti:sapphire laser cavity was set to 867nm and the other to 900 nm.

The Ti:sapphire lasers were doubled and tripled to generate UV output at wavelengths of 289 and 300 nm by means of two Lithium Triborate (LBO) nonlinear crystals because of LBO's good non-linearity, large acceptance bandwidth, and high optical damage threshold.

The Ti:sapphire lasers have shown the required output beam quality at 30 Hz, (M^2) of 1.3 times diffraction limited, at a maximum output pulse energy, of 115 mJ at 867 nm and 105 mJ at 900 nm, with a slope efficiency of 40% and 32% respectively, to achieve more than 30 mJ of ultraviolet laser output at wavelength of 289 or 300 nm.

A model that describes the physics of the laser cavity and pulse evolution was derived and presented in this thesis. This model agreed well with the experiment. A reduction of the upper laser level lifetime due to phonon absorption to a higher level was included. Another model describing the second and third harmonic conversion efficiency and the parameters affecting conversion were presented and compared with experimental results. The thesis model was useful to guide the experiment in optimizing SHG and THG.

It has been shown that the output pulse energy should increase as the input pulse energy increases, our reported output energies are limited by the concern for optical damage to the Ti:sapphire rod, the LBO crystals, and the coatings on the crystal surfaces, due to the small beam size and high energy fluence.

The focal length of the thermal lens was measured while the Ti:sapphire laser bricks were constantly cooled. This measurement can help design the Ti:sapphire laser to avoid any damage that might be caused by thermal lensing. Without cooling the focal length of thermal lens was short, within the range of cavity length, causing a frequent damage to the high reflectivity mirror of the laser cavity but with cooling the thermal focal length became longer than the laser cavity length thus avoiding optical damage.

For practical use in an airborne ozone DIAL system, future work should possibly incorporate cavity mode locking, temperature-controlled housings for the LBO crystals, and a pressure-stabilized environment for the dispersion components to improve long-term stability and reliability. Also, the brick diameter can be reduced to allow for better heat transfer from the Ti:sapphire brick to the cooled mount.

Lastly, a Ti:sapphire laser system that meets the requirements for ozone differential absorption lidar aircraft measurements of atmospheric ozone was demonstrated and ready to incorporate into the aircraft ozone system.

CURRICULUM VITA
for
KHALED ELSAYED

DEGREES:

Doctor of Philosophy (Electrical Engineering), Old Dominion University, Norfolk, Virginia,
August 2002.
Master of Science (Physics), Cairo University, Giza, Cairo,
May 1996.
Bachelor of Science (Physics), Cairo University, Giza, Cairo,
May 1991.

PROFESSIONAL CHRONOLOGY:

Department of Electrical Engineering, Old Dominion University,
Norfolk, Virginia
Graduate Research Assistant, March 1999- Present

Lasers & Electro-optics branch, NASA Langley Research Center,
Hampton, Virginia
Laser Engineer, June 1999- Present

Department of Physics, Cairo University,
Giza, Cairo
Assistant Lecturer, December 1991- March 1999.

Department of Physics, American University in Cairo
Cairo
Graduate Teaching Assistant, January1991- March 1999.

SCIENTIFIC AND PROFESSIONAL SOCIETIES MEMBERSHIP:

Member, American Physics Society, APS, 2001-present
Member, The International Society for Optical Engineering, SPIE, 2001-present
Reviewer, *Journal of Applied Optics*, OSA, 2002

HONORS AND AWARDS:

Dr. Mokhtar Award for Physics Excellence, 1991
PhD scholarship from NASA Langley Research Center, 1999
Travel grant from SPIE, 2002

COURSES TAUGHT DURING THE LAST FIVE YEARS:

General Physics Lab, Electronics Lab, Advanced Solid State Lab, Advanced Nuclear Lab, Optics Lab, Physics 111, Physics 112, Classical Mechanics, Electricity & Magnetism, Electronic Circuits, Modern Physics, and Quantum Mechanics.

SCHOLARLY ACTIVITIES COMPLETED:

- "On the study of the electron kinetic progresses in the breakdown of argon by 0.53 um and 0.248 um laser radiation," *Journal of Physics. D: Applied Physics* Vol 32, 1999, pp1633-1639.
- " 30-mJ, 30 Hz, and 300 nm Ultraviolet laser source generated by frequency tripled Ti:Sapphire laser," *CLEO 2001, CTHP6.*
- " High Pulse energy 300 nm Ti:Sapphire laser for airborne ozone lidar measurements," *Proc. SPIE Vol 4630 P 89-93, Solid State Lasers XI, Richard Scheps; Ed.,* March 2002.
- "High energy, Efficient, 30-Hz ultraviolet laser sources for airborne ozone lidar system," *Journal of Appl. Opt.,* Vol 41, No. 15, (2002).
- "A compact high-pulse-energy, ultraviolet laser sources for airborne ozone Differential Absorption Lidar (DIAL) system," in press.